Project Final Report

DEPSCoR/ONR Grant N00014–94–1–1027

Coastal Meteorology and Oceanography with Airborne 95 GHz Radar

Robert D. Kelly and Gabor Vali

Department of Atmospheric Science
University of Wyoming
P.O. Box 3038
Laramie, WY 82071–3038

January 27, 1998

Period of award: 1 August 1994 through 31 October 1997

_____

Distribution:

Dr. Scott Sandgathe, Scientific Officer   (3 copies)
Office of Naval Research, Code 322MM
800 North Quincy Street
Arlington, VA 22217–5660

Administrative Grants Officer   (1 copy)
Office of Naval Research
Resident Representative
University of New Mexico
Bandelier Hall West, Room 111
Albuquerque, NM 87131–001

Director, Naval Research Laboratory   (1 copy)
Attn: Code 2627
Washington, DC 20375

Defense Technical Information Center   (2 copies)
Building 5, Cameron Station
Alexandria, VA 22304–6145

19980210 058

Dr. Ronald Ferek   (1 copy)
Office of Naval Research, Code 322MM
800 North Quincy Street
Arlington, VA 22217–5660

DTIC QUALITY INSPECTED 3

1.0 Introduction

This document is the final project report for DEPSCoR/ONR Grant N00014–94–1–1027, "Coastal Meteorology and Oceanography with Airborne 95 GHz Radar." The grant period was originally 1 August 1994 through 31 July 1997, and was extended to 31 October 1997 by way of a 90–day no–cost extension (R&T Code 322D101–01, Modification number A00001).

In August–September1995 we flew our research aircraft and airborne radar off the coast of Oregon, focusing on the near–coastal marine stratus. In the sections to follow we summarize the research carried out during the project, list presentations and publications resulting from that work, and describe data shared with another ONR investigator. As supporting material we have also attached copies of two journal articles, two thesis abstracts, and the abstract from a conference presentation.

2.0 Presentations and publications resulting from the project

Refereed journal articles:

1998: Fine–scale structure and microphysics of coastal stratus. G. Vali, R. D. Kelly, J. French, S. Haimov, D. Leon, R. E. McIntosh, and A. Pazmany. To appear in *J. Atmos. Sci.* (Copy attached.)

1998: Retrieval of three–dimensional particle velocities from airborne Doppler radar data. D. C. Leon and G. Vali. To appear in *J. Atmos. and Oceanic Tech.* (Copy attached.)

Conference papers:

1996: Coastal stratus observations with an airborne radar. G. Vali, R. D. Kelly, S. Haimov, D. Leon, and J. French, *Preprints, 12th Intl. Conf. on Clouds and Precip.*, 19–23 Aug., Zurich, Switzerland.

Theses and dissertations:

1996: Retrieval of three dimensional winds from airborne Doppler radar data. Master's thesis, Department of Atmospheric Science, University of Wyoming, by David C. Leon.

1998: Measurement of radiative fluxes in marine stratus. Master's thesis, Department of Atmospheric Science, University of Wyoming, by Elizabeth Sinclair.

Other documents making use of data collected on this project:

Ebling, T., R. O'Malley, J. A. Barth, and R. L. Smith, 1998: SeaSoar and CTD observations During Coastal Jet Separation cruise W9508b, 17–27 August 1995. Data Report, College of Oceanic and Atmospheric Sciences, Oregon State University, in preparation.

3.0 Summary of research

3.1 Instrumentation

The primary field research equipment used on this project were the University of Wyoming King Air and the 95 GHz airborne Doppler radar. The King Air carries a full array of probes for thermodynamics, dynamics, and microphysics measurements. Full three–dimensional winds are derived from gust probe, inertial reference system (IRS), and global positioning system (GPS) data. Thermodynamic data include air temperature (including one probe designed for in–cloud measurement), dew–point, and static pressure. Cloud particle measurements are obtained with a set of four laser–optical scattering and shadowing probes (all manufactured by Particle Measuring Systems), which count and size cloud droplets (3–50 μm at 3 μm resolution), drizzle drops (25–200 μm at 12.5 μm resolution), small raindrops and crystals (50 μm–1 mm at 25 μm resolution), and precipitation–sized raindrops, aggregates, graupel, etc. (400 μm–10 mm at 200 μm resolution). Radiometers include up– and down–looking Eppley pyranometers and pyrgeometers and a down–looking Heimann IR thermometer. Data are recorded at rates ranging from 1 to 50 Hz, depending on the instrument response characteristics.

The 95 GHz Doppler radar (University of Wyoming Cloud Radar, or UWCR), which is the result of some 8 years of collaboration with the Microwave Remote Sensing Laboratory at the University of Massachusetts, can be operated with the beam looking up or to the right side of the aircraft, normal to the aircraft center-

setts, can be operated with the beam looking up or to the right side of the aircraft, normal to the aircraft center-line. In most projects the radar is operated with 100 range gates (@ 30 m), recording 10–15 profiles s^{-1}. Each profile is an average of 125–500 individual pulses. The radar is also fully polarimetric and can transmit user-designed clusters of horizontally and vertically polarized pulses. The mean Doppler velocities are usually obtained with the pulse–pair method. However, full Doppler velocity spectra can also be recorded. Precise time data are sent from the radar data system to the King Air data system, so that the data can be synchronized, post–flight, to at least 0.1 s accuracy.

3.2 Preparation for field operations.

Prior to the 1995 field operations, significant effort was dedicated to preparation of the radar. Our last prior flights had been in early 1994, wherein we experienced unsatisfactory amounts of transmitter unsteadiness, which reduced the overall signal–to–noise ratio and therefore the detectability limits for the radar. These problems were eventually solved. At the same time, we developed new techniques for ground calibration of the radar and also modified the radar for continuous monitoring and recording of receiver noise levels.

Another important area of development focused on the problem of removing Doppler "contamination" resulting from any component of aircraft motion lying along the radar beam. Removal of this contamination requires accurate, high–rate recording of aircraft attitude and 3–D motion (IRS plus GPS), and accurate synchronizing of the radar and aircraft data. We have also developed techniques for checking the accuracy of the aircraft–motion removals. This includes maneuvers which have become part of all our radar projects, placing the radar in side–looking mode and flying the aircraft in steeply–banked right turns at several different bank angles. The Doppler signal for the surface should then be zero if the two data streams are synchronized accurately and the aircraft motion removed correctly. In 1995 (Oregon) also flew the aircraft through the up-looking beam of a NOAA Doppler radar which was operating near the area of our stratus studies, giving a check of the motion correction with the airborne radar beam pointed upward.

3.3 Field operations, 1995

From 27 August to 16 September we conducted 11 flights, @ 2–4 hrs, into stratus 30–80 km off the Oregon coast, in the vicinity of 45°N latitude and 124°W longitude. Boundary layer depth in these cases was always ≤ 1 km, and the cloud layer depths varied from 100 to 400 m. Table 1 summarizes the meteorological, boundary layer, and cloud conditions for each flight.

On 25 August we conducted one additional flight in the vicinity of Cape Blanco, Oregon, mapping near–surface winds over an area near the coastline while the Oregon State University research ship (WECO-MA) was conducting a study of coastal jet separation. Copies of the aircraft data were given to the OSU group (J. A. Barth, PI) for use in their analysis.

3

TABLE 1
Summary of stratus cases
Oregon 1995 UW KingAir flights

	950827	950830	950831	950901	950902	950908	950909–1
Tme period of flight (Z)	1925–2015	1655–1805	1525–1550	1525–1650	1605–1755	1605–1820	1525–1555
Location (lat. / long.) (~50 km radius from point)	44.8N 124.2W	44.9N 124.8W	45.1N 124.4W	44.7N 124.6W	46.0N 124.6W	45.8N 124.1W	44.7N 124.2W
Subcloud $\Delta\theta/\Delta z$ (°K/100m)	?	0	?	0	+ 0.1	0.04	
Cloud base (m MSL)	50	0–100	50	200–270	400 +	400–470	
Cloud depth (m)	270	350 – 480	150	130–200	500 –	230–300	
Cloud top (m MSL)		350 – 550		400	800–900	600–700	
Cld. layer $\Delta\theta_e/\Delta z$ (°K/100m)	–0.3 to 100m +0.15 above	0	+0.45	0 high values at top	–0.4 bottom 200 m; 0 above	–0.2 lower half; +0.3 upper half	
Inversion magnitude (°C) gradient (°C/100m)	1 0.35	1 ∞	5 2.0	7 30	8 12	12 2.0	
Winds: surface (°T / m s^{-1}) cld base cld top above	 300° / 2 300° / 4 320° / decr.	 160° / 3 160° / 1 300° / 1	 90–100° / 10–15 300° / 20–25	 180° / 4 180° / 2 100° / 1	180° / 4 180° / 4 180° / 5 100° / 8	360° / 10 360° / 7 020° / 5 020° / 12 (??)	
FSSP conc. max. (cm^{-3})	160	220	800	600	450	350	
FDBAR, max. (µm)	16	22	12	15	18	16	
FLWC max.(g m^{-3})	0.3	0.9	0.35	0.5	1.0	0.7	
Rain rate, max.(mm h^{-1})	0.03	0.1	0.01	0.05	0.07	~ 0	
dBe0t max.	–5	0	–10	–2	0	–8	
Echo top	undulating, not sharp	large undul.	slight undul.			smooth	
Echo structure	weak, 0.3 to 0.5 km	strong cells; and bands	upward gra- dient; weak spots in ho- rizntal			upward gra- dient	
Echo intensity max. (dBZ$_e$)			–16 max				
	950827	950830	950831	950901	950902	950908	950909–1

Continuation of table from previous page.

	950909–2	950913		950914	950915	950916	
		part A	part B				
Time period of flight (Z)	2030–2220	2135–2335		1800–2025	1610–1820	2140 – 2325	
Location (lat. / long.) (∼50 km radius from point)	44.2N 124.6W	44.9N 124.4W		44.6N 124.3W	44.3N 124.3W	45.7N 124.3W	
Subcloud Δθ/Δz (°K/100m)	0	0.2		1.2 in lower layer	0.4	0.5	
Cloud base (m MSL)	near 100	∼ 20 – 100		300 (100 for fragments)	350 + fog to sfc	550	
Cloud depth (m)	70–200	220	280	250	380	350	
Cloud top (m MSL)	240–300	250	300	550 – 570	670 – 710	900 – 920	
Cld. layer Δθ$_e$/Δz (°K/100m)	0 (θ$_e$ variable by ± 1)	0		0 in upper layer	–0.1 to 500m; 0 above	0	
Inversion magnitude (°C) gradient (°C/100m)	7 10	5 ∼∞		10 4 (avg.)	6 20	5 5	
Winds: surface (°T / m s^{-1}) cloud base cld top above	340° / 9 350° / 9 000° / 5 020° / 5	360° / 8 360° / 8 010° / 5 decr.		160° / 3 160° / 3 330° / 8 360° /decr.	210° / 3 300° / 1 300° / 2 090° / 5	200° / 6 190° / 5 210° / 5 000° / 1	
FSSP conc. max. (cm^{-3})	600	800	600	200	300	200	
FDBAR, max. (μm)	10	10	15	20	22	20	
FLWC max.(g m^{-3})	0.4	0.4	0.6	0.6	0.6	0.6	
Rain rate, max.(mm h^{-1})	∼ 0			0.08	0.2	0.1	
dBe0t max.				+ 10			
Echo top				small undul.		flat	
Echo structure				cellular, strg. sheared at 300 m		cellular, vir-ga into layer below 400 m	
Echo intensity max. (dBZ$_e$)				10	10	5	
	950909–2	950913		950914	950915	950916	

4.0 Analysis

4.1 New technique for wind retrievals

The horizontal uniformity of the stratus provided an excellent "test bed" for developing methods to retrieve vertical profiles of horizontal wind vectors from the airborne radar Doppler data. A long–standing application of ground–based Doppler data is the Velocity Azimuth Display (VAD) wind retrieval method (Browning and Wexler, 1968: *J. Appl. Meteor., 7, 105–113*). VAD analysis requires constant–elevation radar scans, so that the Doppler data from individual range gates will be spaced evenly and can be used to obtain the first few terms of a Fourier series, yielding vertical profiles of horizontal wind direction and speed, divergence, and stretching and shearing deformations.

Data gathered with the UWCR during turns are similar to those used in VAD analysis, but, since the beam elevation angle and the 3–D platform location change continuously, the data are not spaced at even intervals and are therefore not suitable for Fourier processing. A new, more flexible method, which we have termed Airborne VAD (AVAD), was developed to handle the airborne data, starting from techniques explored by Testud et al. (1980: *J. Atmos. Sci., 37,* 78–98). The gated radar data are interpolated into ground–relative coordinates, with tiers or layers of data at constant geometric heights. A "forward model" is then specified for the winds, including divergence, deformation, etc. Singular value decomposition (SVD) is then used to obtain the vertical profiles of horizontal winds.

The AVAD technique has been tested extensively with data from the Oregon stratus, yielding wind profiles which agree well with data obtained during aircraft soundings in the same locations. Several advantages of the AVAD technique have also been identified, including 1) the aircraft turns do not have to cover a full 360 degrees (90–180 degrees will usually suffice), and 2) the beam elevation angles do not have to be held constant (20–60 degrees gives best results). As a result, AVAD can be applied to much smaller cloud areas than ground–based VAD. In addition, because the radar is flown close to or even into the clouds, the wind profiles are retrieved from very small areas above or below the flight path. Thus, the sequence of turns that are always part of a flight pattern yield multiple wind profiles in a relatively short time and area.

4.2 New insights into structure of coastal stratus

To date, our most detailed analyses of coastal stratus data focused on three consecutive days near the end of the field period (14, 15, and 16 Sept. 1995). A copy of the J. Atmos. Sci. article describing this study is attached.

The stratus layer was unbroken throughout the three–day period, but interesting changes were observed in the BL depth, cloud depth, BL wind profiles, and the vertical and horizontal patterns of radar reflectivity and Doppler velocity. Throughout the three flights, the radar reflectivity was dominated by drizzle drops (diameters > 50 μm) over the lower 2/3 to 4/5 of the cloud layer, and by cloud droplets (3–50 μm) above that. Vertical profiles of average cloud liquid water content were typical of those measured in other marine stratus, extending linearly from zero at cloud base to the maximum value at cloud top. Average droplet concentrations, on the other hand, were nearly constant through the cloud depth.

Vertical cross–sections of radar reflectivity had a "cellular" appearance, with the cells having irregular horizontal cross–sections but occurring with a dominant horizontal spacing of about 1.2–1.5 times the cloud layer depth. In all cases, cells with above–average drizzle drop concentrations (at the aircraft flight level) can be identified, and they occur with a wide range of sizes. In these same vertical cross–sections, the Doppler velocities, which are reflectivity–weighted averages and therefore dominated by the velocities of the larger drops, were downward in all but a very small fraction of the cloud volumes, indicating that drizzle drops were present in the lower cloud layers, as expected, but also present right up to cloud top.

The cross–correlation between the reflectivity and Doppler velocity data from the vertical cross–sections yielded an interesting pattern. In the lower cloud layers the reflectivity and downward Doppler velocity were positively correlated, consistent with having the strongest downward Doppler signals correspond to the presence of the largest drizzle drops. Above the mid–level of the stratus, however, the correlation changed sign, so that the strongest downward motions corresponded to the weakest echo intensities and the weakest downward motions corresponded to the strongest echo intensities (at a given level). Thus, it appears that

the strongest downward motions in the upper layers of the clouds occurred in small regions where large drops were not present and where the drop sizes had been reduced by entrainment of drier air from above cloud top. Drizzle drops, on the other hand, were still being carried to near cloud top by the strongest updrafts, with the large–drop fall speeds equal to or nearly equal to the updraft speeds. Graphical evidence for the entrainment can be found in radar cross–sections where the lowest–reflectivity areas have been highlighted. Here, some of the narrow, downward moving "plumes" of weak reflectivity extended downward more than 200 m from cloud top, ending less than 100 m above cloud base.

The 'Conclusions' from the J. Atmos. Sci. manuscript are quoted below to indicate where these studies led.

"Observations were made in stratus over the upwelling zone off the Oregon coast with an aircraft equipped with in situ sensors and a 95 GHz radar. Measurements for three consecutive days were presented in this paper. Thermal stratification and wind conditions changed significantly during that period thus allowing differences and similarities to be exploited in search of underlying causes. The clouds were unbroken, with no detectable horizontal structure in parameters other than drizzle."

"The observations here reported provide essentially a 'frozen' description of cloud structure, in images and in statistical parameters. In situ measurements, taken along lines through the clouds, were extended by the radar data to horizontal and vertical planes. Conversely, the reflectivity and velocity fields detected by the radar were interpreted in light of the air motion and dropsize distribution data from the in situ probes. In other words, the radar data provided a greater wealth of information than the in situ measurements along a line, and the ambiguities of reflectivity measurements were significantly reduced with the help of the simultaneous in situ measurements. Such combined data overcomes many of the problems and limitations identified, for example, by Davis et al. (1996) in the use of LWC data for examining scales of variation in stratocumulus."

"The observations we report are consistent, in a general sense, with the model, also suggested by other authors, of broad regions of net upward fluxes and narrow entrainment regions of stronger downward motions. Our data refine this model in three respects. First, we show that the upward flux is most significant for drizzle drops over the size range 50 to 300 μm diameter, not for LWC made up by smaller cloud droplets. This difference has important implications regarding the way the upward transport is envisaged to come about, and certainly lessens the applicability of parallels between stratus and cumulus. Second, it is clear from the radar images that the regions of upward transport are of irregular shapes over a large range of sizes. Third, we show that downward moving diluted regions existed in the clouds we examined, in spite of the absence of thermodynamic instability at cloud top. Especially in one case, and to lesser degrees in the other two, turbulence generated by wind shear might have been responsible for the initiation of entrainment. "

"Structures revealed by the kinds of radar echoes shown in this paper appear to provide a good basis for examining the degree and the scales of variability of drizzle in stratus and stratocumulus. The reflectivity images are nearly equivalent to images of precipitation concentration. It is clear that, through the many ways that drizzle interacts with other cloud properties, local variations in drizzle have significant impacts on a broad range of cloud characteristics and are of importance for the time evolution of the cloud. On the other hand, since drizzle represents a small fraction of the total water content of the cloud, effects of the drizzle structure are not felt in the instantaneous values of properties like liquid water path (LWP) or albedo."

"While we find the results here presented solidly supported by our data, undoubtedly, these observations need to be confirmed, and their range of validity

7

delineated, by cases from a broader range of conditions. The conclusions drawn
need elaboration and integration in model simulations both with respect to dynamical
and microphysical factors. At the same time, these observations might be helpful in
providing ideas and realistic constraints to model calculations."

4.3 Preliminary study of radiative fluxes

Due to instrument problems with the long–wavelength radiometers, only short–wave radiative fluxes
were available from the 1995 data. A compilation of up–looking pyranometer (downward fluxes) data for sev-
eral cases, with maximum liquid water contents ranging from 0.5–1 g m^{-3}, have yielded promising results.
After correction of the above–cloud fluxes for aircraft attitude and solar position, average flux profiles and inte-
grated liquid–water paths (LWP) were plotted for soundings through the stratus layers. Using Lambert's law,
the full–cloud volume extinction coefficient could be determined for each case. When these values are plotted
against the slant–path LWPs, along with data from another project in 1997, it appears the the volume extinc-
tion coefficient for these clouds is a simple linear function of the total cloud LWP. This relationship, which needs
to be examined for a broader range of liquid water contents and cloud depths, should be a useful addition to
modeling predictions of local radiation budgets for marine stratus.

4.4 Analyses in progress

4.4.1 Patch analyses. The structure of stratus, as revealed by the 95 GHz radar data we collected
during the 1995 field project, contain interesting clues about the development of drizzle in these clouds. The
analyses described in Section 4.2 are now being extended by further looks at the 'patches' of radar echoes
in horizontal sections across the clouds. An abstract has been submitted to the 1998 AMS Conference on
Cloud Physics indicating the direction of this work. The Abstract is quoted below:

ABSTRACT

"Airborne radar (95 GHz) observations in marine stratus revealed that drizzle
areas are patchy in the horizontal, in spite of fairly uniform LWC. Observations refer to
regions of about 10 km in horizontal extent in unbroken clouds. Reflectivity
fluctuations at given altitudes are due, principally, to variations in the concentrations
of drizzle drops (> 50 μm diameter)."

"Horizontal cross–sections of reflectivity were examined for the distribution of
regions exceeding threshold levels near the maximum values observed. For any
given threshold value, the size distribution of patches follows a negative exponential
trend. This function is invariant with thresholds when numbers are expressed as
cumulative percents and with the patch sizes normalized to some measure of the
average size. The exponent in this function varies (within the range −0.3 to −0.7) for
different cloud cases or with altitude within given cases. The actual numbers of
patches exceeding the resolvable minimum size of 60x60 m increase as threshold
values are lowered, until the patches begin to merge and start decreasing in number.
The 90th percentile patch size increases as the threshold value decreases in a nearly
linear fashion. The fractal dimension of the patch perimeters is about 1.5"

"These analyses suggest that the patchiness of drizzle areas inside stratus
layers has many similarities to spatial characteristics previously reported for the
distributions of stratocumulus top heights and for regions exceeding brightness
thresholds in cumulus and stratocumulus fields."

4.4.2 Polarimetry studies in nimbostratus

On 6 Sept. 1995 we used the aircraft and radar to investigate a nimbostratus which had developed
over the study area. The cloud contained a broad range of temperatures, including the melting band, with

8

a correspondingly wide variety of hydrometeor types and shapes. The radar data have been extensively stratified by temperature (at each gate) and beam orientation, with interesting results. In general, the ZDR values show variation with crystal type and degree of aggregation. There is a general negative correlation between equivalent reflectivity and ZDR. This correlation agrees with the in–situ 2–D probe images, in that the regions of strong positive ZDR are those with basic crystal types and little or no aggregation. When the radar beam was pointed horizontally, ZDR > 3 dB were recorded in regions with plate crystals. In regions with needle crystals, we found ZDR < 3 dB. LDR values were generally below the noise level of the radar, except in the bright band, where values of –19 to –10 dB were recorded. Reflectivities measured by the airborne radar agreed to with 5 dBZ with those measured by the NOAA Ka–band radar.

4.5 Questions deserving further investigation

In the course of this project, several questions have been raised which warrant further investigation. In the three–day sequence of stratus described in section 4.2, we repeatedly found moist (high humidity) layers directly above cloud top, rather than the sharp dry–down typically found with temperature inversions at the BL top. This feature was measured with two very different instruments (chilled mirror hygrometer and IR absorption spectrometer) and was observed during descents into and ascents out of cloud top, so instrument lag can be eliminated as an explanation. We have not yet found evidence in our 1995 data for the origins of the moist layer. And we have also not yet had the time to explore its possible influence on the stratus dynamics and thermodynamics.

Since the data collected in 1995 were near shore, interesting questions are also raised about possible mesoscale influences on the stratus origins, maintenance, structure, and dissipation. Near–shore upwelling of colder water would depend on coastline geometry and currents, and would contribute to near–shore gradients of sea–surface temperature. Such gradients would undoubtedly influence BL dynamics and sea–breeze formation, both of which would influence the stratus.

Given the cellular patterns of radar reflectivity seen by the radar, traceable to variations in the cloud and drizzle drop populations, another interesting study would focus on similar scale patterns of long– and short–wave radiative fluxes in these clouds. Short–wave absorption near cloud top, long–wave absorption and emission at cloud base, and long–wave emission at cloud top are already known to be important in stratus dynamics. Examining variations in these fluxes at the same scales of variation seen by the radar could shed new light on the origins and maintenance of the cellular structures of the clouds.

Finally, we would like to further investigate the origins and dynamics of the cloud–top entrainment as seen in the 1995 cases. Several of the questions outlined here would be relevant in such a study, including the presence of the moist layer above cloud top and the possible roles of cell–scale variations in long– and short–wave radiative fluxes in starting and maintaining the entrainment events.

Fine–scale structure and microphysics of coastal stratus.

Gabor Vali[‡], Robert D. Kelly[‡], Jeffrey French[‡], Samuel Haimov[‡], David Leon[‡],
Robert E. McIntosh[§] and Andrew Pazmany[§]

[‡] Department of Atmospheric Science, University of Wyoming, Laramie, WY 82070.
[§] Microwave Remote Sensing Laboratory, University of Massachusetts, Amherst, MA 01003.

Corresponding author address:
    Gabor Vali, Box 3038, Laramie, WY 82071, USA
    E–mail: vali@uwyo.edu

1

ABSTRACT

Observations were made of unbroken marine stratus off the coast of Oregon using the combined capabilities of in situ probes and a 95 GHz radar mounted on an aircraft. Reflectivity and Doppler velocity measurements were obtained in vertical and horizontal planes that extend from the flight lines. Data from three consecutive days were used to examine echo structure and microphysics characteristics. The clouds appeared horizontally homogeneous and light drizzle reached the surface in all three cases.

Radar reflectivity is dominated by drizzle drops over the lower 2/3 to 4/5 of the clouds and by cloud droplets above that. Cells with above–average drizzle concentrations exist in all cases and exhibit a large range of sizes. The cells have irregular horizontal cross–sections but occur with a dominant spacing that is roughly 1.2–1.5 times the depth of the cloud layer. Doppler velocities in the vertical are downward in all but a very small fraction of the cloud volumes. The cross–correlation between reflectivity and vertical Doppler velocity changes sign at or below the midpoint of the cloud indicating that in the upper parts of the clouds above–average reflectivities are associated with smaller downward velocities. This correlation and related observations are interpreted as the combined results of upward transport of drizzle drops and of downward motion of regions diluted by entrainment. The in situ measurements support these conclusions.

1. Introduction.

Understanding the evolution of drizzle in stratus is hindered by a number of difficulties in spite of the apparent simplicity of these clouds. The characteristic vertical profiles and near–adiabatic values of the liquid water content tend to indicate that vertical transport is taking place. However, it is also clear that this is not accomplished with major organized updrafts so that Lagrangian models of condensation and coalescence are inapplicable. The question is to what extent and on what scales vertical motions and drizzle development are random versus organized.

Model calculations have been devised which superimpose some form of turbulent transport on the coalescence process (Nicholls, 1987; Baker, 1993; Austin et al., 1995; Feingold et al., 1996). In these models, the main focus is on the vertical distribution of cloud properties, and they are anchored to observations in terms of the variance of vertical air velocities measured by aircraft. On the other end of the scale, Paluch and Lenschow (1991) showed evidence for variations over horizontal scales of >10 km in cooling by evaporation of drizzle; similar patterns are also apparent in the data of Austin et al. (1995). Cellular patterns of drizzle formation with scales on the order of 1 km are incorporated, due to quite different forcing, in the model results of Kogan et al. (1995) and of Feingold et al. (1996). The role of gravity waves above the cloud layer in imposing local variations that ultimately also influence drizzle development has been mentioned by a number of authors. Internal circulations are also assumed to play a role in the eventual breakup of stratus to stratocumulus (e. g. Schubert et al., 1979; Krueger et al., 1995).

A large number of investigations have shown the existence of structure (inhomogeneities) in the internal composition, thermodynamic and turbulence characteristics, and radiative properties of stratus and stratocumulus (among others: Sauvageot, 1976; Paluch and Lenschow 1991; Welch et al., 1988a and 1988b; Lee et al., 1994; Boers et al., 1988; Cahalan and Snider, 1989; Duroure and Guillemet, 1990; Kikuchi et al., 1991; Kikuchi et al., 1993; Gollmer et al., 1995; Davis et al., 1996; Gerber, 1996). However, the connections between these patterns and the development and spatial distribution of drizzle were largely inaccessible. This contrasts with the extensive studies available on the structure of precipitation from a variety of other precipitation types (Fabry, 1996; and references therein).

One of the difficulties in studying the connection between structure in other characteristics and drizzle development is that cloud composition, specifically the size distribution of cloud droplets and drizzle drops, is poorly documented by the in situ probes carried on aircraft. Total cloud droplet concentration and liquid water content are the only parameters for which adequate sample sizes can be obtained; the resolution achievable in measurements of the concentrations of larger droplets and of drizzle drops is very limited. A common limitation for all in situ measurements is that they are restricted to a line along the flight path. Liquid water path (LWP) measurements via microwave radiometry provide another type of description (e.g. Cahalan and Snider, 1989), but because of the inherent vertical integration through the entire depth of the clouds these data are also difficult to interpret from the point of view of cloud spectra evolution. The purpose of this paper is to show observations obtained with an airborne radar operating at 95 GHz (3 mm wavelength) in marine stratus, and to explore the additional insights these data can provide on cloud processes. While still an integrative quantity whose precise interpretation depends on knowledge of the size distribution of drops, radar reflectivity is unique in depicting the spatial distribution of the relative intensity of precipitation formation. The information obtained from the radar–observed velocity fields is also unique in depicting essentially instantaneous fields of hydrometeor velocities over regions of several kilometers in horizontal extent. A further strength of the airborne radar data used in these studies is that the reflectivity and Doppler velocity data are referenced along the flight path to information derived from the in situ probes carried by the aircraft.

The observations to be described were made off the Oregon coast in September 1995. Flight locations were generally 30 to 80 km off the coast, in the vicinity of 45°N latitude and 124°W longitude. A total of 11 flights were made over a period of 3 weeks. The boundary layer was less than 1 km deep in all cases and cloud depths varied from 100 to 400 m. Flight patterns consisted of mixtures of level segments below and within the cloud, and of vertical soundings along straight or spiral paths. The duration of each flight was 2 to 4 hours, and the cloud area explored was about 50 km in horizontal extent. Data from three consecutive days will be presented. One of these days had quite unusual dynamic and thermodynamic structures while the other two days were more typical of marine stratus and stratocumulus situations. The contrasts and similarities that were found in the data for these different situations are helpful in isolating physical links and in establishing the generality of some of the findings.

The main focus of the paper is on the development of drizzle. However, this interest is not interpreted narrowly; cloud characteristics are presented in some detail so that these observations, and the potential applicability of the unique radar observations to those from other areas can be assessed.

2. Instrumentation.

a. In situ probes

The University of Wyoming King Air aircraft is equipped for the measurement of position, attitude, relative air motion, hydrometeor distributions and radiation. Specifications of the instrumentation relevant to this study are listed in Vali et al. (1995). To clarify the interpretation of the data presented here, some comments on the measurement of key parameters are in order.

As will be seen in the soundings, humidity measurements just above the cloud layer appear somewhat anomalous, showing constant values or increases rather than decreases. Humidity measurements are available from two instruments, a chilled–mirror device and an infrared absorption device. While not in perfect agreement, both devices show the same trends above the clouds. The observed profiles are independent of whether the data were recorded during ascents or descents. Thus, since the two instruments are located at different positions on the aircraft and operate on different principles, and since pre–wetting in the clouds does not seem to influence the results, we have no reason at this time to question the humidity measurements.

Vertical wind is determined with data from an inertial navigation system and from a gust probe, which are recorded at 50 Hz after anti–alias filtering with a cutoff frequency of 10 Hz. Instantaneous vertical wind values have a precision of the order of cm s^{-1}. Average vertical winds for wavelengths of 100 m to 5 km are limited in accuracy by the determination of aircraft motion from the inertial reference system and the gust probe; the resultant error is estimated to be < 1 m s^{-1}. In any event, mean vertical velocities over kilometer distances are forced to zero.

Cloud droplets are measured with the forward scattering spectrometer probe (FSSP, from Particle Measuring Systems, Inc.) in fifteen size categories. Most data for this paper were recorded with bin sizes of 3 μm at 10 Hz. Calibration of the FSSP is based on sizing of polystyrene spheres; the sample volume is determined from the laser beam diameter and from a micrometer tracing of the depth of field. Data processing follows Brenguier and Almodei (1989) and Brenguier (1989). The 'reset' rate was not recorded for this project, so it was set to five times the 'strobe' rate; later data on the reset parameter proved that assumption to be valid. While no reference standards are available, we estimate the accuracy of total droplet concentrations to be around 10%, with sizing accuracy around 15%. These errors lead to roughly a factor 1.7 maximum possible uncertainty in the liquid

water content (LWC) derived by integration of the droplet spectra. Actual errors are probably smaller; comparisons with LWC values measured with the CSIRO hot–wire probe generally show agreement within about 20%. Paluch et al. (1996) estimate the inherent errors in LWC derived from the FSSP data to be $\pm 13\%$.

Drizzle drops are measured with an optical array probe (2D–C, from Particle Measuring Systems, Inc.). Measurement granularity is 25 μm; data for this study were grouped into intervals of 50–100, 100–150, 150–200, 200–250 and 250–350 μm. No drops beyond 350 μm diameter were observed in this study. Artifacts due to water streaming from the probe tips were rare, but were nonetheless removed in processing. Drop sizes were taken to be given by their maximum dimensions along the flight direction; this treatment leads to a possible underestimation of drop size by about 25 μm due to the electronic delay in triggering the detector circuits. No corrections were made for the size dependence of the depth of field. This is based on agreement found between the size distributions of ice crystals measured by direct collection and by the 2D–C probe. Baumgardner and Korolev (1997) show that for water drops, and with the response time of the detectors taken into account, the depth of field for drops <100 μm is underestimated; for our first size category their correction would be approximately a factor of 10. The aforementioned shortcomings in data processing may be responsible for the local minima in our size spectra near 50 μm diameter, but we do not consider the evidence for this conclusive.

b. Radar.

The advantages and disadvantages of 95 GHz (3 mm wavelength) radars for meteorological studies have been widely discussed. Lhermitte (1988a and b) reported the first meteorological applications of this frequency. Pazmany et al. (1994a), Vali et al. (1995) and Galloway et al. (1997) describe the results of work done by the same University of Massachusetts and University of Wyoming groups with earlier versions of the radar system utilized in this study . Clothiaux et al. (1995) presented a summary of results obtained by the PennState University group in various cloud types. Sassen and Liao (1996) presented calculations of reflectivity and cloud content for 95 GHz. Considerable interest in 95 GHz radars derives from plans to build a spaceborne radar of this wavelength (Browning et al., 1993; IGPO, 1994).

From our point of view, the choice of the 95 GHz frequency was dictated by the small overall size and by the narrow beam angle achievable with a small antenna, enabling such a radar to be fitted at reasonable cost to the University of Wyoming twin–engine King Air aircraft. The radar used in this study has been described in Mead et al. (1994) and in Pazmany et al. (1994b). Main parameters of the radar, as used in these experiments, are: 1.6 kW peak power, 30 m range resolution, 10–20 kHz pulse repetition frequency, real–time integration of up to 500 pulses, 7.5 to 15 km and 8 to 16 m s^{-1} unambiguous distance and velocity ranges, 60 m minimum range.

The antenna is pointed to the right side of the fuselage. A reflector plate housed in an airfoil faring outside the fuselage can be moved into position to direct the beam vertically upward. The half–power beam angle is 0.7°. The antenna and reflector combination were designed to point either vertically up when the aircraft is in level flight at average load and airspeed, or perpendicular to the longitudinal axis, to the right of the aircraft. For reflectivity data we do not correct the locations of range bins for small deviations (< 5°) in pitch or in yaw. The measured Doppler velocities are converted to ground–relative values by removal of components of the aircraft motion in the beam direction. The manner in which this was accomplished is described in Leon and Vali (1997). In addition, during the Oregon program the aircraft was flown over the NOAA Ka–band radar (Kropfli et al., 1995) and the vertical Doppler velocities compared; based on that, a –0.3 m s^{-1} correction was applied to the airborne vertical Doppler velocity data presented in this paper.

The received power measurement was calibrated on the ground using a corner reflector. The accuracy of the calibration is ± 2 dB. During operation, the power output of the radar was monitored and found to have been repeatable within 3.6 dB over the three days discussed in this paper. The receiver noise level was constant to better than 1 dB during this same period. Over periods of several minutes, the data collection interval for images to be presented here, both the transmitter and the receiver were steady to better than 5% coefficient of variation. Thus, the precision of reflectivity values within individual data segments (images) is quite high, but absolute values have, conservatively, possible errors of up to 5 dB.

Reflectivities have been thresholded to exceed the fluctuation in noise level by at least two standard deviations. Noise levels were determined from power received just prior to transmission of pulses. Received reflectivity values below the threshold were set to large negative numbers and appear in the images as black areas; also, no velocity data are accepted for such points. The contribution of turbulence to the observed reflectivities is estimated to be negligible. Using the observations reported by White et al. (1996), the calculated reflectivity factors for turbulence are near -80 dBZ. Attenuation at 95 GHz is appreciable for clouds of the type encountered in this work. From data collected with a horizontal beam, in cloud areas indicated by the in situ probes to be relatively uniform, we determined that the attenuation coefficient (in dB km^{-1}) is well represented by the relation $\{0.7 + 4.4 \cdot (LWC)\}$, where LWC is in (g m^{-3}) . This result agrees well with the calculated values of Liebe et al. (1989) and Lhermitte (1990). Attenuation corrections were made for horizontal echo sections based on the above formula and on the mean LWC measured during the period. Attenuation corrections were not made for vertical cross–sections, since the combination of limited cloud depth and small LWC values lead to maximum attenuations of <1 dB, as also shown by the calculations of Clothiaux et al. (1995).

3. General cloud characteristics.

All three days to be discussed had solid cloud covers without visible breaks in the clouds. Therefore, the cases are classified as stratus, not stratocumulus. Satellite images for the three study periods are shown in Fig. 1. As the small squares indicate, the flight locations were 30–80 km off the coast, in clouds of uniform appearance, and at distances from cloud boundaries that provided a minimum of 12 h of advection time to the region of observation. The images also show that the flight areas were to the NE of large regions of stratocumulus. The flights took place near local noon. No clouds were present above the stratus, so the clouds were exposed to full solar heating and infrared cooling.

The depth of the boundary layer gradually thickened during the 3–day sequence to be described in detail (950914 through 950916), and there were significant changes over that period in winds and in sea–surface temperatures. On the day preceding the sequence (950913) the base of the inversion was at 300 m ASL (above sea level[1]) and the stratus layer was about 150 m in depth. On the first study day the inversion base was at 550 m. By the last day (950916) the inversion base was at 920 m and cloud depth increased to 300 m. For comparison, the cloud at the beginning of the first Lagrangian experiment (L1) described by Bretherton and Pincus (1995) was at similar altitude, and was about as deep as the cloud observed on the second day of our sequence. In this paper, the evolution of the cloud layer is not analyzed in terms of large–scale meteorological factors. Cloud observations for each day are treated essentially as independent data sets. This is justified by the brevity of observations on each day in comparison with the time interval between them. Nonetheless, by focussing on three consecutive days in this paper, an example is provided of the longer term evolution of the boundary layer and of the associated stratus.

---

1. All heights in this paper are referenced to sea level. Altitude data were taken from a precision radar altimeter.

6

Soundings for the three study days are shown in Fig. 2. Panels (from left to right) show data for temperature (T), total mixing ratio (q_t), equivalent potential temperature (θ_E), potential temperature (θ), horizontal wind direction (*wdir*) and horizontal wind magnitude (*wmag*). Data in these plots are averages in 25-m altitude blocks over all observations from arrival at the study site to departure from it roughly 2 hours later. The depths of the cloud layers are indicated by heavy vertical lines in the first panel of each sounding. Temperature profiles are not far from T=15°C–0.005H, with H in meters, between 330 m and cloud top for 950914, and for the entire layer below the inversion for the other two days. This is near the wet adiabatic lapse rate for 10°C and 950 mb. Temperature changes at the inversion remained roughly the same, +5°C, for the period. Fluctuations in temperature at any given altitude were quite small (typically <0.2°C standard deviation) over the typical 2 hour duration and about 50 km spatial extension of each flight. Below the inversion the standard deviations of the temperature measurements were ≈0.2 °C. Greater variability was found near the inversion layer. Humidity measurements show unusual constancy just above the cloud layers instead of the more usual sharp decrease; as discussed in Section 2, we have no reason to doubt the validity of these data. (A humidity sounding similar to those we observed was also reported by Rogers and Telford (1986) in their sounding S2, that was, coincidentally, taken closest to the coast.) In all cases, within the accuracy of the measurements, saturated conditions prevailed to the lowest flight altitudes (~50 m). The principal stratification of the boundary layer, based on detailed temperature profiles, is given in Table 1.

As shown in Fig. 2 and in Table 1, the sounding for 950914 has several unusual features which deserve closer examination. Temperature and humidity soundings are shown in greater detail in Fig. 3; points in this diagram represent 1-second averages of data recorded during several ascents and descents through the cloud layer. The humidity measurements here show increases above the cloud layer; in Fig. 2 these are less evident due to the larger scale of the diagram and because of the averaging by altitude intervals. The main cloud layer, defined (somewhat arbitrarily) as the region of near-constant θ_E values, overlies a stable layer of about 330 m depth. Within that stable layer there is a complete reversal of wind direction, from southerly near the surface to almost northerly above that. The altitude of direction reversal coincides with near-zero speeds. Shear is strong (~0.03 s^{-1}) from the surface to about 380 m altitude (50 m into the cloud); there is little shear throughout the rest of the cloud layer. The main cloud layer is not well defined by the LWC; zero LWC values are found only at about 50 m ASL and below, but there is a change in the vertical gradient of the LWC at the base of the constant-θ_E layer (Fig. 14). Soundings obtained at different times indicate that the base of the inversion rose by about 20 m and cloud base rose by about 50 m during the 1.7 h period of the flight. The cloud layer warmed by about 1°C during that time. These gradients are not large; the rate of rise of the inversion base is only about 50% greater than the mean value over 72 h, and only about a third of the rate reported for one day by Gerber et al. (1989).

7

Table 1. Stratification by stability.

DATE	Height interval (m)	Lapse rate ($^\circ$C km^{-1})
950914	0 – 330	+3.2
	330 – 520	−5.0
950915	0–700	−5.0
950916	0–100	−7.9
	100–300	−1.0
	300–580	−8.0
	580–920	−5.0

Soundings for the other two days are closer to the usual pattern for well–mixed, inversion–capped boundary layers (Fig. 2 b,c). While some directional wind shear is still evident below the cloud on 950915, there is none on the last day. The deep near–surface stable layer is gone by these days. The inversion was about the same strength, and the magnitude of the wind shear across the inversion layer was also comparable. On these two days there were no discernible time trends in the soundings; variabilities were on smaller scales.

The dimensionless coordinate ϕ will be used at times to describe cloud depth, with $\phi=0$ at cloud base and $\phi=1$ at cloud top. We use this normalization instead of one based on total boundary layer depth, primarily because on one of the days the boundary layer had a complex structure, and because it permits better comparisons of cloud microphysics properties. Cloud base was at 0.60, 0.53 and 0.65 times the total boundary layer depth for the 3 days.

Drizzle was observed to be falling from cloud base and reaching the sea surface in all three cases. Precipitation rates at cloud base were near 0.01 mm h^{-1}. On the first day, 950914, the rate increased to 0.02 mm h^{-1} near the sea surface due to the presence of the weak cloud in the stable surface layer. On the other two days there was little change below cloud base. The mass concentration of drizzle increased from near $2\cdot10^{-3}$ near cloud top to about $8\cdot10^{-3}$ g m^{-3} at cloud base in all three cases. The uniformity of drizzle characteristics is consistent with having similar cloud depths for the last two days; the cloud on the first day was only 2/3 as deep.

4. Echo patterns.

Images. Reflectivity (Z) and velocity[2] (V)fields, observed with the radar pointing upward, are shown in Fig. 4 for typical flight segments of each of the three study days. Each of these images was recorded during a level flight segment (±5 m); the vertical scales are altitude above the sea surface. The images are shown with 1:1 horizontal and vertical scales. As mentioned before, each cloud situation was quite steady in time; this is also borne out by the close similarities observed among the 6–10 images recorded at various times during each flight of approximately 1.5 to 2 hours.

---

2.   For simplicity, the term 'velocity' will often be used to refer to the observed Doppler velocity corrected for aircraft motion. This velocity represents reflectivity–weighted particle velocities with respect to the ground. Upward velocity is positive. If the term Doppler velocity is used, for clear differentiation from air velocities, it also will mean velocities corrected for aircraft motion, not the Doppler velocities actually measured.

The main features to be noted in these images are the relative uniformity of the upper echo boundary and the cellular structure of the echoes. Most of the high–reflectivity cells extend downward from near the echo tops and become more or less sheared through the lower parts of the images. The occasional appearance of stronger echoes not originating at the top is probably related to the orientation of the sample plane relative to the environmental winds. There are no breaks in the echoes. These characteristics apply to all three examples here presented and have been found to be also valid for other stratus cases examined.

Fig. 5 shows the shapes of the high–reflectivity cells in horizontal sections. These data are also from level flight segments but with the radar beam pointing sideways from the aircraft. Data from two or three different levels are displayed for each case; the lapse of time between data segments was anywhere from a few minutes to half an hour. An attenuation correction has been applied in each image according to the average LWC observed along the flight segment. Except in the images for the two lower altitudes for 950914 in Fig. 5, the echo cells exhibit rather irregular and highly intricate shapes. Cell sizes cover quite a large range.

For 950914, distinct echo streaks are seen to run at a 335°–155° orientation in Fig. 5 for 90 m altitude. There is also some evidence for echo lines of 320°–140° orientation at 300 m. No preferred orientation of echoes is perceptible in the 460 m ($\phi=0.59$) image. The streaks result from the strong wind shear below 400 m; this is also seen in the vertical sections.

Source of reflectivity patterns. Interpretation of the reflectivity and velocity distributions shown in Figs. 4 and 5 must take into account the fact that the relative contributions of different drop size ranges to the reflectivities and to the reflectivity–weighted fall velocities vary with altitude. This drop–size weighting of reflectivity and velocity can be calculated with the help of the size distributions recorded by the in situ probes.

Fig. 6 shows the results of this analysis for reflectivity, using data from the ascent and descent soundings. The dominant contribution in the lower parts of the clouds comes from $(Z_{calc})_{twodc}$, the reflectivity due to drizzle drops (>50 μm diameter, from the 2D–C probe), whereas $(Z_{calc})_{fssp}$, the reflectivity due to cloud droplets (<45 μm diameter, from the FSSP probe), becomes stronger near cloud tops. The crossover from drizzle domination to cloud droplet domination occurs at 480 m ($\phi=0.68$) for 950914, at 670 m, ($\phi=0.90$) for 950915 and at 830 m ($\phi=0.74$) for 950916. From this we can generalize that the crossover occurs in the upper 2/3 of the clouds. One evident reason for the crossover to greater contributions to reflectivity by cloud droplets is the increase in LWC and in mean droplet size with height within the cloud.

However, it is important to look beyond average reflectivities in order to establish the roles of different drop sizes in producing the observed patterns of variation about the means. There is little question about the sources of the patterns in the lower portions of the clouds where the absolute values are dominated by drizzle. In these regions it is also found that the standard deviation of $(Z_{calc})_{fssp}$ over contiguous level flight segments of 5–12 km length is typically an order of magnitude smaller than the standard deviation of $(Z_{calc})_{twodc}$ so that the variation in Z is dominated by variations in drizzle drop populations. Furthermore, while essentially no correlation can be found between Z_{obs}, the observed reflectivity, and $(Z_{calc})_{fssp}$, that is due to cloud droplets, positive correlations of 0.3 to 0.6 are found between Z_{obs} and $(Z_{calc})_{twodc}$. Although this correlation is not as high as it should be, due to the separation between sample volumes and the inadequate sampling rate of the 2D–C probe, the correlation supports the conclusion that drizzle dominates the reflectivity patterns.

Near cloud top, above the crossover to domination by smaller drops, the sample rates for larger drops is so low that it becomes more difficult to extract valid data. This problem is exacerbated by the fact that no long horizontal flights legs were made in those regions. A number of points can nonetheless be made. First, the maximum relative contribution to reflectivity is from droplets of

around 30 μm diameter. Second, the standard deviation of the de–trended values of $(Z_{calc})_{fssp}$ (10–m resolution data) is only about 1 dBZ, which is considerably less than the variability of the observed reflectivities. Third, in all three clouds, about 10% of the values of $(Z_{calc})_{twodc}$ from regions above the crossover points exceed the highest values of $(Z_{calc})_{fssp}$ for the same regions. Fourth, although much less pronounced toward cloud top, the reflectivity patterns extend without noticeable changes above the crossover heights. These observations suggest that one can extend the conclusion that the major source of variation in reflectivity is the non–uniform spatial distribution of drops >50 μm, and definitely >30 μm diameter, even to regions near cloud top. As mentioned before, in the lower parts of the clouds drops >100 μm account for the reflectivity patterns.

Since the size dependence of terminal fall velocity further increases the sensitivity of V_{calc} to larger drops, the reflectivity–weighted fall velocity, V_{calc}, is dominated by drizzle drops at all heights except within the last few meters below cloud top where maximum drop sizes are <50 μm.

5. Echo statistics and Z–V correlations.

Echo intensities at any given altitude in the clouds have a relatively wide range. Statistics[3] of the observed reflectivities and vertical velocities are shown in Fig. 7 for the data segments of Fig. 4. The distribution of dBZ values at a given altitude is quite symmetrical and can be well approximated by a normal distribution (log–normal in terms of Z). The average value of the widths of the distributions is around 5 dBZ; this corresponds to a geometric standard deviation of 0.5 for the distribution of Z. It is worth noting the similarity of this value to the geometric standard deviation of 0.39 reported by Cahalan et al. (1994) for liquid water paths determined by radiometric observations.

Although not in all cases, in general, the spread in reflectivity values is greatest in the drizzle below cloud base where the 95% range covers 15 to 20 dBZ (factors of 30 to 100 in Z). In the upper reaches of the clouds this range is about 5 to 10 dBZ (factors of 3 to 10 in Z). This latter variation can be accounted for either by variations of about factors of 1.2 to 1.5 in the diameters, or by factors of 3 to 10 in the concentrations of drops.

For the majority of cloud volumes where reflectivity is dominated by drizzle, it is interesting to convert reflectivity to drizzle rate. Calculating both reflectivity and rainfall rate from the size distributions measured with the FSSP and 2D probes, we find that the relationship $Z = 10 \cdot R^{1.0}$ (with Z in $mm^6 \, m^{-3}$, and R in $mm \, h^{-1}$) represents the central tendency of the data quite well for all three days (within factors of about 2 for $R > 0.05$, and within about a factor of 10 for smaller R). Accepting the exponent of unity means that the average 10 dBZ (factor 10 in Z) range of variation of echo intensity translates into a factor 10 variation in precipitation rate, and the more extreme 20 dBZ range corresponds to a factor of 100 in precipitation rate. Clearly, these are significant deviations from horizontally averaged values.

The mean values of the observed vertical velocities are close to the calculated reflectivity–weighted fall velocities for given altitudes. This is consistent with the expected near–zero mean vertical air velocities. For the first two days (Figs. 7a and 7b), all the observed velocities are downward (negative); i.e. no net upward motion of particles is detected anywhere. On 950916 (Fig. 7c), a small fraction of positive values are found near the middle of the cloud and the fraction increases from there upward. However, even in this case one must bear in mind that the magnitudes of the observed positive values are smaller than the estimated accuracies of the vertical air velocity, and hence also of the Doppler velocity, measurements. The general trend to smaller negative (and perhaps some positive) values in the upper regions of the clouds is due to the smaller drop sizes and

---

3.   Reflectivity statistics were calculated in terms of Z, then converted back to dBZ.

fall velocities prevailing there. Interestingly, the range of variation of the measured velocities at given altitudes is relatively small, 0.5 to 0.7 m s⁻¹ for 95% of the points. This variation reflects the combined effects of air velocities and of variations in drizzle concentrations and sizes. At least in the upper parts of the clouds, as will be shown later, these two factors work in opposite directions, thus reducing the overall variability.

Even simple visual comparisons of the reflectivity and particle velocity images indicate a considerable degree of correspondence between the two fields. A quantitative expression of this correlation is shown in the right–most panels of Fig. 7. The main feature of these reflectivity–velocity correlations is a reverse–S pattern; the same pattern is evident in all of the more than twenty instances examined. At low altitudes, higher reflectivities correspond to greater downward particle velocities. This is as would be expected for clouds from which drizzle is falling: higher reflectivity regions indicate larger and faster falling drops. However, in the upper regions of the cloud this pattern reverses: zones of higher reflectivity have <u>smaller</u> downward particle velocities. The crossover from negative to positive correlations takes place near ϕ=0.54, 0.56 and 0.35 for the three examples shown. Maximum positive correlations are found at ϕ=0.82, 0.90 and 0.72 for the three cases. Both the crossover point and the position of the maximum have nearly equal values for the first two days and are lower for the third day. It should be noted that the regions of positive Z–V correlations start at considerably lower altitudes than where the changeover occurs (cf. Fig. 6) from reflectivities dominated by drizzle drops to reflectivities dominated by cloud droplets. This fact, and the absence of positive (upward) V–values, rule out the explanation that the positive Z–V correlations arise due to the association of 'updrafts' with higher liquid water contents.

The reverse–S patterns in Z–V correlations appear to be a robust characteristic of the clouds studied, so it is important to examine their origins. Different factors influencing the pattern are explored in the following paragraphs: (i) vertical air velocity versus observed reflectivities, (ii) vertical air velocity versus calculated reflectivities for drizzle and (iii) diluted downward plumes. These examinations lead to the conclusion that the dominant factor in producing the reverse–S patterns is the vertical transport of drizzle drops.

Vertical air velocity vs. observed reflectivity. One suggestion for the vertical transport of hydrometeors emerges from the relations between the observed reflectivities Z_{obs} and the aircraft–measured vertical air velocities w. Scattergrams of air velocity[4] (w) vs. reflectivity (Z_{obs}) from the side–looking cases in Fig. 5 are shown in the upper panels of Fig. 8 with each point representing 3.4 m of flight path. These samples are from the middle to upper parts of the clouds (460, 600 and 750 m, or ϕ=0.59, 0.70 and 0.50 for the three cases). Weak positive correlations are evident: r_{wZ}=0.23 to 0.42 (see Table 2). The lower panels in Fig. 8 indicate the correlation coefficients for the entire sample of each case and for subdivisions of it; the latter serve to illustrate the relative homogeneity of the data sets, i.e. that not some specific larger–scale cloud region yields the points that dominate the correlation. In contrast with the foregoing, no correlations are found lower down in the clouds, and strong negative correlations prevail in the subcloud precipitation . These data are further characterized in Table 2 with the quantity Δ (dBZ), the difference in average reflectivity for points with air velocities that differ from the mean by at least one standard deviation to either side of it. This quantity indicates that upward air motions are associated with reflectivities that exceed those associated with downward air motions by factors of up to about 2.

---

4.   The recorded air velocity values have been adjusted to a zero mean over each flight segment. The offsets were 0.15, 0.3 and 0.13 m s⁻¹ for the three cases here considered; these values are within the accuracy of the measuring system.

TABLE 2. Measured reflectivity (Z_{obs}) vs. air velocity (w).

Date	Altitude (m)	Norm. depth ϕ	Length (km)	$w-Z_{obs}$ correl. r_{wZ}	$\Delta(dBZ)$	$Z_{obs}-(Z_{calc})_{twodc}$ correl. r_{ZZ}
950914	460	0.59	6.8	0.23	1.3	0.30
950915	600	0.70	6.8	0.34	2.3	0.42
950916	750	0.50	8.5	0.42	3.6	0.57

Vertical air velocity vs. calculated reflectivity. Further insight into the relationship between vertical air motion and reflectivity can be obtained by separating the total calculated reflectivities into those due to cloud droplets and drizzle drops. As was already pointed out, $(Z_{calc})_{twodc}$, the calculated reflectivity for drops >50 μm (from the 2D–C probe) is positively correlated with Z_{obs}, (rightmost column of Table 2), but there is no correlation between $(Z_{calc})_{fssp}$ and Z_{obs}. Similarly, there is no correlation ($r<0.1$) between the measured air velocity, w, and $(Z_{calc})_{fssp}$ (using 10–Hz FSSP data). However, significant correlations are found between w and $(Z_{calc})_{twodc}$ as shown in Fig. 9. The individual points in this graph represent between 30 and 70 pairs of values, each value being an average over roughly 90 m horizontal distance in the cloud. Except for the points from level flight segments (filled circles), data from 3 to 5 separate cloud regions are combined at all levels; in spite of that, the degree of coherence in the data can be said to be quite good. Perhaps more remarkable is the fact that the w vs. $(Z_{calc})_{twodc}$ correlation shows the same sign reversal with altitude as was seen for V vs. Z_{obs} in Fig. 7. Negative values prevail below cloud base and positive values dominate though most of the cloud depth. Examinations of Z_{calc} vs. w scatter–plots reveal that, similarly to Fig. 8, the correlation coefficients are not dominated by a small number of extreme values.

The two sets of analyses just discussed, w vs. Z_{obs} and w vs. $(Z_{calc})_{twodc}$, indicate that upward transport of drizzle drops is one source of the positive correlation between reflectivity and velocity in the upper reaches of the clouds. However, an additional contribution to that relation derives from the downward motion of parcels diluted by entrainment mixing.

Diluted downward plumes. One indication for downward moving parcels with stronger than average velocities is seen in the few points with large negative air velocities and weak reflectivities in Fig. 8; in terms of V the downward velocities would be even stronger. Even stronger, descriptive evidence for the downward motion of diluted parcels is shown in Fig. 10 where narrow reflectivity and velocity ranges are highlighted for the images of Fig 4. The highlighted reflectivities are relatively low values, and they are surrounded by higher reflectivities. The highlighted velocities are nearly the largest negative values for the entire field, and these regions are surrounded by smaller negative velocities. Many of the highlighted reflectivity zones extend downward from cloud top and suggest downward penetrating plumes. In most cases this is confirmed by the velocity pattern. There are particularly striking examples of the these plumes at the horizontal locations 2700, 3400 and 4500 m in Fig.10a. In these instances the plumes start at cloud top, extend downward more than 200 m, and terminate less than 100 m above cloud base. The general prevalence of high–velocity regions in the lower parts of the images is, of course, due to the larger fall velocities acquired by the growing drops.

Detection of the downward incursions in the hydrometeor data from the in situ probes is made elusive by the small, 50–100 m, sizes of the regions. Only 5 to 10 data points are registered by the

FSSP probe over that distance, and the 2D imaging probe has no useful resolution on that scale for the low drizzle drop concentrations prevailing in these clouds. As mentioned before, at lower levels in the clouds no correlations exist between the reflectivity due to cloud droplets and the vertical air velocity; the diluted plumes represent too small a fraction of the total volume, and conditions in them deviate from the means so slightly, that their effect is not discernible in terms of correlations. Some relatively clear examples of the phenomenon have been found near the tops of the clouds. Fig. 11 shows two such examples from slow traverses of the cloud tops. In the first example (Fig. 11a), a region of low reflectivities is seen between 300 and 400 m horizontal distance; corresponding low vertical air velocities are seen in the upper panel. This feature occurred only about 10 m below the altitude where the aircraft emerged from the cloud at 750 m horizontal distance. The second example (Fig. 11b) covers a larger horizontal region from a descent into cloud at an approximate rate of 50 m altitude loss per kilometer of horizontal travel. A number of interesting points are shown by these data. The temperature minimum occurs well into the cloud, about 50 m below the altitude of cloud entry. Sharp decreases in velocity, with accompanying decreases in LWC and in reflectivity are seen at 0.9 km, and in three interrupted segments between 2.8 and 3 km. The latter segment is 130 m below cloud top. These are patterns expected for diluted mixtures. It may also be noted that the incursion at 0.9 km is associated with a rise in temperature while the incursions at 2.8–3 km are associated with decreases in temperature; this results from the fact that the aircraft is descending through the inversion, so that temperature is increasing with time (decreasing altitude) at 0.9 km while the gradient is the opposite at 2.8–3 km.

Upward transport of drizzle. The conclusion that can be drawn from the empirical evidence in Fig. 7 and from the foregoing analyses (remembering that all observed values of V are negative) is that the positive correlation between Z and V in the upper parts of the clouds is due to a combination of two causes: upward transport of drizzle drops and the downward motion of regions diluted by entrainment. We are unable to make a rigorous separation between the contributions made these two processes. However, positive correlations of both the observed and calculated reflectivities with vertical air velocity, the substantial difference in reflectivities associated with upward and downward air motions, and the absence of correlations between w and $(Z_{calc})_{fssp}$ all indicate that the upward transport of drizzle drops is likely to be the stronger contributor.

Thus far the upward transport of drizzle drops was characterized in terms of reflectivity. Clearly, the transport should also be evident in terms of number concentration and in terms of mass of the drizzle drops as well. To demonstrate that indeed this is the case, the correlation between vertical air velocity and the mass concentration of drizzle drops, LWC_{twodc}, is shown in Fig. 12 for one of the study days. This plot can be compared with the right–most panel in Fig. 9. Just as in terms of reflectivity, negative correlations dominate below cloud base and positive ones in most of the cloud layer. The largest positive values are found just above the middle of the cloud. The decreased correlations near cloud top are due, at least in part, to the poor sampling of drizzle drops in that region by the in situ probes. More will be said about these correlations in Section 8.

The radar data indicate that upward transport of drizzle drops is present on scales at least as small as about 4–5 m, while the in situ data show a similar pattern on scales of around 90 m. Our in situ measurements of drizzle drop concentrations do not have sufficient resolution to examine fluxes on scales comparable with the radar data. It is also beyond the scope of this study to comment on the spectral distribution of turbulent transport or the magnitudes of the fluxes.

6. Liquid water content.

As shown in the soundings of Fig. 2, the LWC[5] profiles on all three days exhibit the usual triangular profile. There are, however, significant differences to be noted. In Fig. 13 the LWC measurements are presented in greater detail and the observed values are compared with those expected for a saturated parcel lifted adiabatically from cloud base. In each case, data are combined from three to five ascents and descents through the cloud layer. Mean, and 50– and 90–percentile values of LWC are shown. All values are averaged over the time spent by the aircraft in the given altitude intervals so that zeros are also included. Except for altitudes above 540 m, 650 m and 860 m (the last two points on each profile) and below cloud base for 950914 (330 m), the fraction of flight time with non–zero LWC values exceeded 95%. This confirms the visual continuity of the clouds and indicates that the observed decreases in LWC with respect to adiabatic values near cloud top did not result from averaging over cloudy and clear zones. The total lengths of the flight segments represented by data points in each height interval are about 3 – 6 km.

For 950915 and 950916 the profiles are close to the adiabatic values from cloud base to about 2/3 of the cloud depth. For 950914 the observed profile is almost totally incompatible with the notion of parcel lifting; this case will be examined in more detail in Section 10.

The data in Fig. 14 were derived from the FSSP probe and have 10–30 % probable errors. For the flight of 950914 data are also available from the CSIRO probe; data from this probe show the same profile and have even less variability. However, the LWC values from the CSIRO probe are only about 68% of the values derived from the FSSP, with the relationship $LWC_{csiro} = 0.63 \cdot (LWC_{fssp}) + 0.02$. The major mass contribution in these clouds comes from near 30 μm diameter droplets at all altitudes; there are no obvious shortcomings of either instrument for droplets of those sizes, so the source of the difference between the two instruments remains unexplained. This uncertainty in the LWC measurements indicates that the actual LWC was perhaps not as close to the adiabatic values as is depicted in Fig. 14.

Another aspect of the difference between 950914 and the other days can be seen in the variabilities of the observed LWC values. Vertical profiles of the variances of the LWC measurements are shown in Fig. 14 expressed as fractions of the means for given heights and using the normalized cloud depth parameter ϕ. While not shown, the dispersion profiles for 950916 are identical to those of 950915. The sharp increase in dispersion for $\phi > 0.6$ on 950914 is in remarkable contrast with the nearly constant values observed on the other days. The CSIRO probe data yield even lower dispersion values than the FSSP data (in spite of using 30 Hz CSIRO data versus 10 Hz FSSP data) further underscoring the uniformity of the LWC for given altitudes.

In contrast with the uniformity of LWC, the number concentrations of cloud droplets exhibit great variability, with dispersion values up to and exceeding 100%. This variability is offset, however, by a strong negative correlation ($r \approx -0.7$) between number concentration and mean droplet size. This fact was also noted by Hudson and Li (1995).

7. Size distribution.

The concentrations of cloud droplets exhibit different vertical profiles for the different days. These data are shown in Fig. 15 for 950914 and 950915. As for the LWC plots, the indicated values are averages over the entire duration of flight in each height interval, including zeros where they

---

5. The contribution of drizzle to the LWC is always small so that the LWC essentially reflects the mass of cloud droplets (<50 μm diameter).

occur (only at $\phi = 0.9$ and 1.0, and at $\phi < 0$). Maximum concentrations were 100–120 cm^{-3} on the first and third days, while the day in the middle had concentrations reaching 200 cm^{-3}. Highest concentrations occurred at $\phi \approx 0.8$ on 950914 and at $\phi \approx 0.5$ on the other two days; as will be seen, this is due to the differences at the small ends of the size spectra.

Size spectra, averaged over level flight segments are shown in Fig. 16 for the first two days. Data from the FSSP and 2D–C probes are combined in these diagrams. The breaks near the middle of the curves correspond to the change from one probe to the other; it is unresolved to what extent the breaks are real and to what degree they result from undersampling of drops in the smallest size interval used for the 2D–C probe (50–100 μm). The spectra for the two days differ in two important respects. First, while the concentrations of the smallest droplets remain high for all altitudes on 950914, there are significant decreases from the peak values on 950915 and the decreases become more pronounced with increasing altitude. Diminished concentrations of small droplets with time is expected for condensational and coalescence growth. We do not have an explanation for the source of the smallest droplets found at all heights on 950914. Second, there are substantial increases in the concentrations of drizzle drops with decreasing altitudes on 950914; corresponding changes on 950915 are barely perceptible. The growth observed on 950914 is consistent with the presence of cloud droplets below the main cloud base (330 m, $\phi=0$) leading to continued growth of drizzle drops by coalescence.

Using data from the combined soundings, changes in the average size spectra with altitude can be depicted as in Fig. 17. In both cases the concentrations of drizzle drops increase from the top down. The concentrations of cloud droplets in each size category increase upward consistent with droplet growth. The first three size channels show an exception to this pattern for 950915. Drizzle drop concentrations in the range 50–150 μm diameter were higher on 950914 by factors of about 2. The two sets of data are nearly identical in the size range 25–45 μm.

Precipitation rates near cloud base, calculated from the in situ probe data, were in the range of 0.05 – 0.01 mm h^{-1} on both days. Below cloud base the rate increased to 0.015 mm h^{-1} on 950914.

8. Velocity variances and correlations.

The observed variances of vertical velocities reveal some differences among the study days. The variances of the Doppler velocities $var(V)$ and of the air velocities $var(w)$ are shown in Fig. 18a–c. Sampling rates for these two quantities are nearly the same (30 and 20 Hz). Peak values of $var(V)$ occur at about 2/3 cloud depth and have comparable values of ≈ 0.05–0.07. Profiles of $var(w)$ have maxima near the middles of the cloud layers on all three days but the values are about only half as large for 950914 than for the other two days . Especially on 950915 and on 950916, $var(w)$ is considerably greater than $var(V)$. This is not surprising in view of the negative correlation between w and drizzle drop concentration, plus the fact that V is determined by the velocities of the drizzle drops.

The skewness of the air velocity and Doppler velocity distributions (right–hand panels in Fig. 18) have similar vertical variations and have comparable values. This is somewhat surprising in light of the fact that the aircraft data for w are composites for entire flights while the radar measurements of V shown in these figures are relatively short data segments. For all three days, negative skewness values prevail within the cloud layers and positive ones below cloud base. Negative values within the cloud are consistent with the likely source of in–cloud turbulence being at cloud top, while positive values below cloud base are to be expected to be associated with an upward buoyancy flux.

The variance of the Doppler velocity in the horizontal, $var(V_h)$, was also evaluated for some flight segments at constant altitudes and with the antenna in the side–looking mode. These results

are shown in Table 3 along with values of $var(w)$ and of $var(V)$ for the same altitudes from Fig. 18. In spite of scatter, in part due to the lack of simultaneity in the measurements of the various parameters, it is clear that the $var(V_h) > var(V)$ and that $var(V_h) \approx var(w)$. The latter near–equality supports the validity of the measurements, because it is consistent with the expectation that V_h and w have similar distributions in nearly isotropic turbulence.

Table 3. Variances of horizontal and vertical velocities

Date	Altitude (m)	Norm. cld. depth. ϕ	$var(w)$	$var(V)$	$var(V_h)$
950914	460	0.59	0.07	0.05	0.09
	300	−0.14	0.02	0.02	0.08
	160	−0.77	−	0.01	0.03
950915	600	0.70	0.14	0.05	0.07
	480	0.33	0.10	0.05	0.10, 0.14
950916	780	0.59	0.12	0.07	0.15
	630	0.15	0.07	0.06	0.16

As a summary, and as reinforcement for the connections between air motions and hydrometeor populations already discussed, correlations between the vertical air velocity w and other parameters are indicated in Table 4. Level flight segments without turns have been used for these analyses. The highest resolution available was used for each parameter: 30 Hz for w and for temperature, 10 Hz for FSSP and 1 Hz for 2D–C data. To match the slower parameters, w was re–sampled after filtering with an 8th order non–recursive low–pass filter with a cutoff frequency of 4 or 0.4 Hz.

The correlations between w and temperature are generally weak, but they do show a systematic sign reversal between in–cloud and below–cloud values. While we have not attempted to quantify the fluxes, it appears to us that heat fluxes were relatively small in the clouds examined, were opposed by stability below the main cloud on 950914, and were inhibited even in the unstable layer around 480 m ($\phi=-0.29$) on 950916.

Table 4. Correlations with air velocity (w)

	950914			950915		950916		
Altitude (m)	460	300	155	600	480	780	630	480
Norm. cld. depth, ϕ	0.59	−0.14	−0.77	0.7	0.33	0.59	0.15	−0.29
Temperature	0.21	−0.13	−0.21			0.32	0.19	−0.10
Drop concentration	0.58	0.30	−0.13	0.39	0.44	0.29	0.44	−
Mean drop size	−0.53	−0.26	−0.04			−0.23	−0.38	−
LWC_{FSSP}	0.16	0.06	0.07	0.21		0.0	0.0	−
LWC_{CSIRO}	0.30	−0.01	−0.15					
Drizzle conc.	0.44	−0.04	−0.03	0.45		0.42	0.27	−0.11
Drizzle mass	0.50			0.42		0.45		

Empty boxes indicate data not available or not calculated
Dash (−) means that no cloud was present.

The relation between vertical velocity and cloud droplet concentration deserves an additional note. While the scatterplots of most other pairs of parameters appear relatively uniformly spread across the range of values, the droplet concentration vs. vertical air velocity plots have characteristic 'golf club' shapes, as shown in the top panels of Fig. 19 with each point representing about 10 m of horizontal distance through the cloud. As these diagrams indicate, negative air velocities are associated with low droplet concentrations, while at positive air velocities the droplet concentrations cover a large range, to maxima well above the mean values. The lower panels in Fig. 19 indicate how these patterns translate into frequency distributions for points with air velocities that differ from the mean by more than one half standard deviation. There are considerable differences between the pairs of distributions for upward and downward air velocities, specially in the tails toward large concentrations. For each of the three data sets shown in Fig. 19, the lowest altitude has been chosen for which adequate data were available. For 950915 and 950916, data from higher altitudes were also examined; these show the same patterns but the distributions for positive w do not extend to as high values as at the lower altitudes. These results are consistent with the creation of new cloud droplets at cloud base in upward moving parcels as has been seen already in the size distributions shown in Section 7. The correlation with w confirms the role of upward air motions in the formation of new drops. Closely coupled with these results are strong negative correlations between droplet concentrations and average droplet sizes, leading to relatively modest variations in LWC at any given altitude.

9. Horizontal scales

Scales of horizontal variation of echo intensity and Doppler velocity were examined using Fourier spectral analysis of up–looking radar data during straight, constant–altitude aircraft passes at

or below cloud base. Fig. 20 presents data from one such pass on each of two of the study days. Spectral and co–spectral densities were calculated for each range gate that had continuous data, then combined as contour plots in Fig. 20. Although originally calculated as functions of frequency, the values are contoured here in the spatial domain of altitude and wavelength (true airspeed/frequency). The base–10 logarithms of spectral density for Z and V are contoured in the first two panels of each figure; negative values correspond to magnitudes less than 1. The $Z–V$ cospectral densities are contoured in the last panel. The cospectra have the same signs as the corresponding correlation coefficients (Fig. 6), with the dominant values being positive in the upper cloud layers and negative in the sub–cloud layers.

On 950914 the horizontal scales of variation change with altitude. The Z and V spectra and the $Z–V$ cospectra are strongest at wavelengths of about 300 m in the upper cloud layer (370–520 m; see also Fig. 2a), and about 1000 m in the layer below that. As shown in Fig. 4a, the change in scale probably resulted from the fact that not all of the high reflectivity areas in the upper cloud layer had corresponding high reflectivity areas in the layer below. The most likely cause of this is the strong shear, and the fact that the vertical plane sampled by the radar was not lined up with the wind direction, resulting in spread–out precipitation trails crossing into the sample plane. In contrast, on 950916 there was no directional shear, so that nearly all the high reflectivity areas were continuous from the cloud layer to the sampling level. The resulting spectra and cospectra show the strongest scale of variation to be about 500 m at all heights (Fig. 20b).

These analyses are relatively simple attempts at characterizing the echo structure. Brief looks at parameters other than radar reflectivity, which is principally a reflection of the spatial distribution of drizzle, revealed no structural characteristics, but this aspect needs further examination. The influence of the relative orientation of the flight line with respect to the winds also needs more detailed attention. Furthermore, the horizontal echo maps (Fig. 5) offer opportunities for more detailed analyses than those included here.

10. Discussion

Some comments are in order to round out the information given in Section 3 regarding general conditions during the three days of the case studies. The coastal stratus cases described here differed from the thermodynamic characteristics frequently associated with marine stratocumulus most importantly in that air immediately above cloud top and to some distance beyond the inversion top was not dry; in fact, mixing ratios changed little across the inversion in our cases. In addition, on the first day, the cloud layer was advecting into the region above a deep stable layer; other than that the boundary layers were well mixed. Wind profiles varied remarkably during the three days: near–surface winds veered from southerly to westerly, winds above the inversion veered from NNE to E, and winds in the cloud layers backed from N to NW. Windshear was always strong across the inversion and was also strong in the subcloud layer on the first day. With respect to radiational forcing, the three days were quite similar, as all three sets of observations were made during the late morning hours and there were no upper level clouds in any of the cases.

In the following paragraphs, specific topics are taken up to round out the analyses presented in the preceding sections, and to compare the findings with those of other authors.

The 950914 case. The cloud studied on 950914 had the most unusual features which deserve some additional discussion. First of all, this cloud was cut off from moisture supply at the surface by the stable layer between the ocean surface and 300 m. The air temperature measured at the lowest flight level (65 m) was 12°C on this day, 2°C colder than either the day before or the two subsequent days. While we have no measurements of sea surface temperature from the flight location, buoy and ship data from within a 100–km region support the assumption that there was a brief incursion or

upwelling of cold water in the area on 950914. Evidently, the cloud above the stable surface layer was advected into the region and was precipitating. About 7 hours would be required to deplete the water content of the cloud at the observed precipitation rate. Traveling with a speed of 6 m s⁻¹, the cloud would move 150 km over that period. That is about four times the extent of the study area. Temperature within the cloud at any level had a N–S gradient of about 0.5°C per 10 km which translates (at 6 m s⁻¹ wind speed) to a cooling of -1.1°C h⁻¹. However, this cooling was offset by the warming of $+1.1$°C h⁻¹ that was evident in the temperature measurements when returning to given locations over the study period. The net effect on a parcel of cloudy air advected toward the south would be roughly no temperature change. The accuracy of these heating and cooling rates is relatively poor, since they are obtained from data collected during a complex flight pattern. In fact, the apparent steady state of the cloud is readily explained by an overall cooling, by radiation and by mixing with cold air near the sea surface, of only about 0.1°C h⁻¹. That much cooling is sufficient to offset depletion by precipitation.

Other surprising features of the 950914 case were the presence of cloud within the low stable layer and the monotonic LWC profile from the surface to the top of the main cloud. Cooling from the sea surface was no doubt producing the positive temperature gradient within the stable layer and was deepening it, while at the same time the main cloud layer was getting 'eroded' from the base up. The Richardson number within the stable layer is about 0.9, indicating the possibility of dynamic instability and enhanced vertical mixing. Thus, the observed structure is probably a combined result of cooling within the stable layer, maintaining saturated conditions there in the manner of an advection fog, and of mixing with the main cloud layer above it.

Although the wind shear within the stable layer extended into the lower few tens of meters of the main cloud on 950914, the turbulence generated by this within the main cloud layer was less intense than that generated by buoyancy forces on the other two study days. Evidence for this is seen in the roughly factor 2 lower values of *var(w)* on 950914 than on the other days (cf. Fig. 18).

The correlations (cf. Tables 2 and 4) between *w* and temperature and hydrometeor parameters are not significantly different for this day from values obtained for the other days.

Drizzle. One general characteristic of the coastal stratus we studied was the prevalence of drizzle. Drizzle drops, in concentrations corresponding to precipitation rates up to 0.2 mm h⁻¹ were found in 10 of the twelve clouds sampled on that many different days. The cases with drizzle included a large range in droplet concentrations (160 – 800 cm⁻³) with no clear correlation to drizzle rate. Cloud depths varied between 150 and 500 m; shallower clouds produced lower drizzle rates. A similar conclusion regarding high drizzle frequency was reached by Fox and Illingworth (1997) based on in situ observations in stratocumulus around the Azores and around the British Isles. Our data confirm, with some qualifications, their finding that the 95 GHz reflectivity is dominated in stratus and stratocumulus by drizzle drops in spite of the minor contribution they make to LWC. As shown in our Fig. 6 for the three cases here described, the reflectivity from cloud droplets exceeded that due to drizzle drops only in the upper 50–150 m of the clouds.

Comparing the three cases of this paper, we find fairly similar characteristics with respect to cloud and drizzle drop populations. Total cloud droplet concentration was lowest on the first day; this may have been a reflection of depletion rather than of air mass origin. The cloud and drizzle drop size distributions were nearly identical (Fig. 17), except for the puzzling increase of the concentrations of smallest droplets with altitude on 950914. Maximum drizzle drops sizes were 300 μm diameter on all three days. The basic characteristics of the profiles of drizzle concentrations (Fig. 17), reflectivities (Fig. 6), and correlations with air velocity (Fig. 9) are also invariant from day to day. Median drizzle rates near cloud base were approximately 0.01 mm h⁻¹ for all three days and decreased by about a factor 5 toward cloud top. Maximum values for 1–s (90–m) averages of the

drizzle rate were in the range 0.1 to 0.2 mm h⁻¹. The mass concentration of drizzle drops had median values of 5 to 8 · 10⁻³ g m⁻³ at cloud base, and decreased upward in a manner similar to the drizzle rate. The 1–s values for both drizzle rate and mass concentration show large scatter due to the small sample volume of the 2D–C probe. A better estimate of the variability in drizzle rate can be obtained from the reflectivity statistics shown in Fig. 7 using the unity exponent for the *Z–R* relationship quoted in Section 5.

The size distribution of drizzle drops remains somewhat uncertain in this work due to the instrumentation problems mentioned in Section 2. We appear to share this problem with others who use similar instruments; for example, the spectra obtained by Boers et al. (1996) show the same inflection near 50 μm diameter as our data. That this is not necessarily an artifact is given some support by the relatively good match between calculated and measured spectra obtained by Austin et al. (1995).

Upward transport of drizzle drops. Perhaps the most significant result emerging from our observations is the observed positive correlation between radar reflectivity and Doppler velocity (negative for downward velocities) in the upper regions of the clouds. This reversal from the negative correlation expected, and found, in the lower cloud regions and below the clouds, as well as the correlations found between in situ measurements of air velocity and drizzle drop concentration and mass, indicate an upward transport of drizzle drops through most of the depth of the cloud layer. The upward drizzle flux appears to be strongest near the middle of the cloud layer. Areas of upward transport (higher reflectivities) appear to have a broad range of horizontal extents and have irregular shapes. The radar data indicate the existence of regions of upward transport down to scales of 4 m; the supporting evidence derived from the in situ data is valid for scales down to about 90 m. At this time we are unable to deduce greater detail about the spectral characteristics of the flux, or to reliably estimate its total magnitude.

It may be noted that Hudson and Li (1995) found no correlation between vertical velocity and drizzle drop mass in two rather different cases of stratocumulus. This conflict is surprising because results from the two data sets are quite similar on several other points: positive correlations between vertical velocity and cloud droplet concentrations, negative correlations with average droplet size, and no correlations with cloud liquid water content. Possible reasons for the difference are that lower LWC was found in the cases observed by Hudson and Li (1995), and that their determination of drizzle mass relied on in situ probes only.

Cellular structure. The radar images (Figs. 4 and 5) show that apparently homogeneous stratus layers can have significant cellular structures and that this structure is present in quite similar forms from case to case, in spite of significant differences in stability and wind conditions. The dominant horizontal scales of the cells were somewhat greater than the depths of the cloud layers, but were only about half of the depths of the total boundary layer for the three days analyzed. Horizontal sections of the cells (Fig. 5) reveal intricate shapes, tending toward fluted rather than lobed boundaries of the high reflectivity cores. There is some suggestion for wave organization on one day (950914; Fig. 5a), but this evidence is not strong. No linear organization can be noted on the other days.

The cellular structure here reported has some resemblance to the fine–scale structure of the echoes described by Miller and Albrecht (1995). However, those data originated from a situation in which cumulus were interacting with stratocumulus, and which produced updrafts and rainfall rates an order of magnitude greater than those described in this paper. The 'microcells' described by Kropfli and Orr (1993) were isolated, long–lived and had definite updraft cores. There is also some similarity with the echo cells described in Vali et al. (1995); weak convective buoyancy was believed to have been the driving force in that case. Nicholls (1989) diagnosed vertically coherent downdraft regions

in stratus, and linked that observation to the cellular visual appearance of the cloud sheets. Furthermore, he determined the widths and frequencies of the downdraft regions as a function of distance below cloud top and showed that the observations can be matched to model simulations of a random traverse through hexagonal cells with a spacing of 0.6 times the depth of the mixed layer and with gaps between them 0.2 times the cell size. Downdraft occupied 40% of the area near cloud top and about half that near cloud base.

The spacing of echo cells in our cases (cf. Section 9) are comparable to the thickness of the cloud layer. Since the cloud layers were 1.0, 0.47 and 0.55 times the depths of the mixed layers for the three days, the cell sizes in our cases are larger than those diagnosed by Nicholls (1989). Also, while we did not determine the fraction of area occupied by downdrafts, it is clear from Figs. 10 and 11 that near cloud top this number would be considerably smaller than the 40% given by Nicholls (1989). The main difference between the two sets of data is in cloud top instability, as will be discussed later. The diluted regions identified in Fig. 10 tend to change little in horizontal extent at first, then spread rapidly some distance away from the cloud top; this pattern has a degree of qualitative agreement with the observations of Nicholls (1989).

The observed pattern in radar echoes reflects the distribution of drizzle drops. In all cases and at all altitudes the pattern is dominated by drops >30 μm diameter; in the lower parts of the clouds that size shifts to 150–200 μm. Reflectivity values range over roughly 10 dBZ at given altitudes. As shown in Section 5, reflectivity and precipitation flux are roughly proportional in these clouds, so that the echo patterns can be viewed as directly representing the distribution of drizzle intensity. How the uneven distribution of drizzle depends on and in turn influences other characteristics such as radiative fluxes, cloud breakup, thermal perturbations, etc. is clearly an important question.

The origin of the cellular echo patterns cannot be ascertained from the data on hand. It is specially intriguing that for the three case studied the internal structures are qualitatively quite similar in spite of rather different dynamical conditions of the clouds. It is possible that wind shear at cloud top or gravity waves above the inversion were the common cause of the cellular structures. Another possibility is that weak buoyant fluxes on the last two days and disturbances induced by wind shear below the cloud on the first day (950914) had comparable effects, though this would appear to be too much of a coincidence. Yet a third possibility is that positive feedback through the drag of the larger drops reinforces initially small variations in the growth rate or concentration of drizzle drops. The broader question of the origin of TKE in these clouds is clearly also relevant to the cellular organization – this point is taken up next.

Turbulence and entrainment. Since our data were not collected with turbulence studies in mind, only limited conclusions are warranted on this point . With that caveat, we venture into some speculations about the principal source of energy and hence the controlling factor for the observed turbulence, principally in order to examine relationships to the cellular echo structure.

For cloud situations that were in many ways similar to those here described, Nicholls and Leighton (1986) concluded that turbulence was maintained by radiatively driven convection from cloud top. Two 'signatures' supporting that deduction were that the mixed layers did not extend all the way from cloud top to the surface, and the particular forms of the profiles of *var(w)* and of *skew(w)*. We can compare our data with theirs on these two points. In our cases too, neutral stratification prevailed within the cloud layers. On one day (950915) the mixed layer extended to the sea surface, while the other two days had more complex stratification below the cloud. The *var(w)*–profiles shown in Fig. 18 are very similar to those of Nicholls and Leighton, and the *skew(w)* is negative within the cloud layer in both sets of data. This pattern also agrees with that reported by Moyer and Young (1991) for their flight B from the FIRE project, and with that of Frisch et al. (1995). In the latter report, we can compare with the statistics given for the Doppler velocity, since drizzle

was negligible in their cases and therefore $V \approx w$. It thus appears that the *var(w)* and *skew(w)* profiles are quite robust features of stratus and of stratocumulus. In all, we believe that sufficient similarities exist between our cases and those of Nicholls and Leighton and of Moyer and Young to apply their conclusions about the importance of radiative cooling in producing turbulence to the clouds we observed. However, there are also important differences between our cases and those of Nicholls and Leighton: there was little wind shear across the inversion, and drier air capped the clouds in their cases. The windshear across the inversion was between 0.06 and 0.08 s^{-1} (over 80–100–m height intervals) in our cases, with Richardson numbers around 0.3; this raises the possibility that shear–induced turbulence was also an important factor. In addition to shear at the inversion, shear was also present in the stable layer below the cloud on 950914 (like in flight 564 of Nicholls and Leighton). With respect to the changes across the inversion, positive θ_E–jumps and small q–jumps indicate that there was no thermodynamic instability at cloud top in the clouds we studied. Even the simplified instability condition $\Delta\theta_E < b\,\Delta q$ (b=0.57 ... 1.7), which is not considered very restrictive (cf. MacVean, 1993; Duynkerke, 1993), is not satisfied in any of the cases, since $\Delta\theta_E$ –values range from +8 to +10 K and $\Delta q < 0.6$ g kg^{-1}. Thus, the strength of entrainment was certainly much less in our cases. In all, indications are that turbulence induced by evaporative cooling had a smaller role in these clouds than that derived from shear forces.

We do have evidence, in the radar images and in several aspects of the in situ measurements, that entrainment was taking place. The radar data of Fig. 10 show diluted parcels with relatively large downward velocities. In situ observations consistent with entrainment include (i) reduced values of LWC and increased values of *var(LWC)* near cloud top (Fig. 14), (ii) positive correlations near cloud top between *w* and Z_{calc} (Fig. 9), and between *w* and other parameters (Table 4), and (iii) traces showing downward moving air of reduced hydrometeor content (Fig. 11).

The diluted regions detected in this work are compatible in most respects with those described by Rogers and Telford (1986), Khalsa (1993), Wang and Albrecht (1994) and by Gerber (1996) among others . It is to be noted though, that these similarities exist even though thermodynamic entrainment instability was present in the comparison cases while our cases had none.

11. Conclusions.

Observations were made in stratus over the upwelling zone off the Oregon coast with an aircraft equipped with in situ sensors and a 95 GHz radar. Measurements for three consecutive days were presented in this paper. Thermal stratification and wind conditions changed significantly during that period thus allowing differences and similarities to be exploited in search of underlying causes. The clouds were unbroken, with no detectable horizontal structure in parameters other than drizzle.

The observations here reported provide essentially a 'frozen' description of cloud structure, in images and in statistical parameters. In situ measurements, taken along lines through the clouds, were extended by the radar data to horizontal and vertical planes. Conversely, the reflectivity and velocity fields detected by the radar were interpreted in light of the air motion and drop size distribution data from the in situ probes. In other words, the radar data provided a greater wealth of information than the in situ measurements along a line, and the ambiguities of reflectivity measurements were significantly reduced with the help of the simultaneous in situ measurements. Such combined data overcomes many of the problems and limitations identified, for example, by Davis et al. (1996) in the use of LWC data for examining scales of variation in stratocumulus.

The observations we report are consistent, in a general sense, with the model, also suggested by other authors, of broad regions of net upward fluxes and narrow entrainment regions of stronger downward motions. Our data refine this model in three respects. First, we show that the upward flux is most significant for drizzle drops over the size range 50 to 300 μm diameter, not for LWC made

up by smaller cloud droplets. This difference has important implications regarding the way the upward transport is envisaged to come about, and certainly lessens the applicability of parallels between stratus and cumulus. Second, it is clear from the radar images that the regions of upward transport have irregular shapes over a large range of sizes. Third, we show that downward moving diluted regions existed in the clouds we examined, in spite of the absence of thermodynamic instability at cloud top. Especially in one case, and to lesser degrees in the other two, turbulence generated by wind shear might have been responsible for the initiation of entrainment.

Structures revealed by the kinds of radar echoes shown in this paper appear to provide a good basis for examining the degree and the scales of variability of drizzle in stratus and stratocumulus. The reflectivity images are nearly equivalent to images of precipitation concentration. It is clear that, through the many ways that drizzle interacts with other cloud properties, local variations in drizzle have significant impacts on a broad range of cloud characteristics and are of importance for the time evolution of the cloud. On the other hand, since drizzle represents a small fraction of the total water content of the cloud, effects of the drizzle structure are not felt in the instantaneous values of properties like liquid water path (LWP) or albedo.

While we find the results here presented solidly supported by our data, undoubtedly, these observations need to be confirmed, and their range of validity delineated, by cases from a broader range of conditions. The conclusions drawn need elaboration and integration in model simulations both with respect to dynamical and microphysical factors. At the same time, these observations might be helpful in providing ideas and realistic constraints to model calculations.

REFERENCES

Austin, P. H., Y. Wang, R. Pincus and V. Kujala, 1995: Precipitation in stratocumulus clouds: Observation and modeling resuts. *J. Atmos. Sci.*, **52**, 2329–2352.

Baker, M. B., 1993: Variability in concentrations of cloud condensation nuclei in the marine cloud–topped boundary layer. *Tellus Ser. B – Chem. Phys. Meteor.*, **45**, 458–472.

Baumgardner, D. and A. Korolev, 1997: Airspeed corrections for optical array probe sample volumes. *J. Atmos. Ocean. Techn.*, (in print).

Boers, R., J. B. Jensen, P. B. Krummel and H. Gerber, 1996: Microphysical and short–wave radiative structure of wintertime stratocumulus clouds over the Southern Ocean. *Quart. J. Roy. Meteor. Soc.*, **122**, 1307–1339.

Boers, R., J. D. Spinhirne and W. D. Hart, 1988: Lidar observation of the fine–scale variability of marine stratocumulus clouds. *J. Appl. Meteor.*, **27**, 797–810.

Brenguier, J. L., 1989: Coincidence and dead–time corrections for particle counters. Part II: High concentration measurements with an FSSP. *J. Atmos. Ocean. Techn.*, **6**, 585–598.

Brenguier, J. L. and L. Amodei, 1989: Coincidence and dead–time corrections for particle counters. Part I: A general mathematical formalism. *J. Atmos. Ocean. Techn.*, **6**, 575–584.

Bretherton, C.S. and R. Pincus. 1995: Cloudiness and marine boundary layer dynamics in the ASTEX Lagrangian experiments. Part I: Synoptic setting and vertical structure. *J. Atmos. Sci.*, **52**, 2707–2723,

Browning, K. A., A. Betts, P. R. Jonas, R. Kershaw, M. Manton, P. J. Mason, M. Miller, M. W. Moncrieff, H. Sundqvist, W. K. Tao, M. Tiedtke, P. V. Hobbs, J. Mitchell, E. Raschke, R. E. Stewart and J. Simpson, 1993: The GEWEX Cloud System Study (GCSS). *Bull. Amer. Meteor. Soc.*, **74**, 387–399.

Cahalan, R. F., W. Ridgeway,Wiscombe, W. J., T. L. Bell and J. B. Snider, 1994: The albedo of fractal stratocumulus clouds. *J. Atmos. Sci.*, **51**, 2434–2455.

Cahalan, R. F. and J. B. Snider, 1989: Marine stratocumulus structure. *Remote Sens. Environ.*, **28**, 95–107.

Clothiaux, E. E., M. A. Miller, B. A. Albrecht, T. P. Ackerman, J. Verlinde, D. M. Babb, R. M. Peters and W. J. Syrett, 1995: An evaluation of a 94–GHz radar for remote sensing of cloud properties. *J. Atmos. Ocean. Techn.*, **12**, 201–229.

Davis, A., A. Marshak, W. Wiscombe and R. Cahalan, 1996: Scale invariance of liquid water distributions in marine stratocumulus .1. Spectral properties and stationarity issues. *J. Atmos. Sci.*, **53**, 1538–1558.

Duroure, C. and B. Guillemet, 1990: Analyse des hétérogénéités spatiales des stratocumulus et cumulus. *Atmos. Res.*, **25**, 331–350.

Duynkerke, P. G., 1993: The stability of cloud top with regard to entrainment – amendment of the theory of cloud–top entrainment instability. *J. Atmos. Sci.*, **50**, 495–502.

Fabry, F., 1996: On the determination of scale ranges for precipitation fields. *J. Geophys. Res. – Atmos.*, **101**, 12819–12826.

Feingold, G., B. Stevens, W. R. Cotton and A. S. Frisch, 1996: The relationship between drop in–cloud residence time and drizzle production in numerically simulated stratocumulus clouds. *J. Atmos. Sci.*, **53**, 1108–1122.

Frisch, A. S., C. W. Fairall and J. B. Snider, 1995: Measurement of stratus cloud and drizzle parameters in ASTEX with a K–alpha–band Doppler radar and a microwave radiometer. *J. Atmos. Sci.*, **52**, 2788–2799.

Galloway, J., Pazmany, A., McIntosh, R., Kelly, R., and Vali, G., 1996: MM–wave airborne cloud radars. Proceedings CP–582, *Remote Sensing: A valuable source of information*, Touluse, France, Advisory Group for Aeospace Research and Development, pp. 5.1–5.9.

Gerber, H., 1996: Microphysics of marine stratocumulus clouds with two drizzle modes. *J. Atmos. Sci.*, **53**, 1649–1662.

Gerber, H., S. Chang and T. Holt, 1989: Evolution of a marine boundary layer jet. *J. Atmos. Sci.*, **46**, 1312–1326.

Gollmer, S. M., Harshvardhan, R. F. Cahalan and J. B. Snider, 1995: Windowed and wavelet analysis of marine stratocumulus cloud inhomogeneity. *J. Atmos. Sci.*, **52**, 3013–3030.

Hudson, J. G. and H. G. Li, 1995: Microphysical contrasts in Atlantic stratus. *J. Atmos. Sci*, **52**, 3031–3040.

IGPO, 1994: *Utility and feasibility of a cloud profiling radar.* Publ. 10, International GEWEX Project Office, 53 pp.

Illingworth, A. J. and N. I. Fox, 1997: The potential of a spaceborne cloud radar for detection of stratocumulus clouds. *J. Appl. Meteor.*, (in print).

Khalsa, S. J., 1993: Direct sampling of entrainment events in a marine stratocumulus layer. *J. Atmos. Sci*, **50**, 1734–1750.

Kikuchi, K., Y. Asuma, T. Taniguchi, M. Kanno, M. Tanaka, T. Hayasaka, T. Takeda and Y. Fujiyoshi, 1993: Structure and reflectence of winter maritime stratocumulus clouds. *J. Meteor. Soc. Japan*, **71**, 715–731.

Kikuchi, K., M. Fulii, R. Shirooka and S. Yoshida, 1991: The cloud base structure of stratocumulus clouds. *J. Meteor. Soc. Japan*, **69**, 701–708.

Kogan, Y. L., M. P. Khairoutdinov, D. K. Lilly, Z. N. Kogan and Q. F. Liu, 1995: Modeling of stratocumulus cloud layers in a large eddy simulation model with explicit microphysics. *J. Atmos. Sci*, **52**, 2923–2940.

Kropfli, R. A., S. Y. Matrosov, T. Uttal, B. W. Orr, A. S. Frisch, K. A. Clark, B. W. Bartram, R. F. Reinking, J. B. Snider and B. E. Martner, 1995: Cloud physics studies with 8 mm wavelength radar. *Atmos. Res.*, **35**, 299–313.

Kropfli, R. A. and B. W. Orr, 1993: Observations of microcells in the marine boundary layer with 8–mm wavelength Doppler radar. *26th Intern'l Conf. Radar Meteor.*, Norman, Oklahoma. Amer. Meteor. Soc., 492–494.

Krueger, S. K., G. T. Mclean and Q. Fu, 1995: Numerical simulation of the stratus–to–cumulus transition in the subtropical marine boundary layer .1. Boundary–layer structure. *J. Atmos. Sci*, **52** , 2839–2850.

Krueger, S. K., G. T. Mclean and Q. Fu, 1995: Numerical simulation of the stratus–to–cumulus transition in the subtropical marine boundary layer .2. Boundary–layer circulation. *J. Atmos. Sci*, **52**, 2851–2868.

Lee, J., J. Chou, R. C. Weger and R. M. Welch, 1994: Clustering, Randomness, and Regularity in Cloud Fields .4. Stratocumulus Cloud Fields. *J. Geophys. Res. – Atmos.*, **99**, 14461–14480.

Leon, D. C. and G. Vali, Retrieval of three–dimensional particle velocities from airborne Doppler radar data. *J. Atmos. Ocean. Techn.*, (in print).

Lhermitte, R., 1990: Attenuation and Scattering of Millimeter Wavelength Radiation by Clouds and Precipitation. *J. Atmos. Ocean. Techn.*, **7**, 464–479.

Lhermitte, R. M., 1988: Cloud and precipitation remote sensing at 94 GHz. *IEEE Trans. Geosci. Rem. Sens.*, **26**, 207–216.

Lhermitte, R. M., 1988: Observation of rain at vertical incidence with a 94 GHZ doppler radar: An insight on mie scattering. *Geophys. Res. Let.*, **15**, 1125–1128.

Liebe, H. J., T. Manabe and G. A. Hufford, 1989: Millimeter–wave attenuation and delay rates due fog/cloud conditions. *IEEE Trans. Antenn. Prop.*, **37**, 1617–1623.

MacVean, M. K., 1993: A numerical investigation of the criterion for cloud–top entrainment instability. *J. Atmos. Sci*, **50**, 2481–2495.

Mead, J. B., A. L. Pazmany, S. M. Sekelsky and R. E. McIntosh, 1994: Millimeter–wave radars for remotely sensing clouds and precipitation. *Proc. IEEE*, **82**, 1891–1906.

Miller, M. A. and B. A. Albrecht, 1995: Surface–based observations of mesoscale cumulus–stratocumulus interaction during ASTEX. *J. Atmos. Sci*, **52**, 2809–2826.

Moyer, K. A. and G. S. Young, 1991: Observations of vertical velocity skewness within the marine stratocumulus–topped boundary layer. *J. Atmos. Sci*, **48**, 403–410.

Nicholls, S., 1987: A model of drizzle growth in warm, turbulent, stratiform clouds. *Quart. J. Roy. Meteor. Soc*, **113**, 1141–1170.

Nicholls, S., 1989: The structure of radiatively driven convection in stratocumulus. *Quart. J. Roy. Meteorol. Soc.*, **115**, 487–511.

Nicholls, S. and J. Leighton, 1986: An observational study of the structure of stratiform cloud sheets. Part I: Structure. *Quart. J. Roy. Meteor. Soc.*, **112**, 431–460.

Paluch, I. R., C. A. Knight and L. J. Miller, 1996: Cloud liquid water and radar reflectivity of nonprecipitating cumulus clouds. *J. Atmos. Sci.*, **53**, 1587–1603.

Paluch, I. R. and D. H. Lenschow, 1991: Stratiform cloud formation in the marine boundary layer. *J. Atmos. Sci*, **48**, 2141–2158.

Pazmany, A. L., R. E. McIntosh, R. D. Kelly and G. Vali, 1994 b: An airborne 95 GHz dual–polarized radar for cloud studies. *IEEE Trans. Geosci. Rem. Sens.*, **32**, 731–739.

Pazmany, A., J. Mead, R. Mcintosh, M. Hervig, R. Kelly and G. Vali, 1994 a: 95–GHz polarimetric radar measurements of orographic cap clouds. *J. Atmos. Ocean. Techn.*, **11**, 140–153.

Rogers, D. P. and J. W. Telford, 1986: Metastable stratus tops. *Quart. J. Roy. Meteor. Soc.*, **112**, 481–500.

Sassen, K. and L. Liao, 1996: Estimation of cloud content by W–band radar. *J. Appl. Meteor.*, **35**, 932–938.

Vali, G., R. D. Kelly, A. Pazmany and R. E. Mcintosh, 1995: Airborne radar and in–situ observations of a shallow stratus with drizzle. *Atmos. Res.*, **38**, 361–380.

Wang, Q. and B. A. Albrecht, 1994: Observations of cloud–top entrainment in marine stratocumulus clouds. *J. Atmos. Sci*, **51**, 1530–1547.

Welch, R. M., K. S. Kuo, B. A. Wielicki, S. K. Sengupta and L. Parker, 1988: Marine stratocumulus cloud fields off the coast of Southern California observed using LANDSAT imagery. Part I: Structural characteristics. *J. Appl. Meteorol.,* **27,** 341–362.

Welch, R. M., S. K. Sengupta and K. S. and Kuo, 1988: Marine stratocumulus cloud fields off the coast of Southern California observed using LANDSAT imagery. Part II: Textural analysis. *J. Appl. Meteorol.,* **27,** 363–378.

White, A. B., C. W. Fairall, A. S. Frisch, B. W. Orr and J. B. Snider, 1996: Recent radar measurements of turbulence and microphysical parameters in marine boundary layer clouds. *Atmos. Res.,* **40,** 177–221.

Figure Captions.

Fig. 1. Satellite images (visible channel) of area along coasts of southern Washington, Oregon, and northern California for the three study periods. Images are from GOES–7 for 950914 and 950915, and form NOAA–14 for 950916. Areas covered by aircraft flights are outlined with boxes.

Fig. 2a. Vertical profiles of temperature (T, °C), total specific humidity (q_t, g kg^{-1}), equivalent potential temperature (θ_E, K), potential temperature (θ, K), wind direction (*wdir*, °true) and wind speed (*wmag*, m s^{-1}) for 950914. The data include approach and departure soundings into and out of the study area and all data from within the study area. Data are plotted as averages over 25–m height intervals. Heavy lines in the temperature panels indicate the vertical extents of the clouds.

Fig. 2b. Same as Fig. 2a but for 950915.

Fig. 2c. Same as Fig. 2a but for 950916.

Fig. 3 Detailed data for temperature (T, °C), specific humidity (q, g kg^{-1}), and equivalent potential temperature (θ_E, K) from a series of ascents and descents through the cloud on 950914. Each point represents 1 s of data. Cloud depth is indicated by the heavy vertical line in the first panel. Points within the main cloud layer (330 to 550 m) lie along slightly different, but constant, θ_E lines in all but one of the sequences.

Fig. 4. Examples of vertical cross–sections of radar reflectivity (Z) and of Doppler velocity (V, m s^{-1}, positive upward) for the three days discussed in the text.

Fig. 5. Horizontal cross–sections of radar reflectivity (Z) obtained with the radar in the side–looking position. Altitudes are indicated above each image. Orientation with respect to North is preserved for images from different altitudes for given days.

Fig. 6. Contributions to total reflectivity by two size ranges of hydrometeors. Reflectivity (Z_{calc})$_{fssp}$, calculated from the drop size distributions measured by the FSSP probe (< 45 µm diameter), is shown by a dotted line and $(Z_{calc})_{twodc}$, from the 2D–C probe (> 50 µm), by a dashed line. These data combine measurements made during several ascents and descents through each cloud.

Fig. 7a. Vertical profiles of radar reflectivity (Z), Doppler velocity (V, positive–up), and the $Z–V$ correlation coefficient, for the up–looking radar data shown for 950914 in Fig. 4. In the Z and V profiles, the heavy solid lines show the mean values while the other lines show ± one standard deviation from the means (triple dots), the 50% ranges (dotted) and the 90% ranges (thin).

Fig. 7b. – same as Fig. 7a, but for the image shown for 950915 in Fig. 4.

Fig. 7c. – same as Fig. 7a, but for the image shown for 950916 in Fig. 4.

Fig. 8. Vertical air velocity from the in situ probes versus the radar reflectivity 60 m to the side of the aircraft for the data shown in the higher altitude images of Fig. 5. The upper panels show individual data points, each point representing 3.4 m of flight path. In the lower panel, horizontal lines show the correlation coefficients for the entire data segments and different symbols indicate the coefficients over 1/2, 1/4 and 1/8th of the segments (the symbols are placed at the mid–points of the intervals).

Fig. 9. Correlation coefficients between the aircraft–measured vertical wind (w) and the radar reflectivity $(Z_{calc})_{twodc}$ calculated from drop size distributions measured by the 2D–C probe as

functions of altitude. Values indicated by diamonds are based on 1–Hz data from the ascent and descent soundings with roughly 70, 40 and 30 points per height interval for the three days. Additional data from continuous level flight segments of 4–6 km length (50–70 seconds of data) are indicated by circles. Thick vertical lines indicate the altitude of the cloud layer for each case.

Fig. 10. The same vertical cross–sections of radar reflectivity (Z) and Doppler velocity (V) as those shown in Fig. 4, but with Z and V contour levels changed to highlight areas having relatively low reflectivities and large negative (downward) velocities.

Fig. 11a. Traces of aircraft–measured vertical winds (w), temperature (T), LWC, droplet concentration and calculated reflectivity for an ascent through cloud top at on 950914. The numbers above the top panel are aircraft altitudes. The LWC was derived from the CSIRO probe. Droplet concentration and reflectivity are based on FSSP data.

Fig. 11b. Same as Fig. 11a, except for a gradual descent into cloud on 950915. The LWC content in this figure is based on FSSP data. Aircraft altitudes are indicated at the bottom of the top panel.

Fig. 12. Correlation coefficients for vertical air velocity versus mass of drizzle drops (>50 μm diameter) at different altitudes based on data collected with 90–m resolution during a series of ascents and descents through the cloud layer on 950916. The depth of the cloud layer is indicated by a heavy vertical line.

Fig. 13. Profiles of LWC calculated from drop–size distributions measured by the FSSP probe. Data for each day are combined from several soundings. Mean values are indicated by asterisks, the thick bars encompass the 50th percentiles, and the thin bars show the range of values to the 90th percentiles. Broken lines show LWC values that would occur for adiabatic ascents of saturated parcels.

Fig. 14. Profiles of "dispersion" values for LWC for 950914 and 950915, plotted as functions of normalized cloud depth (ϕ). The first panel shows dispersions calculated as the 50–percentile range of LWC values divided by the means at each level; the second panel uses the 90–percentiles. Each panel contains data from the FSSP (asterisks for 950914; diamonds for 950915) and the CSIRO probe (solid line for 950914 only).

Fig. 15. Profiles of droplet concentrations for 950914 (asterisks) and for 950915 ("+"), plotted as functions of normalized cloud depth (ϕ). The diamonds show average concentrations from horizontal aircraft passes on 950915.

Fig. 16. Average drop size distributions (FSSP and 2D–C data) for horizontal passes at different levels on 950914 and 950915. The labels indicate the geometric height above sea surface (m msl) and the corresponding normalized cloud depth level (ϕ).

Fig. 17. Drop size distributions as functions of altitude on 950914 and 950915. From right to left, alternating heavy and thin lines indicate the differential concentrations for each of the 15 size bins used for the FSSP data (3 to 45 μm in 3–μm intervals) and for 5 size bins extracted from the 2D–C data (50–100 μm, 100–150 μm, etc.). In each panel, the dashed lines are the first and second FSSP size bins, respectively.

Fig. 18a. Profiles of variance and skewness for aircraft–measured vertical winds (w, asterisks and diamonds) and radar Doppler velocities (V, + signs) on 950914. Diamonds refer to vertical wind data from horizontal aircraft passes, while asterisks refer to data from ascents and descent soundings. The Doppler velocities are from a data segment of approximately 5 km length.

Fig. 18b. – as Fig. 18a, but for 950915.

Fig. 18c. – as Fig. 18a, but for 950916.

Fig. 19. The relationship between droplet concentration and vertical air velocity during level flight segments within clouds. Each point in the upper panels is a sample from approximately 10 m horizontal distance. The histograms in the lower panels show the droplet concentrations associated with air velocities differing from the means by more than 0.5 standard deviation.

Fig. 20. Spectral and cospectral densities for radar reflectivity (Z) and Doppler velocity (V) as functions of altitude on 950914 and 950916. Data are from 5 to 20–km segments of up–looking radar data. In the first two panels the contour values are base–10 logarithms of spectral density; in the third panel the contour values are actual cospectral densities. The red–to–violet color progression corresponds to a numerical progression from positive to negative.

950916 21Z
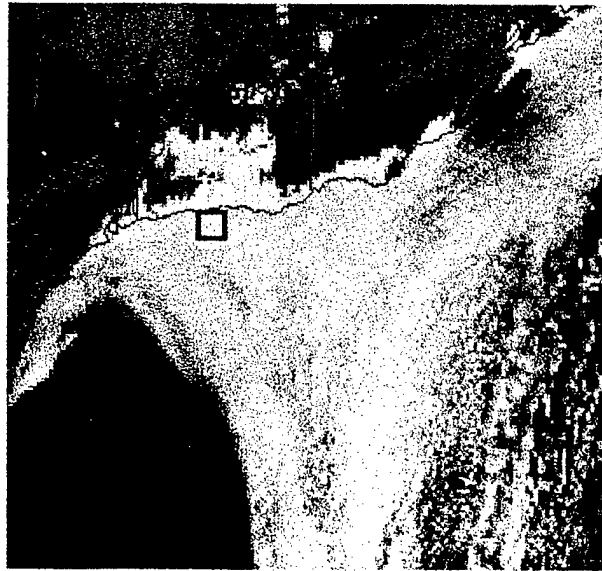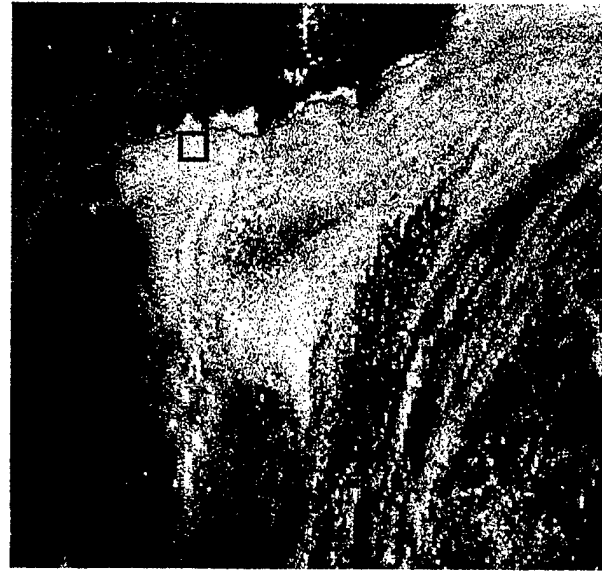
950915 19Z

950914 20Z

Fig. 1

Fig. 2a

950914

Sun Jan 11 15:14:43 1998

Fig. 2.b.

Fig 2.c.

950916

Sun Jan 11 17:30:23 1998

Fig. 3.

Fig. 4

Fig. 5

950916   950915   950914

reflectivity (dBZ)

altitude (m)

Fig. 6.

Fig. 7a.

950914

Fig. 7b.

950915

altitude (m)

reflectivity (dBZ)

velocity (m s^{-1})

cross-correl.

950916

reflectivity (dBZ)

velocity (m s^{-1})

cross−correl.

altitude (m)

Fig. 7c.

Fig. 8.

Fig. 9.

w vs. $(Z_{calc})_{twodc}$ correlation coefficient

altitude (m)

950914   950915   950916

Sun Jan 11 19:48:03 1998
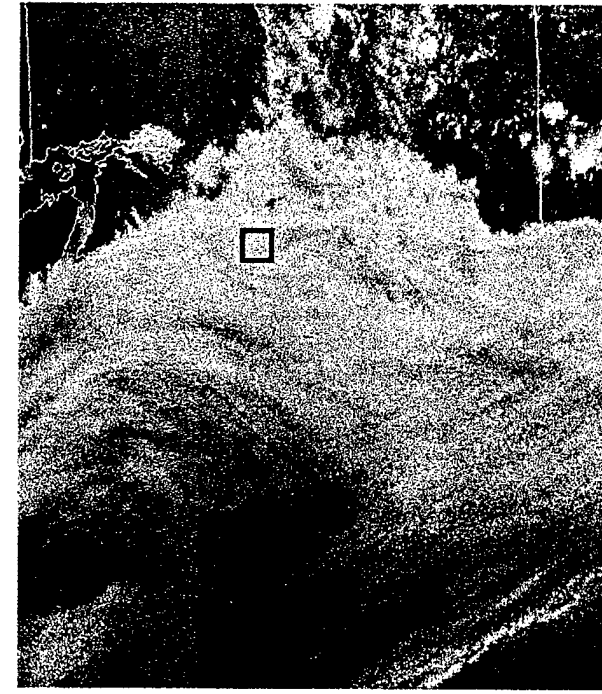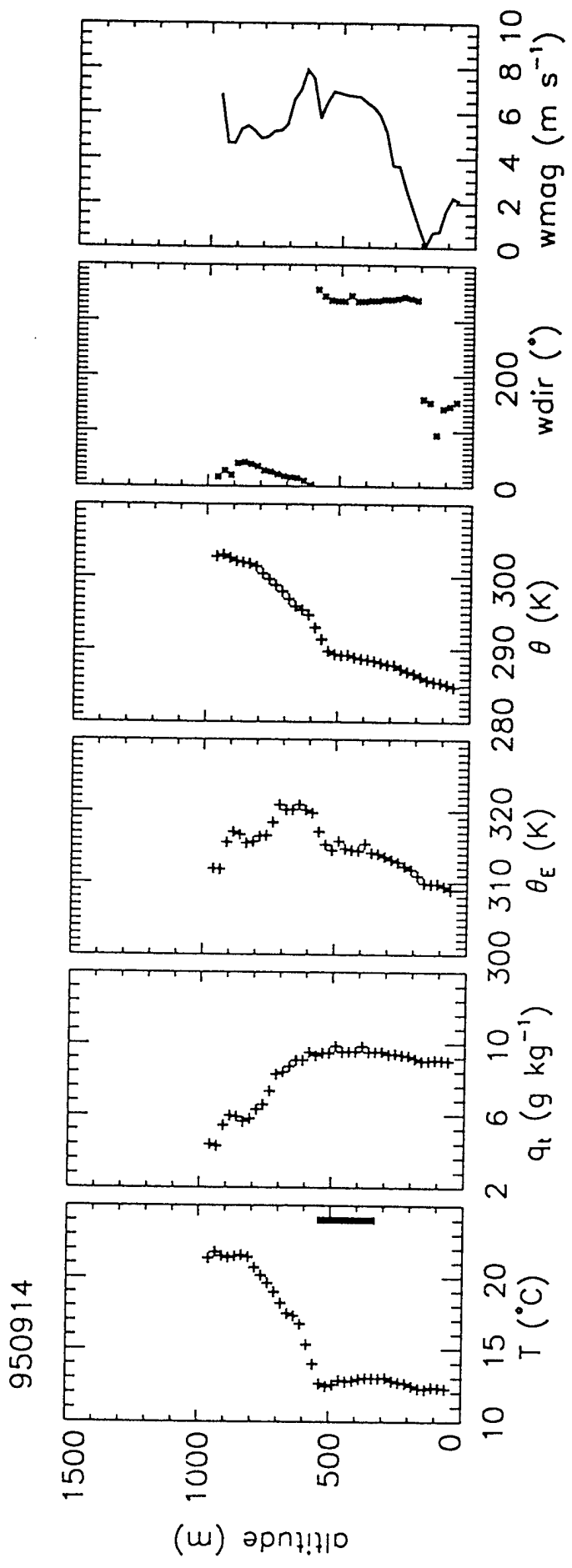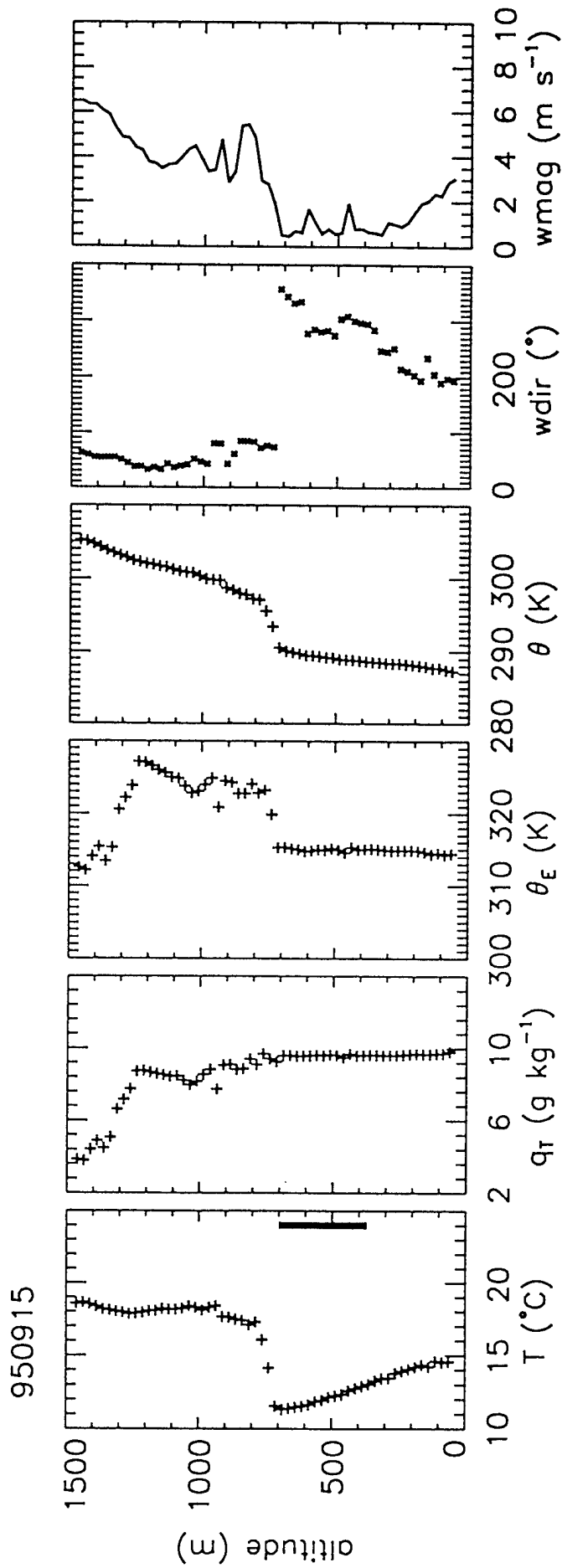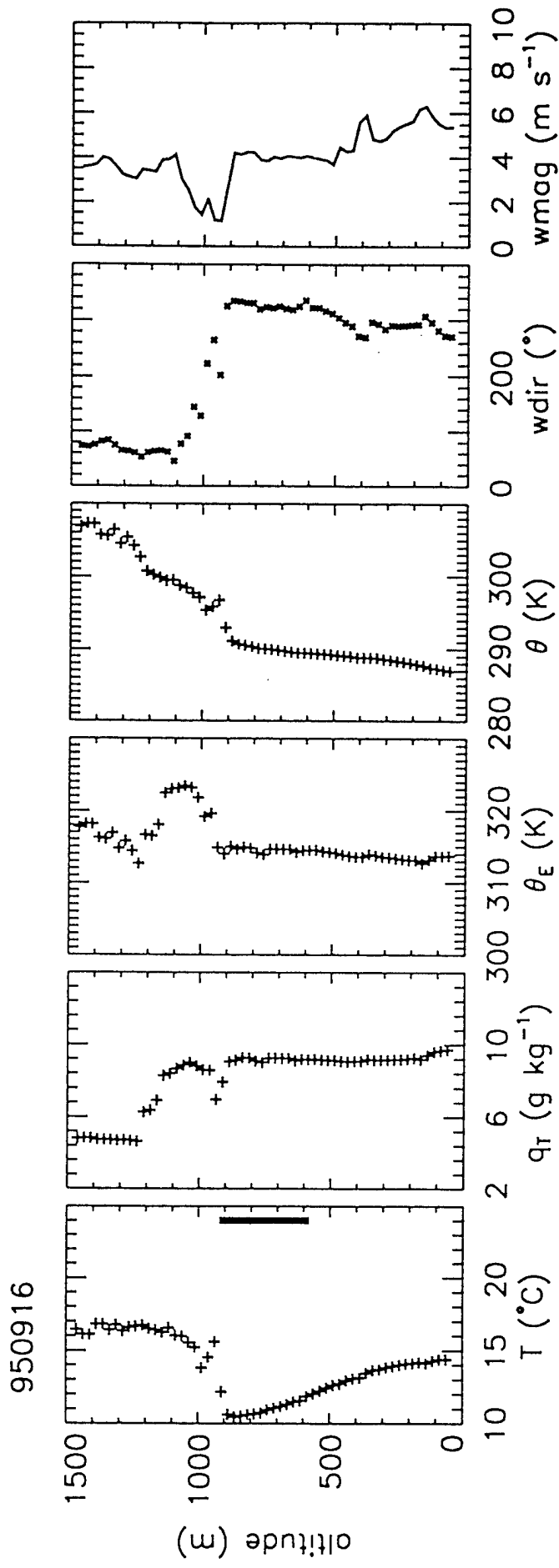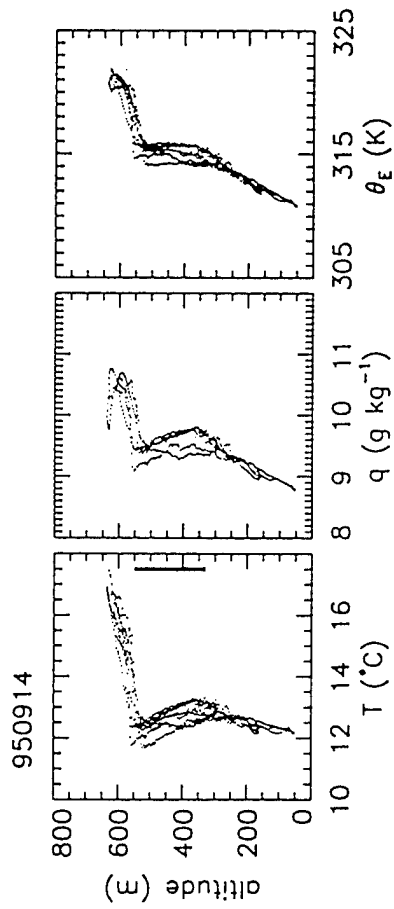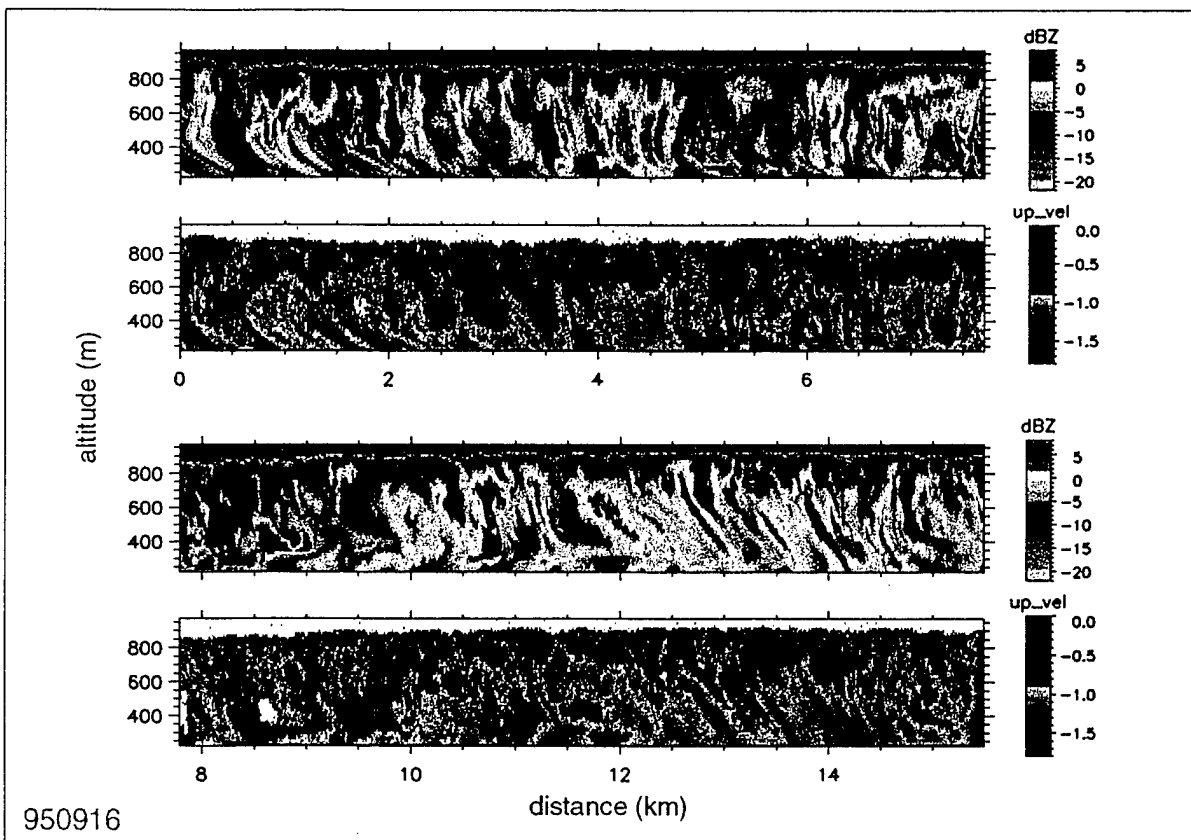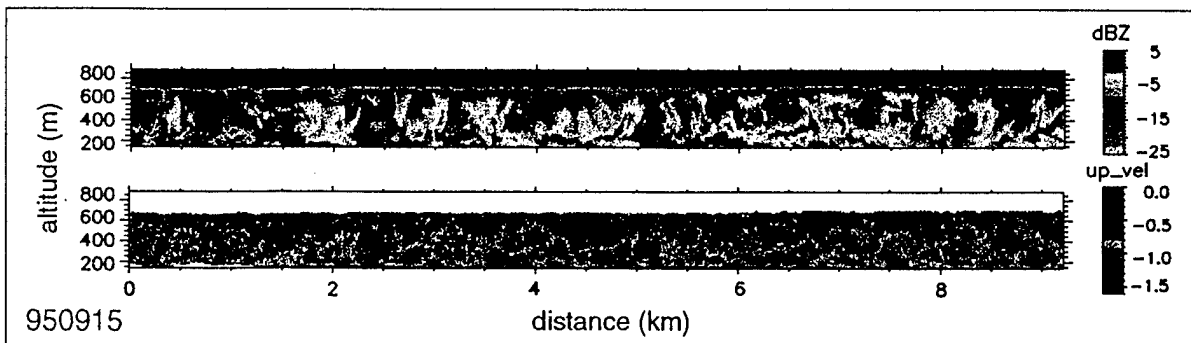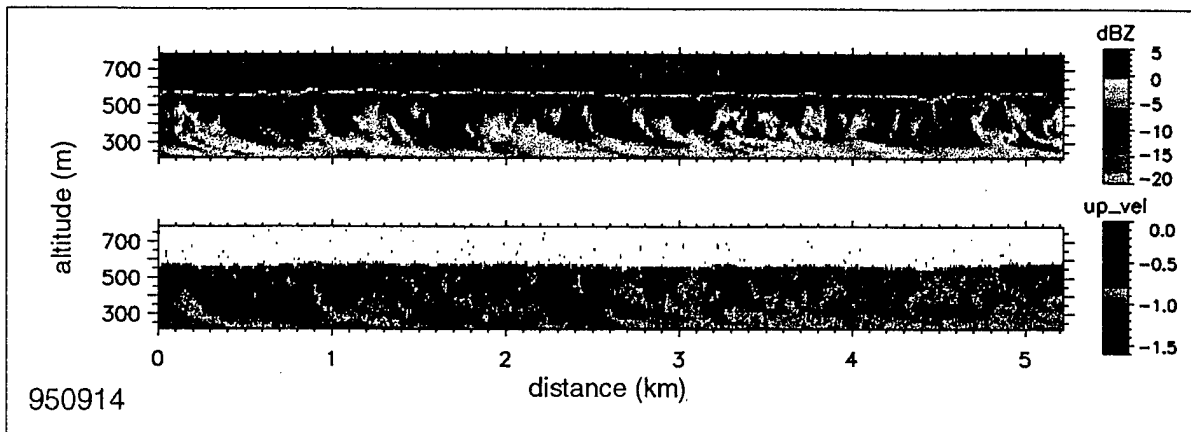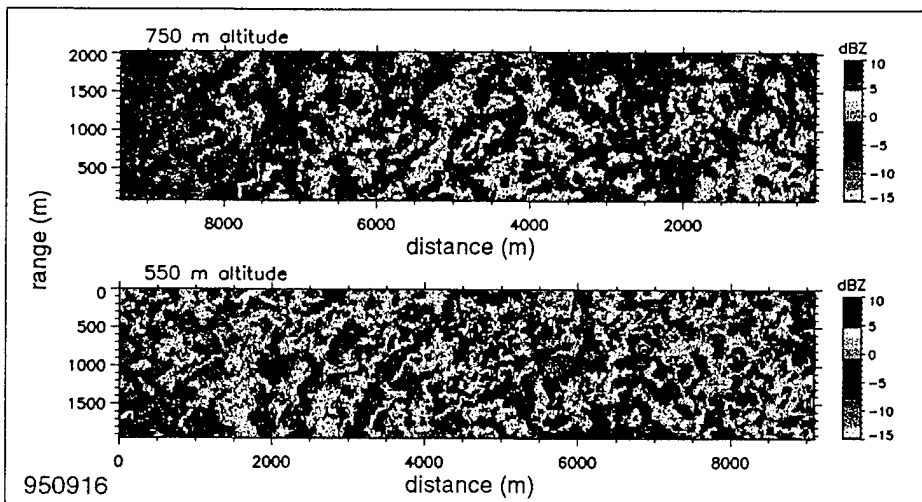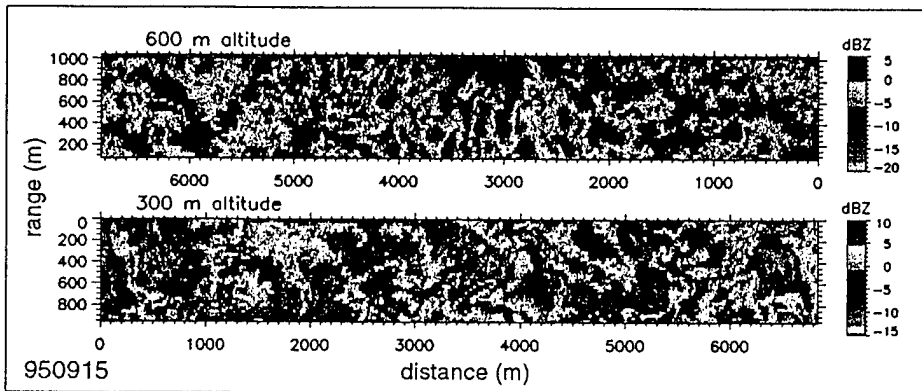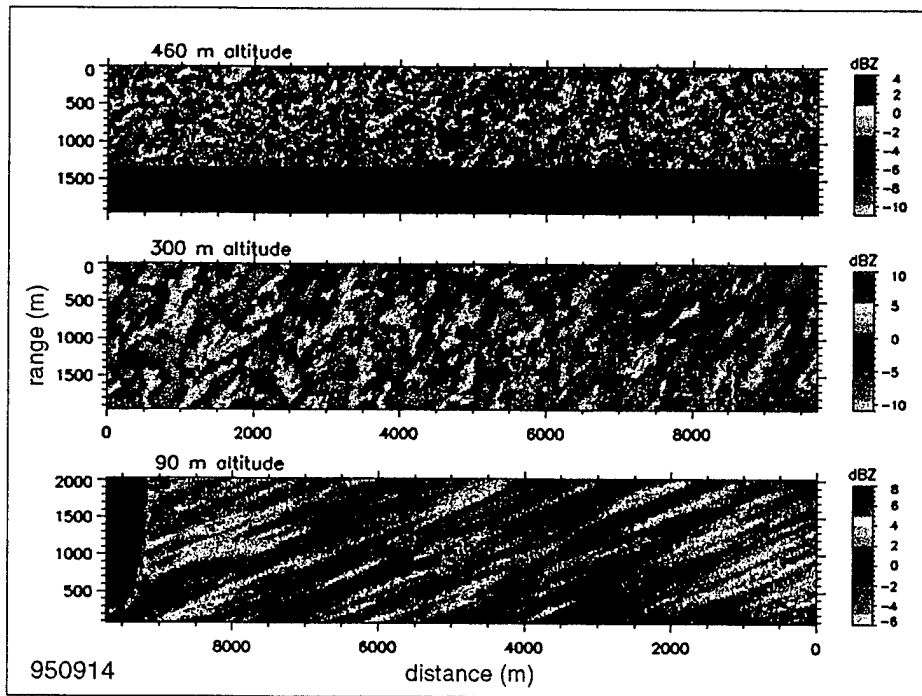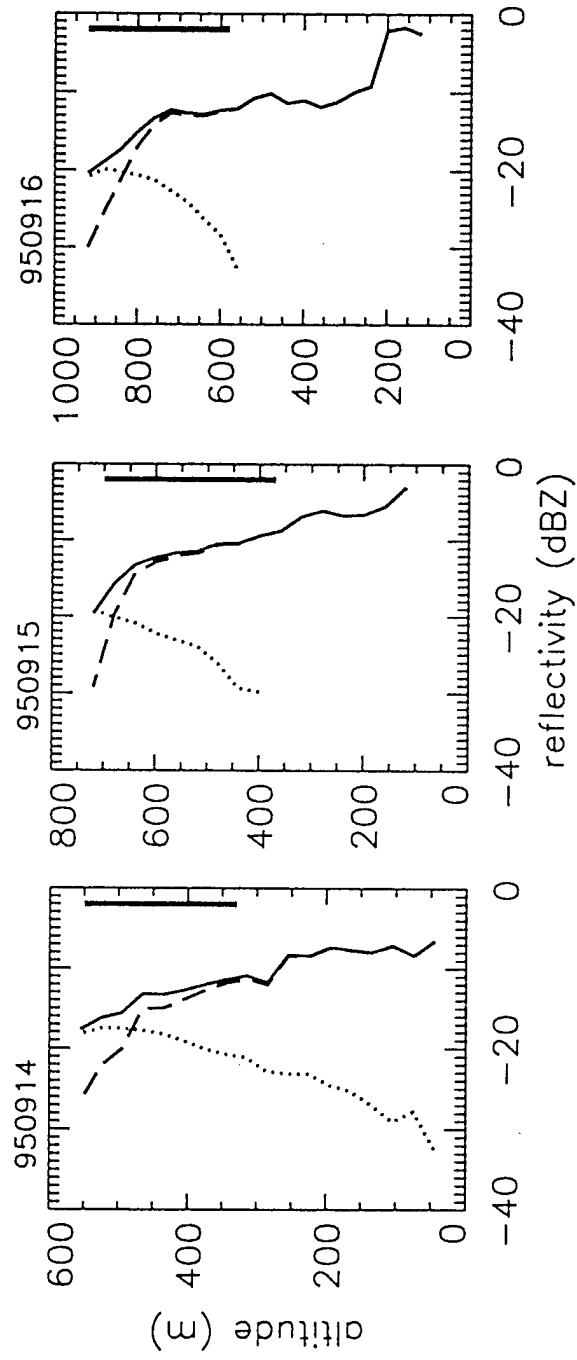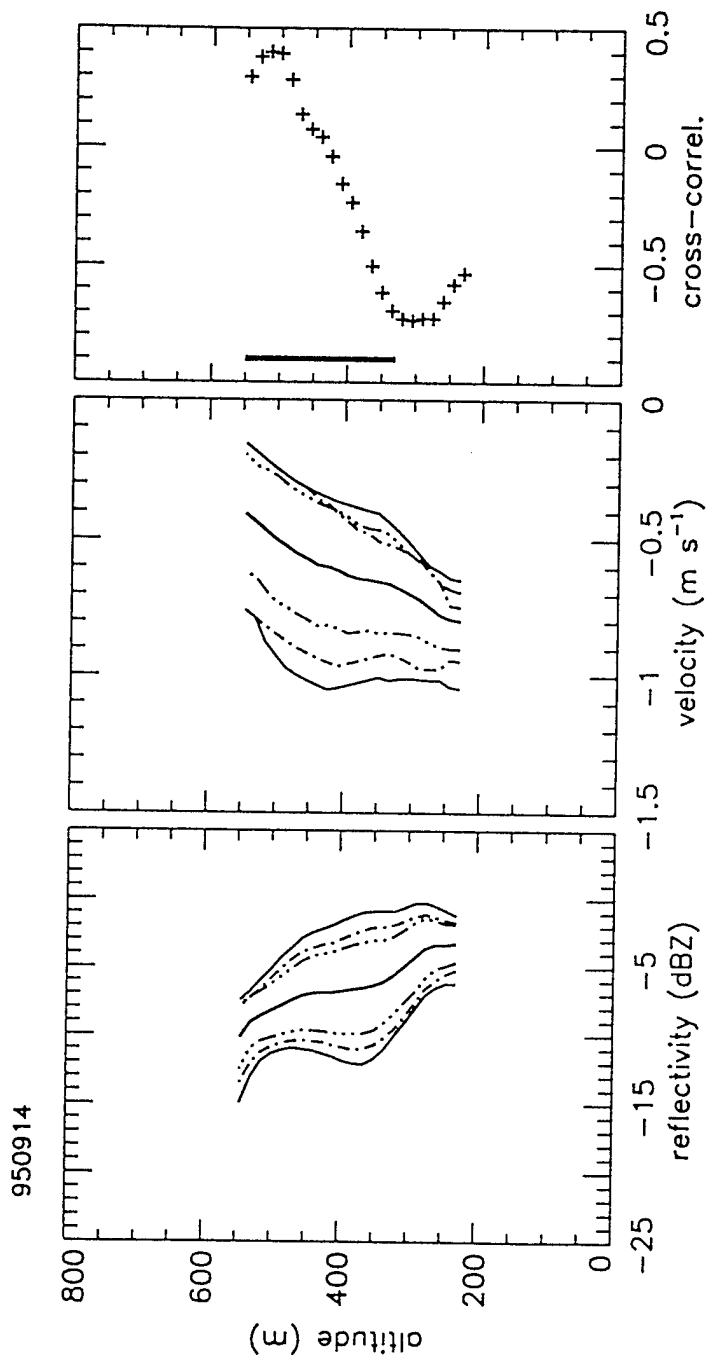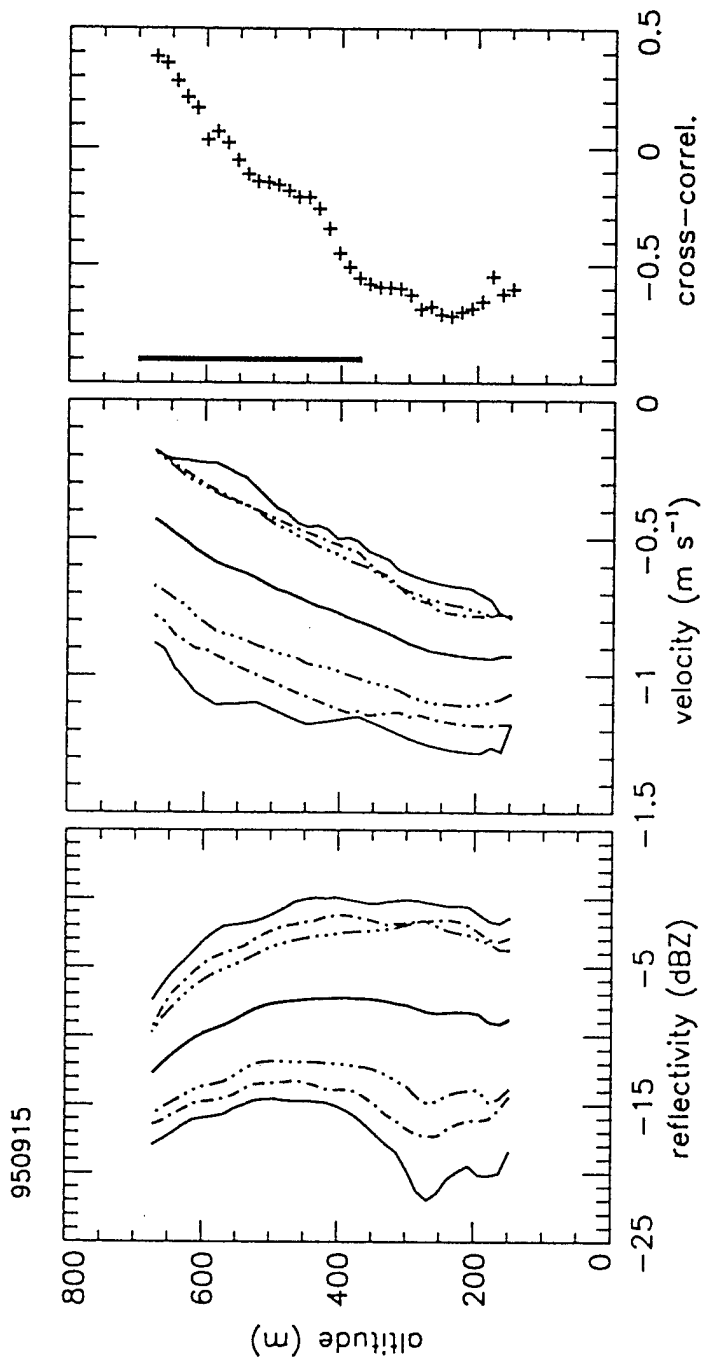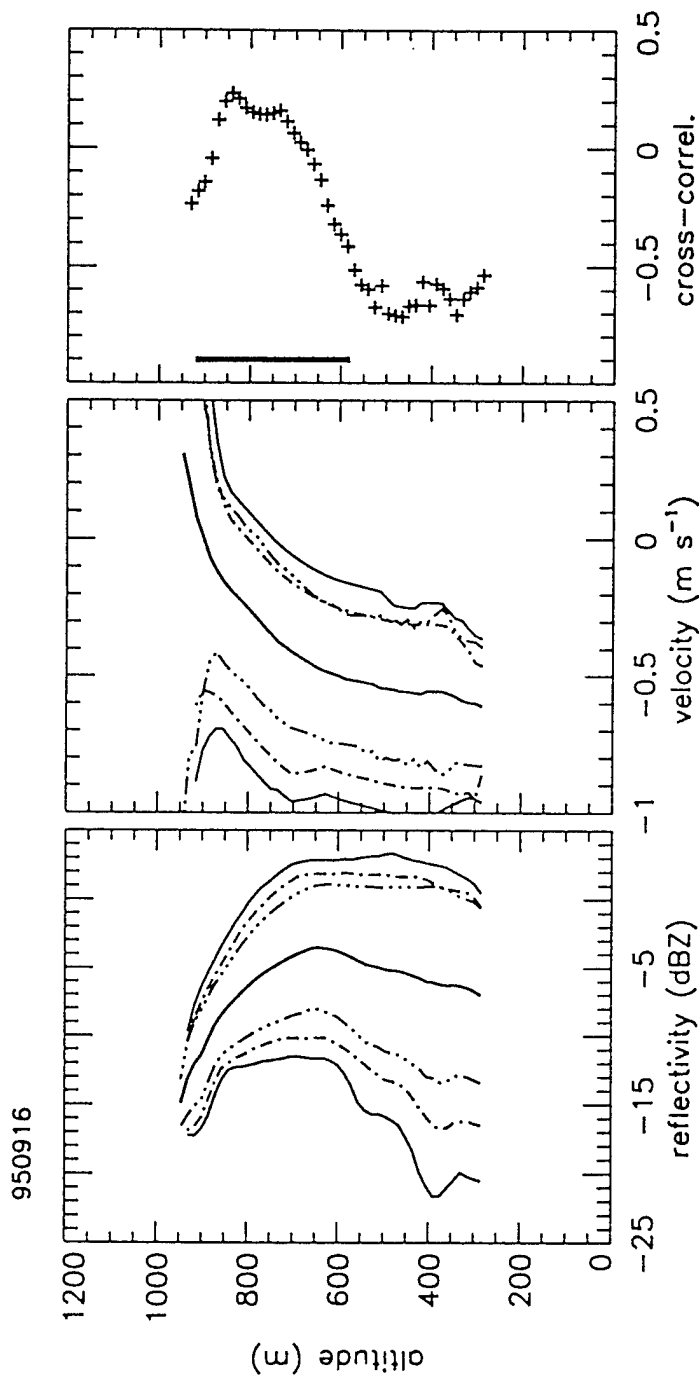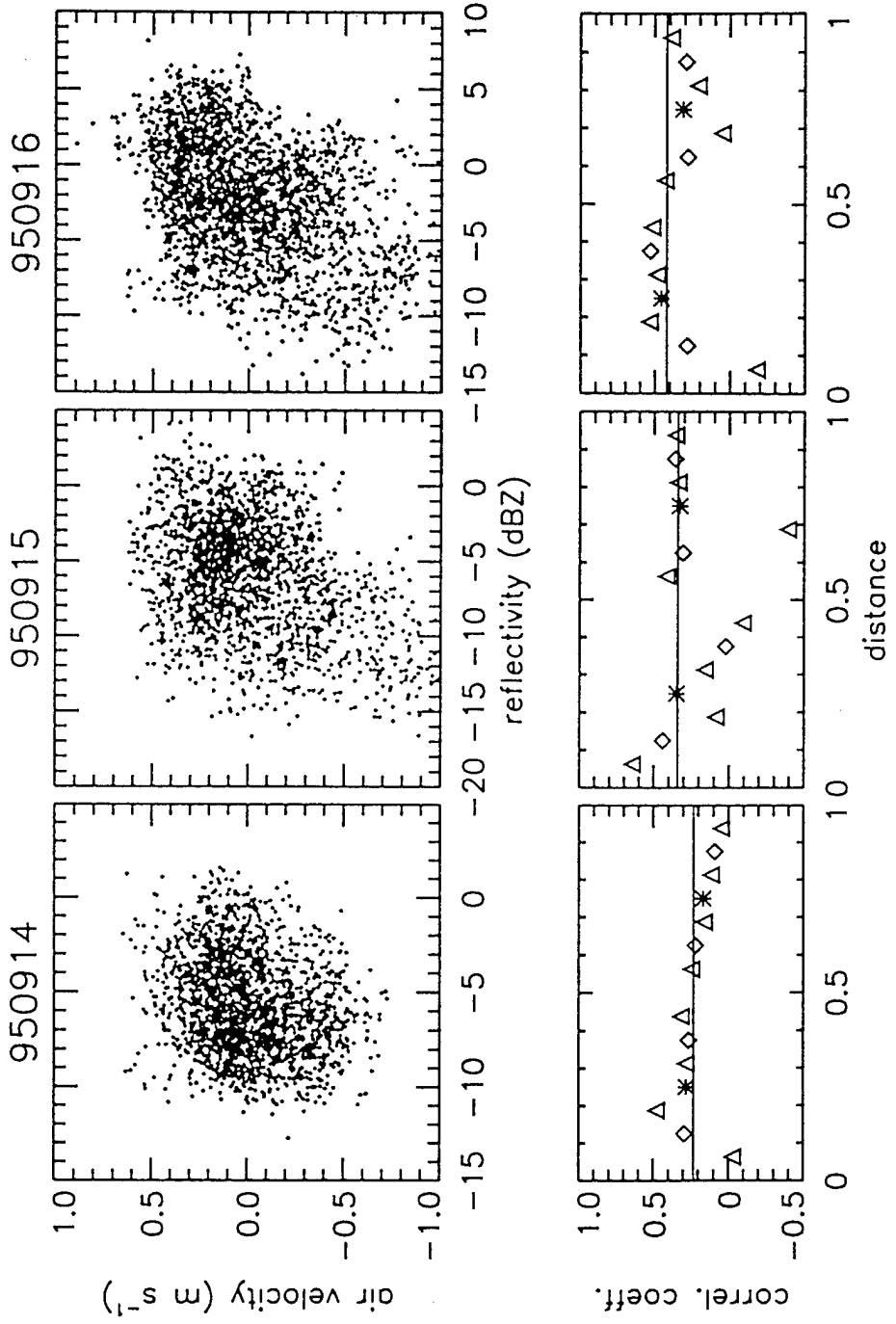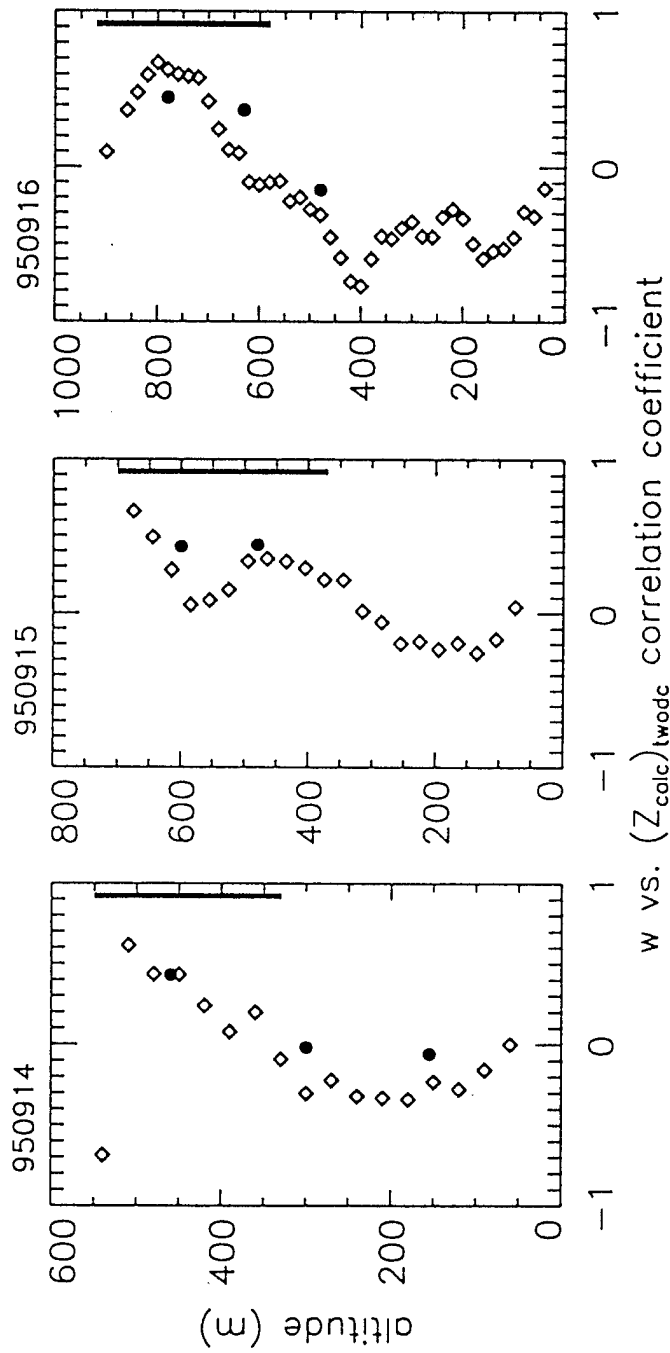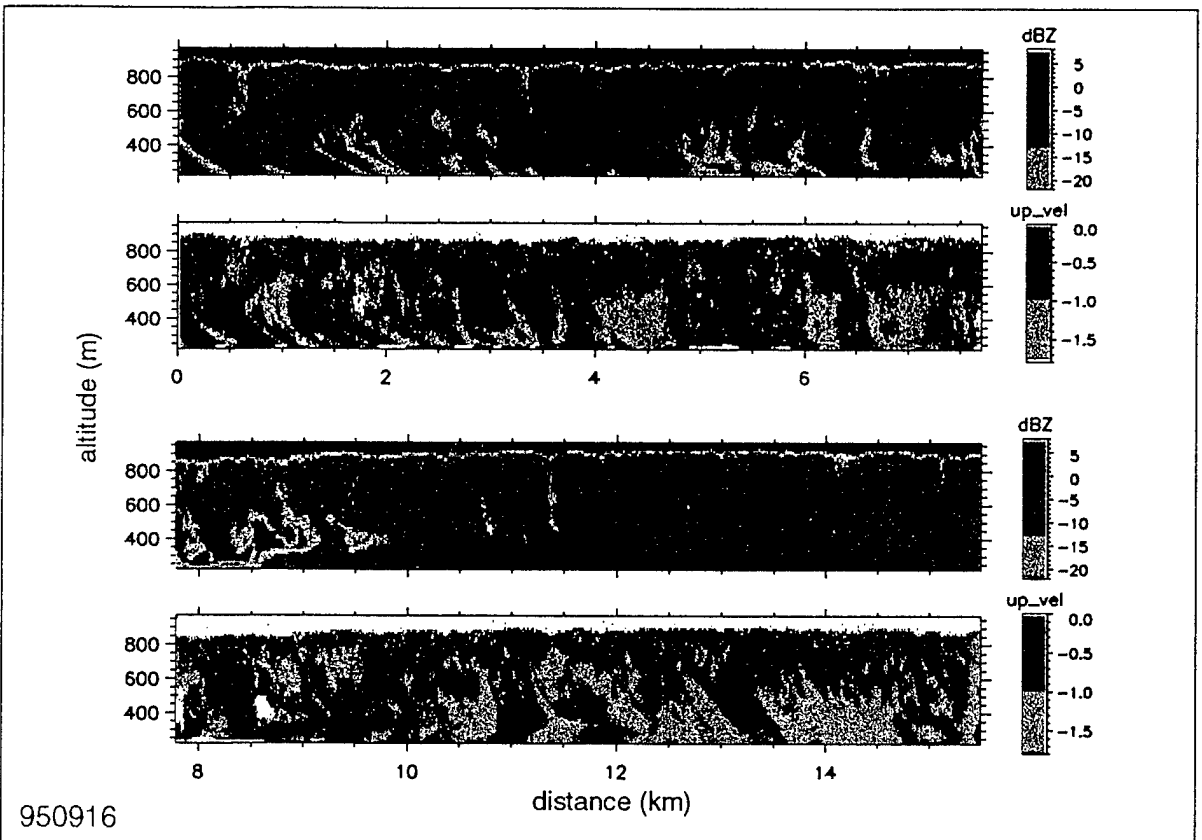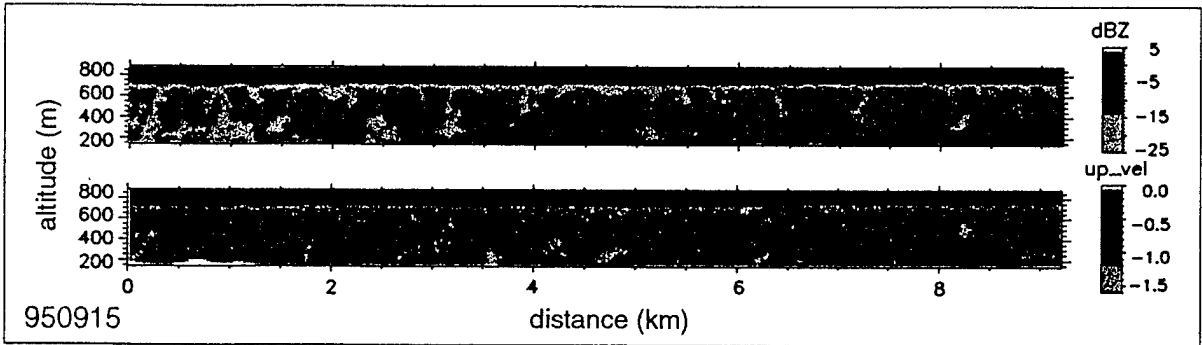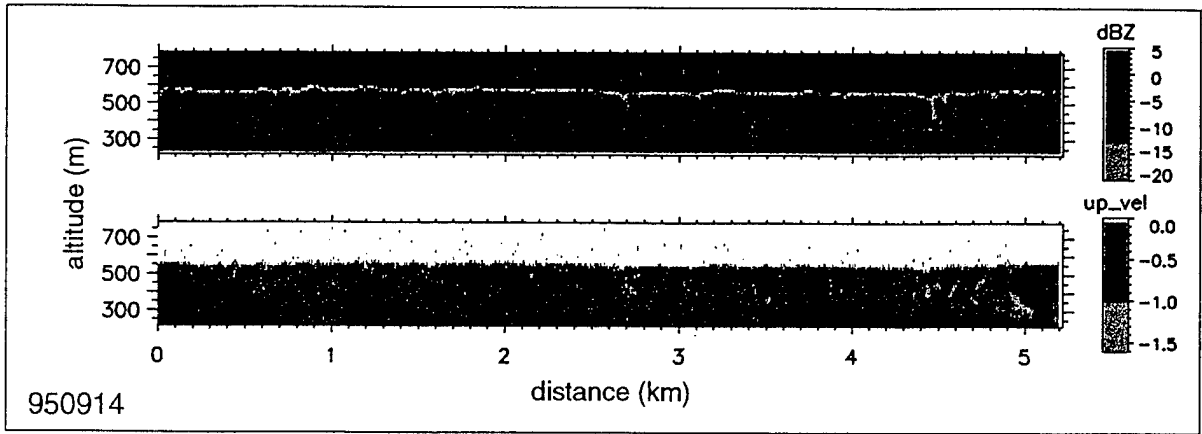
Fig. 10
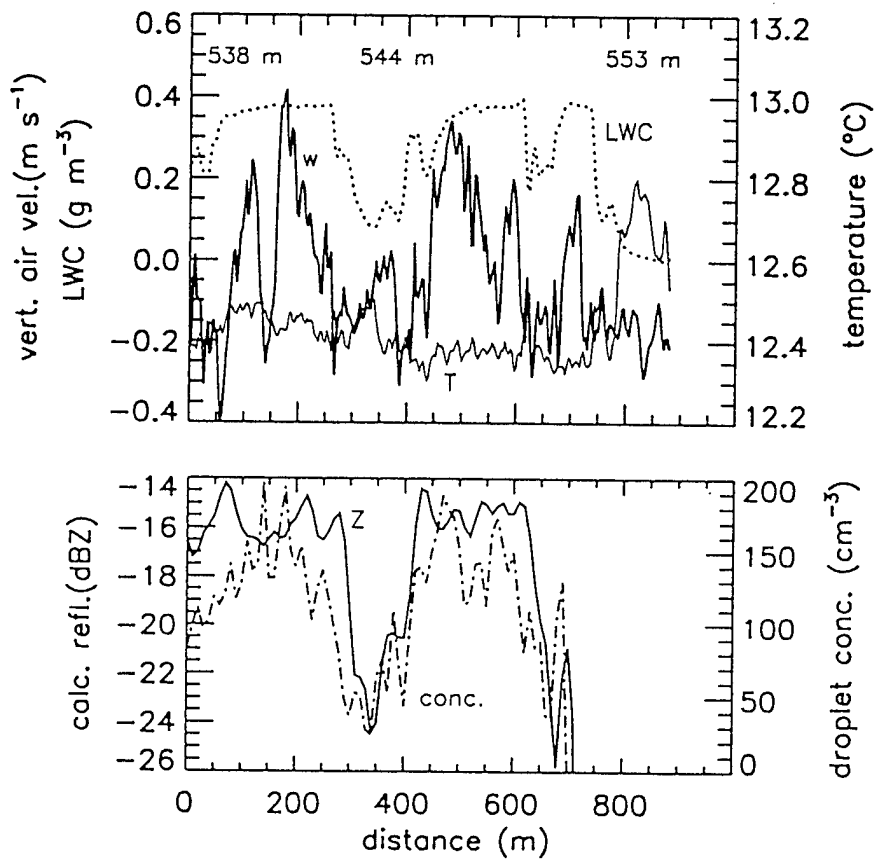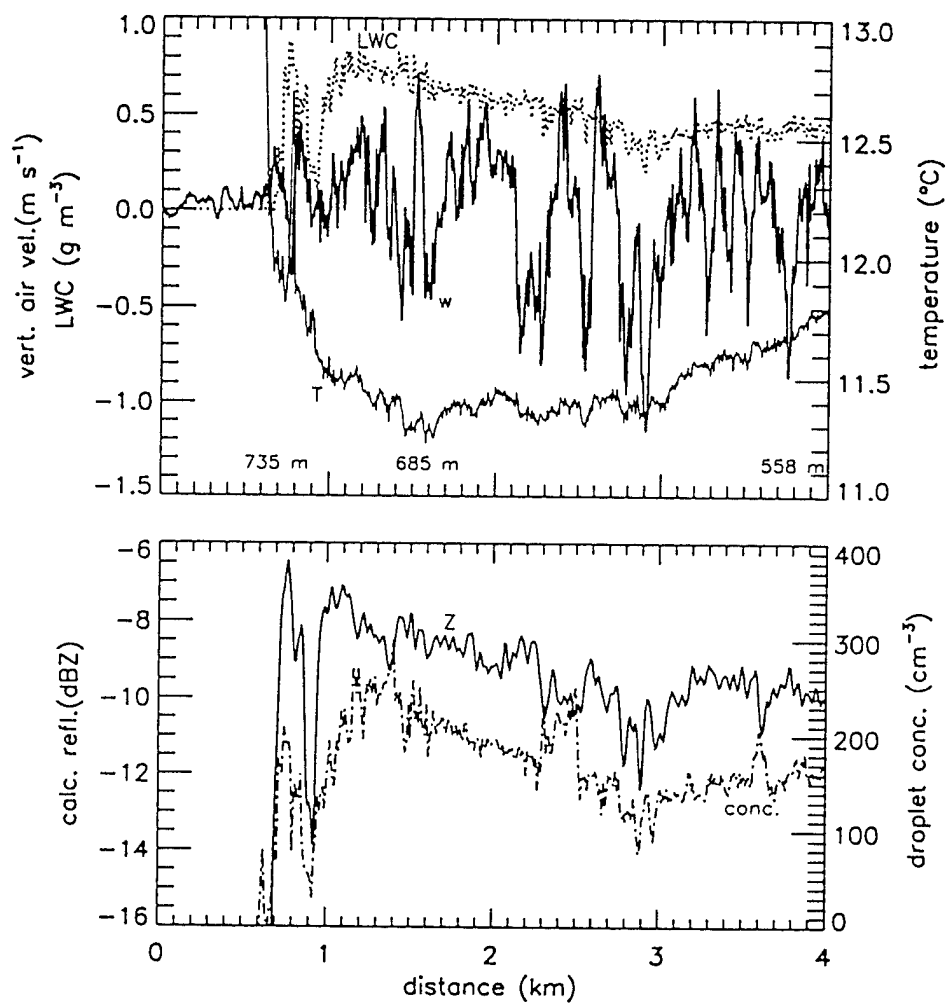
Fig. 11 a.

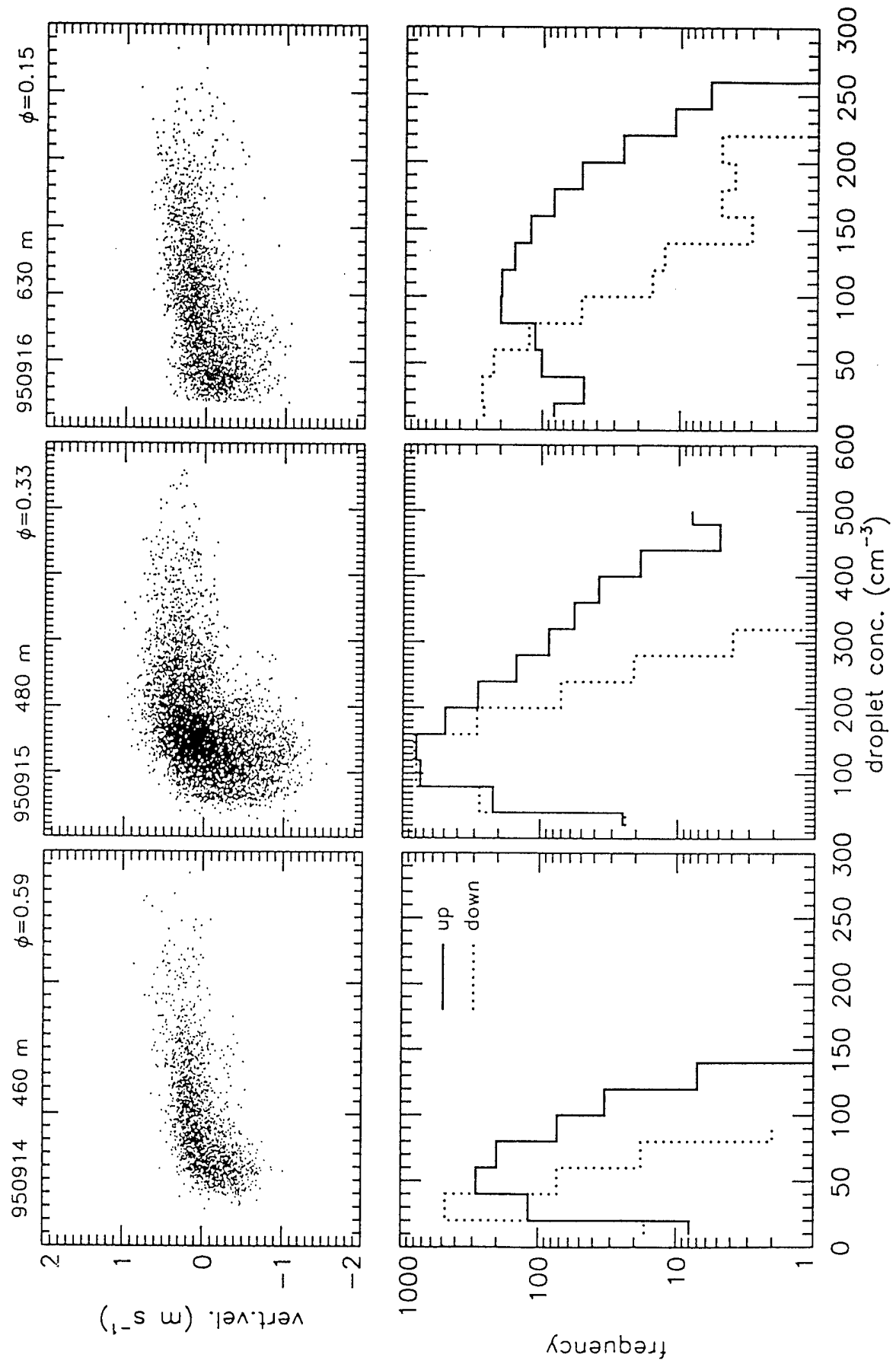Fig. 11 b.
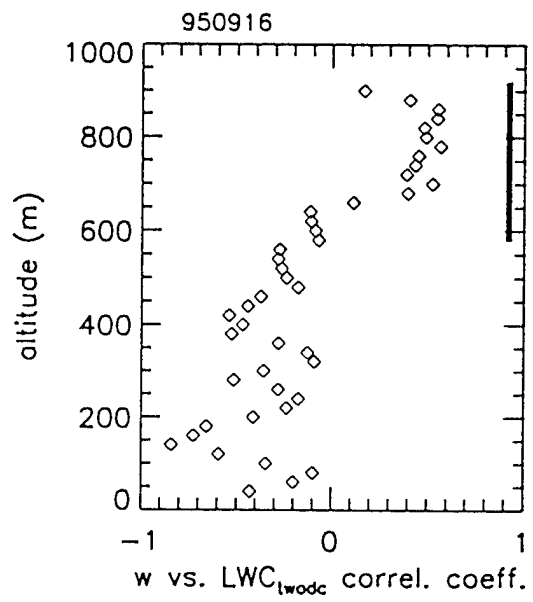
Fig. 12
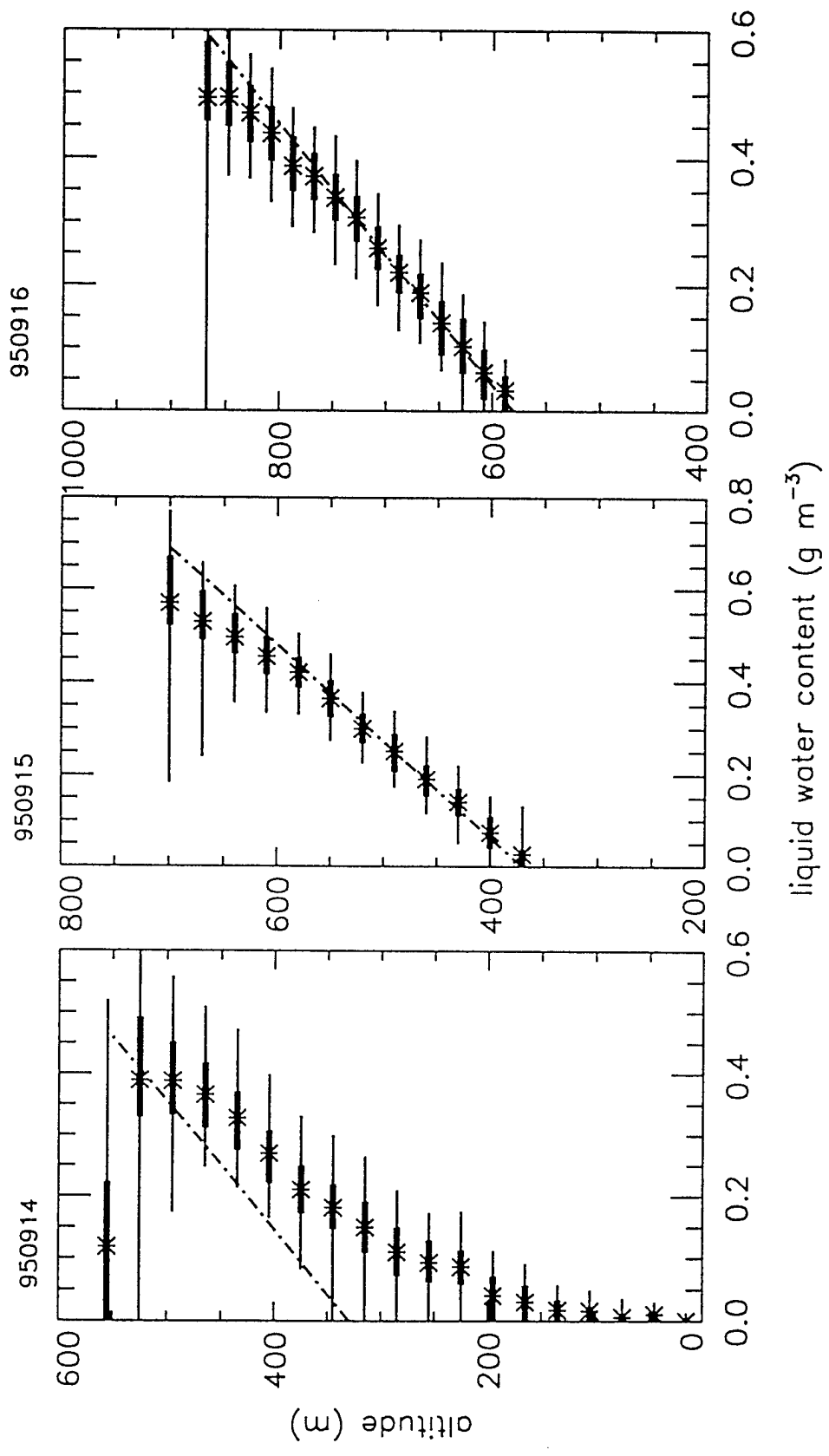
Fig. 13.
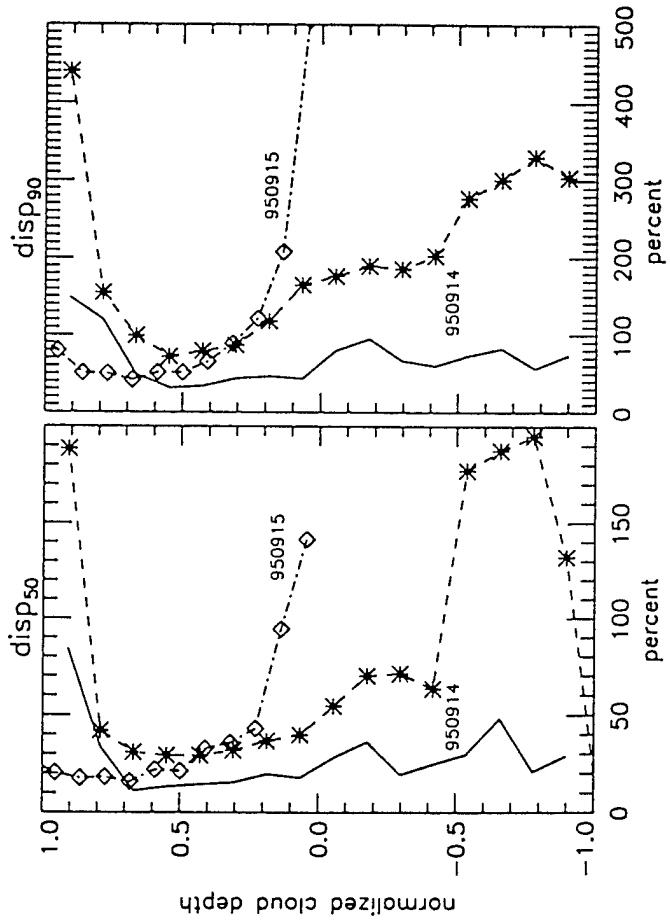
Fig. 14
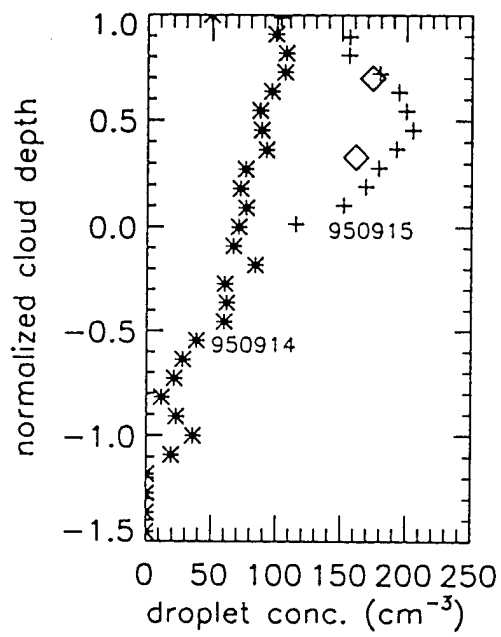
Fig. 15.
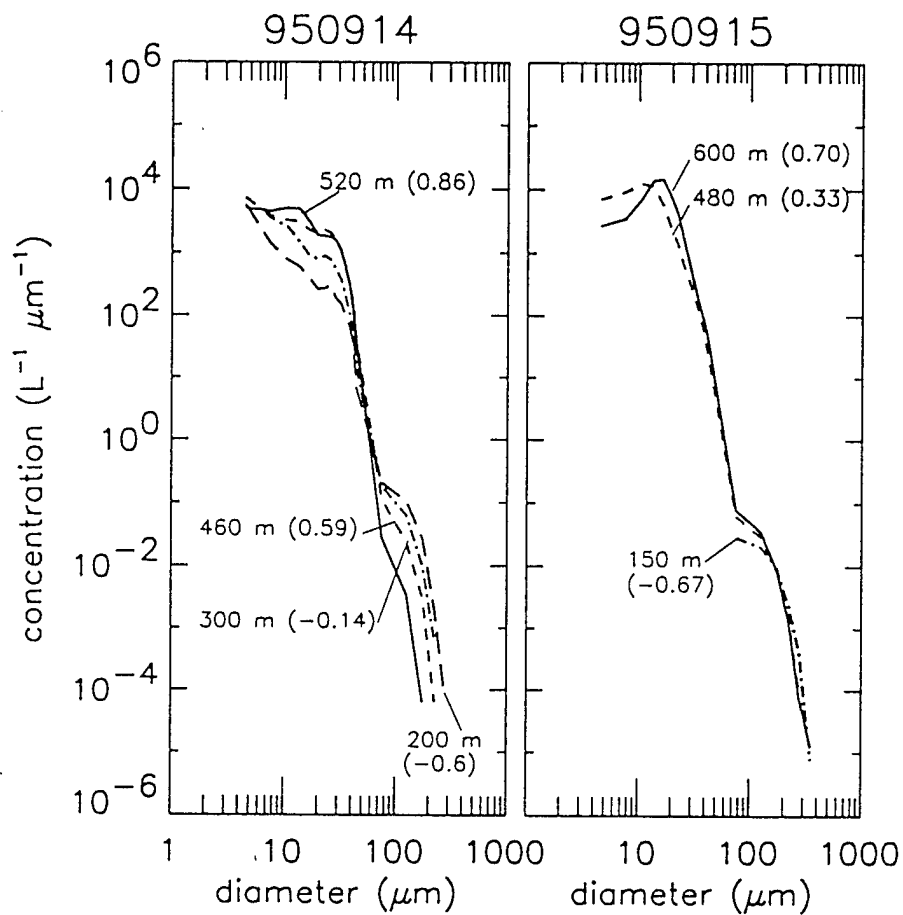
Fig. 16.

Fig. 17

Fig. 18a

Fig. 18 A

Fig. 18C

Fig. 19

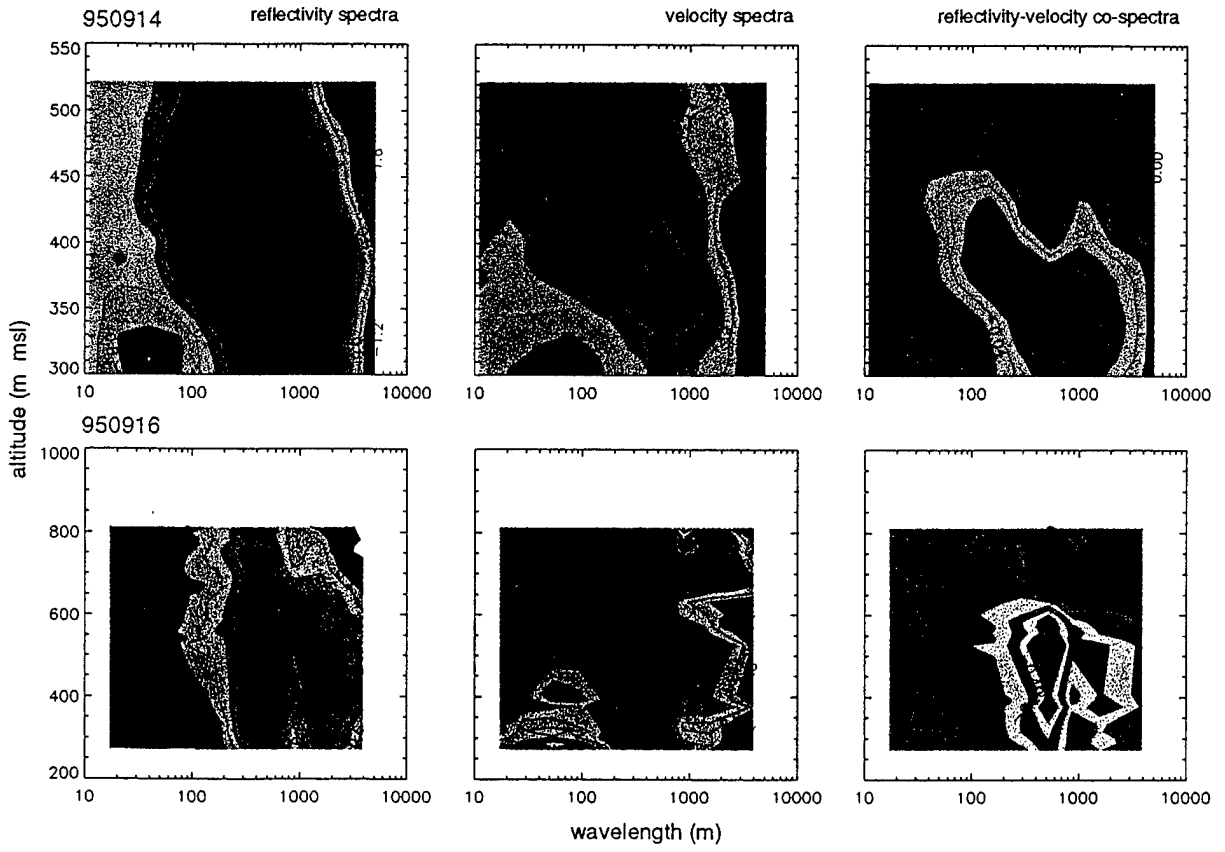950914   reflectivity spectra   velocity spectra   reflectivity-velocity co-spectra

950916

altitude (m msl)

wavelength (m)
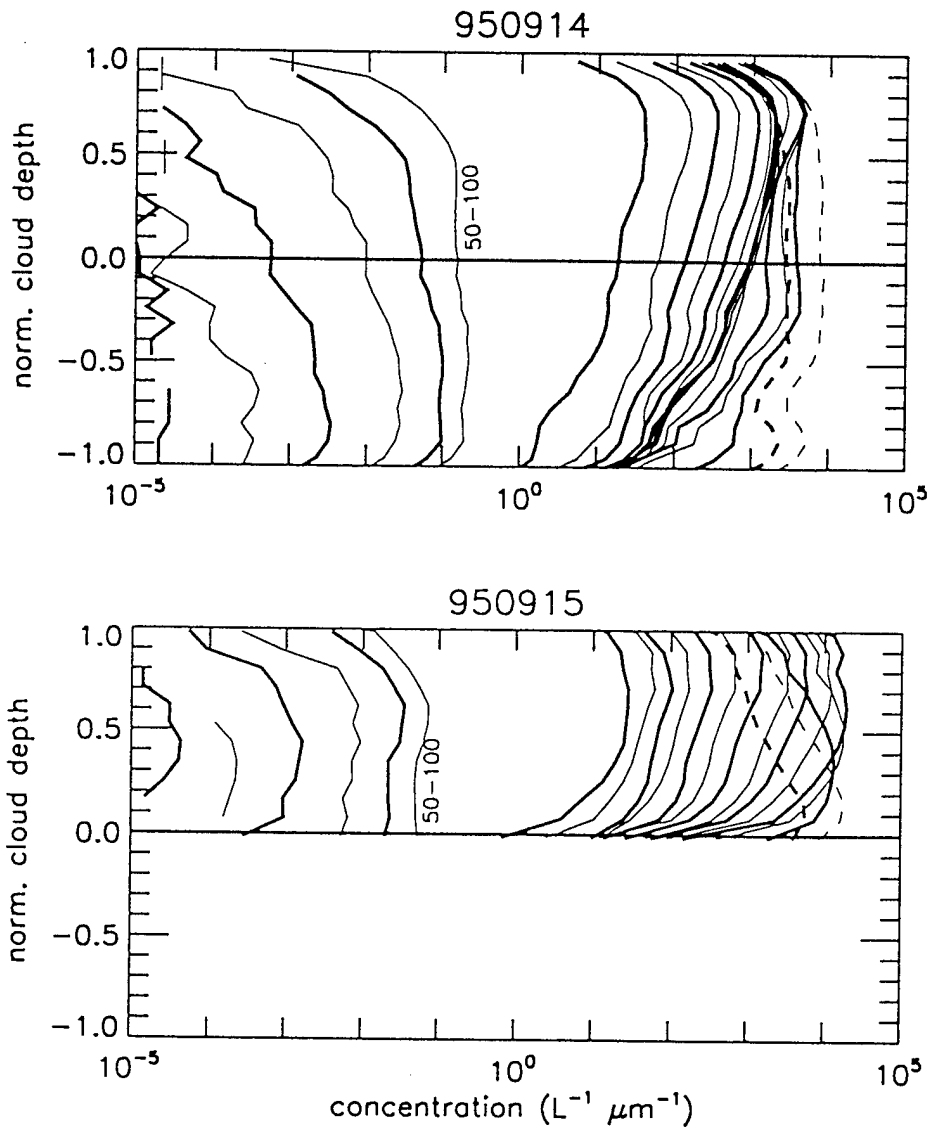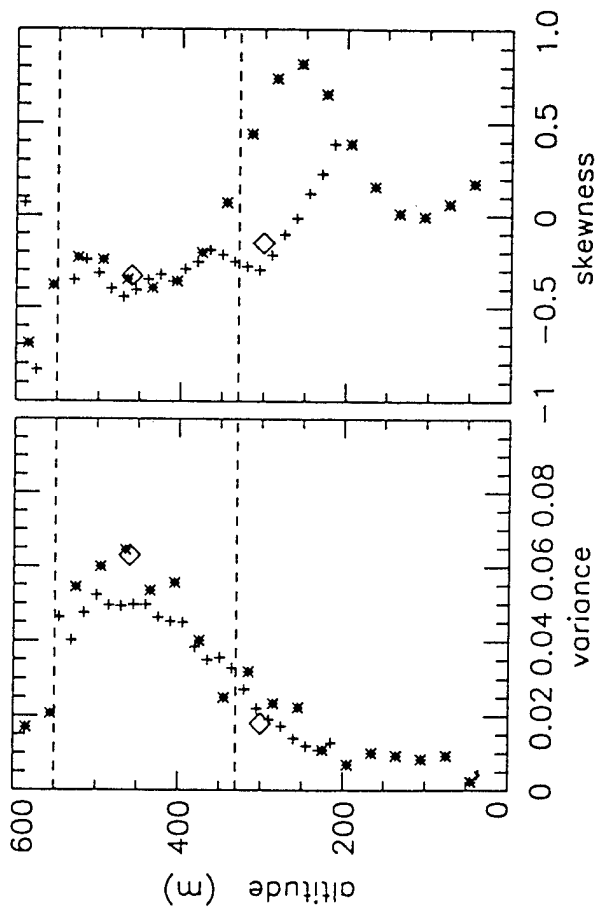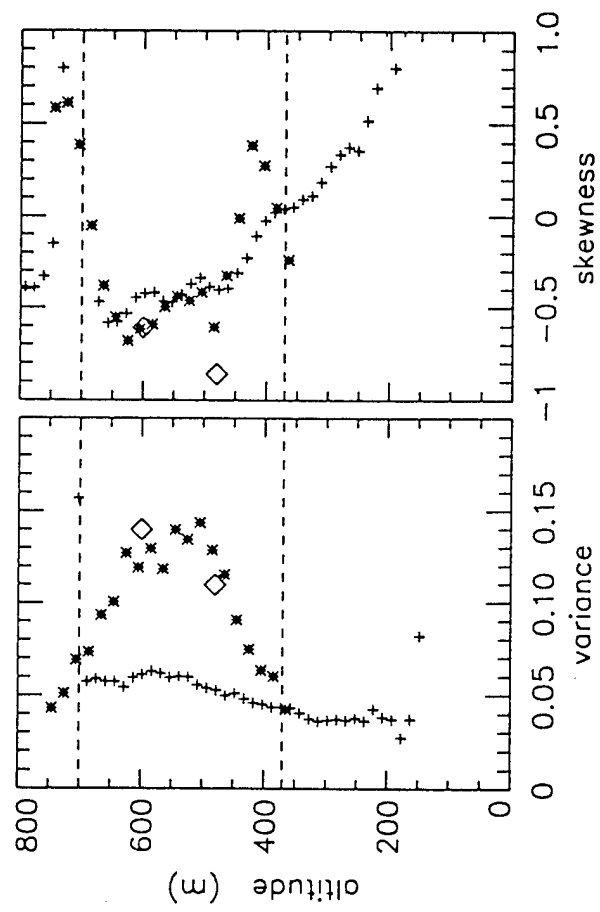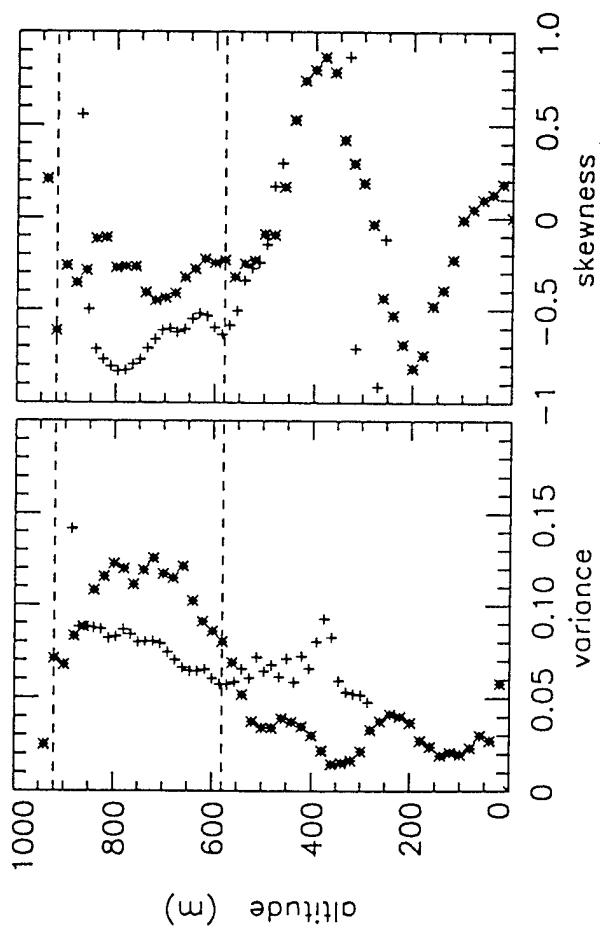
Fig. 20

Retrieval of three-dimensional particle velocity from airborne Doppler radar data

D. Leon and G. Vali

Department of Atmospheric Science, University of Wyoming, Laramie, WY

February 4, 1998

Abstract

A technique has been developed for the retrieval of three dimensional particle velocities from Doppler data obtained with an airborne radar. The 95 GHz radar was mounted on the University of Wyoming KingAir aircraft. The retrieval technique is derived from the Velocity Azimuth Display (VAD) analysis and is termed the Airborne Velocity Azimuth Display (AVAD). Data for this analysis is taken when the radar beam is scanned by the turning of the aircraft. As in VAD analysis a functional form for the horizontal variation of the velocity of the scatterers must be assumed. The components of the velocity field are then determined using a least-squares fit to the Doppler velocities. The AVAD technique differs from VAD analysis because of the mobility of the platform and its proximity to regions of interest, and due to geometric considerations dictated by the turning of the aircraft. The analysis region is only a few km in diameter – considerably smaller than for a ground based VAD analysis. This reduces the required area of cloud coverage and the importance of horizontal variations in the windfield. However, the reduced analysis area also limits the accuracy with which higher order characteristics of the windfield, such as divergence, can be resolved.

This paper presents the AVAD technique and describes the data processing required. Results from multiple AVAD analyses from flights on two days are presented and are shown to be in generally good agreement with winds measured by sensors onboard the KingAir.

1

1 Introduction

Knowledge of air motions is fundamental for the understanding of the microphysical and dynamic processes that determine the evolution of clouds and storm systems. Consequently a wide variety of techniques has been developed to measure the winds. Different techniques give either profiles of winds as a function of height or two or three dimensional wind fields.

Radiosondes and aircraft based soundings are some of the most common means of obtaining wind profiles. These soundings also provide valuable thermodynamic information, however the measurements are taken along a line making it difficult to assess the variability of the measurements and how representative they are of the volume.

Where there are sufficient scatterers wind profiles and wind fields can also be determined through the use of Doppler radars and their derivatives. The fundamental limitation of Doppler radars, that they only measure the radial component of velocity, can be overcome with the use of two common approaches. The first involves the use of multiple Doppler radars (or one mobile radar) that observe the same volume from multiple angles. The second approach makes use of a single Doppler radar combined with assumptions about the horizontal form of the windfield.

Multiple-Doppler techniques allow three-dimensional winds to be calculated over a grid. This allows the spatial variability of the wind field on scales greater than the grid spacing to be observed directly, while variations smaller than the grid spacing are averaged. Ground based dual-Doppler radar analysis is restricted to a small region determined by the location of the radars. Airborne multiple-Doppler analyses, such as described by Jorgensen, Matejka, and DuGranrut (1996), take place over much larger regions. The analysis regions is determined by the aircraft flight pattern, rather than being dictated by a fixed radar location.

The velocity azimuth display technique (VAD) analysis is an example of the second type of approach to resolving winds from Doppler radar. This is one of the earliest applications of Doppler radar. The VAD technique was described in 1960 by Probert-Jones, Lhermitte and Atlas in 1961, and later discussed in more detail by Browing and Wexler (1968) and Matejka and Srivastava (1991). A single radar is scanned in azimuth while mantaining a fixed elevation angle, thus the data comes from a thin shell of a cone emanating from the radar. The wind profiles retrieved can be argued (through the use of the divergence theorem) to be representative of the volume. Wind

2

profilers can be considered to be a degenerate adaptation of the VAD analysis, where the velocity is sampled in only three or four different azimuths. Generally, low elevation angles are used in the VAD analysis to limit the contribution of particle fallspeeds to the Doppler velocities. The low elevation angles combined with the distance from the radar to the regions of interest results in a large area over which the VAD analysis is done.

The millimeter radar mounted on the University of Wyoming KingAir aircraft allows for the development of a VAD based technique. The radar antenna is mounted so as to produce a beam that points to the right of the aircraft. The radar beam can be redirected upwards by means of a reflector plate. This radar uses a short 3.16 mm wavelength that allows a narrow 0.7° beam with a reasonable small (0.3 m) antenna. However this wavelength is much more strongly attenuated by liquid water than longer wavelengths. Details of the radar implementation are included in table 1.

The fixed orientation of the radar beam prevents the adaptation of airborne multiple-Doppler radar techniques to this case. However, the radar beam can be scanned by turning the aircraft. The aircraft bank during a turn results in a scanning geometry silimar to that of a ground-based radar scanning in azimuth. The effective elevation angle of the scan is controlled by the roll angle of the aircraft which in turn is determined by airspeed and turn radius. Thus, this angle cannot be selected for purely meteorological reasons. The geometry of the radar beam during a turn is shown in Figure 1. Depending on the turn direction and the radar beam orientation the radar beam describes a cone that converges above the flight track (up-looking beam either turn direction), a cone that converges below the flight track (side-looking beam, right turn), or a cone that diverges above the flight track (side-looking beam, left turn).

The similarity between the ground-based and airborne geometries implies that VAD analysis can be adapted to the airborne case, and leads the authors to call this the Airborne Velocity Azimuth Display (or AVAD) technique. Radar data from a turn is broken into data subsets corresponding to a constant altitude, and the analysis is carried out out separately for each level.

The diameter of the analysis region is determined primarily by the diameter of the turn, beam orientation, and turn direction. Typically the diameter of the turn is roughly 3 Km for a roll angle of 30° . This generally results in an analysis region with a diameter between 0.5 and 4 km although the analysis region may become as large as 10 km for the side-looking left turn

3

case. The typical range gate spacing of 30 m gives a vertical resolution of about 20 m. Thus the AVAD technique is a cloud scale tool that can provide high vertical resolution wind profiles with less than 60 seconds worth of data. These profiles provide a context for the data gathered by the in situ probes mounted on the aircraft and partially bridge the gap in scale between the data gathered by the in-situ probes and data gathered by other tools such as ground based radars.

The data used in this paper comes from two cases: a Nimbostratus studied in Wyoming in 1992 and a Stratus from off the Oregon coast that was studied in 1995. The in-situ winds measured from the KingAir will be used for comparisons with the results of the AVAD analysis.

2 Data Processing

2.1 Beamvector Notation

The complexity involved in describing the orientation of the radar beam when the aircraft is not flying straight and level prompts the introduction of a simplifying notation, the development of the notation presented in this section paralells that of Lee et al (1994). The beamvector, $\hat{b}$, is a unit vector aligned along the center of the radar beam. The width of the radar beam, while finite, is sufficiently small that for most purposes the beam can be treated as a line. The measured Doppler velocity can be written in terms of $\hat{b}$ as:

$$V_{Dopp} = \hat{b} \cdot V_p \tag{1}$$

where V_p is the three-dimensional velocity of the scatterers relative to the platform. For a ground based radar the components of $\hat{b}$ can be written in terms of the azimuth (ϕ) and elevation (α) angles as:

$$
\begin{aligned}
b_x &= \cos(\alpha)\cos(\phi) \\
b_y &= \cos(\alpha)\sin(\phi) \\
b_z &= \sin(\alpha)
\end{aligned}
\tag{2}
$$

where b_x, b_y, and b_z refer respectively to the East, North, and vertical components of $\hat{b}$.

Given aircraft orientation and attitude data – pitch, roll, and heading angles – the beamvector in aircraft coordinates, $\hat{b}_{ac}$, can be transformed into ground coordinates, $\hat{b}_{gr}$. This coordinate transformation is accomplished through the use of three rotations about each of the aircraft axes (Lenschow 1971)

$$\hat{b}_{gr} = T\hat{b}_{ac} \tag{3}$$

where T is the transformation matrix which in turn can be expressed as the product of three transformation matrices about the aircraft axes:

$$T = H(PR) \tag{4}$$

5

with the matrices $\mathbf{H}$, $\mathbf{P}$, and $\mathbf{R}$ given by :

$$\mathbf{R} = \begin{pmatrix} 1 & 0 & 0 \\ 0 & \cos(\phi) & -\sin(\phi) \\ 0 & \sin(\phi) & \cos(\phi) \end{pmatrix} \tag{5}$$

$$\mathbf{P} = \begin{pmatrix} \cos(\theta) & 0 & \sin(\theta) \\ 0 & 1 & 0 \\ -\sin(\theta) & 0 & \cos(\theta) \end{pmatrix} \tag{6}$$

$$\mathbf{H} = \begin{pmatrix} \sin(\psi) & \cos(\psi) & 0 \\ \cos(\psi) & -\sin(\psi) & 0 \\ 0 & 0 & -1 \end{pmatrix} \tag{7}$$

where ψ, θ, and ϕ are the heading, pitch, and roll angles respectively as defined in Figure 2. In this application $\hat{b}_{ac}$ is constant, thus only $\mathbf{T}$ must be computed to obtain the instantaneous value of $\hat{b}_{gr}$. Hereafter $\hat{b}$ will be used to refer to the beamvector in ground coordinates unless otherwise noted

2.2 Correction for Aircraft Motion

Doppler velocity is measured with respect to the aircraft. Unless the aircraft velocity is perpendicular to $\hat{b}$ the measured Doppler velocity is not the same as would be measured by a fixed radar. To express the velocity in a ground relative frame the component of the aircraft motion in the Doppler velocity must be removed. Using the notation introduced in the previous section the Doppler velocity measured from the aircraft can be expressed as:

$$V_{Dopp} = \hat{b} \cdot V_p - \hat{b} \cdot (V_{ac} + \Omega_{ac} \times R_{radar}) \tag{8}$$

where V_{ac} is the aircraft velocity vector, Ω_{ac} is the aircraft rotation rate vector, and R_{radar} is the moment arm from the inertial navigation system (INS) to the radar. The second term on the right hand side of equation 8 represents the contribution of the aircraft motion to the Doppler velocity. The sum $(V_{ac} + \Omega_{ac} \times R_{radar})$ is the velocity at the radar.

The horizontal components of V_{ac} are determined from INS and GPS data. GPS data are used for the low frequency components (those less than 0.02 Hz) and INS data are used for higher frequencies. The vertical component of the aircraft velocity is calculated from the INS vertical acceleration and pressure data. The aircraft attitude (pitch, roll, and heading) and the rotation rate (pitch rate, roll rate, and heading change rate) are derived from the INS.

The aircraft velocity V_{ac} is generally close to an order of magnitude greater than the velocity of the target, thus both V_{ac} and $\hat{b}$ must be known accurately otherwise errors in the aircraft motion removal might result in errors that are significantly larger than the velocity of the targets.

A precise determination of the beamvectors in aircraft coordinates must be made. An error of only 1° along the flight track will cause a bias of 1.5 m/s in the Doppler velocity at a typical aircraft speed of 90 m/s. The antenna installation was designed to result in a beam oriented 3.6° forward of the vertical in the up-looking case, or to the right (perpindicular to the aircraft centerline) in the side looking case. The up-looking beam orientation was chosen to compensate for the typical angle of attack of the aircraft thus resulting in a true vertically pointing beam during straight and level flight.

However, the installation could not be assumed to be sufficiently accurate and direct measurements of the beam orientation were needed. The high velocity of the aircraft can be used to an advantage in determining the beam orientation by the Doppler velocity of a target of known velocity. The

side looking beam orientation is determined by using the ground as a velocity reference. $\hat{b}_{ac_{side}}$ is set to minimize the residual velocity of the ground. Determination of the up-looking beam orientation is significantly more difficult than the side-looking case due to the absence of a convenient velocity reference. During the Small Cumulus Microphysics Study (SCMS) project the KingAir flew under the Merlin aircraft (operated by Meteo France) and received a radar return from it. This aircraft carries both INS and GPS navigation equipment and could therefore be used as a velocity reference. $\hat{b}_{up}$ is set to satisfy the relationship

$$V_{Doppler} = \hat{b}_{up} \left(V_{Merlin} - V_{KingAir} \right) \tag{9}$$

The up-looking beam has been calculated to point 3.0° forward of up, while the side looking beam has been estimated to point 1.0° back of right.

The determination of the beam orientations has focused on the alignment of the beams along the aircraft centerline. This is the most critical component of the beam orientation, however there is potential for the beam to be misalinged perpendicular to the aircraft centerline. That is, the up-looking beam may be misaligned to the left or right of vertical, while the side-looking beam may be misaligned above or below the horizontal. This is not as significant for the side-looking beam case since the maximum vertical speeds of both the scatterers and the aircraft are not very large compared to their horizontal speeds. However, in the up-looking case a misalignment could be significant as horizontal velocities can be large while vertical velocities are generally small. Unfortunately, it is extremely difficult to evaluate these errors.

The accuracy with which the pitch and roll angles are known is limited by the Schuler oscillation. A Schuler oscillation of (peak-peak) amplitude of 5 km corresponds approximately to a 0.02° error in aircraft attitude. Currently the pitch and roll angles are not corrected for the effects of the Schuler oscillation, however these effects are close to an order of magnitude smaller than the uncertainties in beam orientation which are believed to be about 0.25° and 0.4° for the side and up looking beams respectively.

The component of aircraft motion in the measured Doppler velocities $(\hat{b} \cdot (V_{ac} + \Omega_{ac} \times R_{radar}))$ is calculated for each profile and corrected for in a separate processing step. Errors in both the beamvectors and the aircraft velocity translate into errors in the measured Doppler velocity.

The residual velocity of the ground once the aircraft motion has been removed is used to provide a quantitative assessment of the accuracy of the

aircraft motion removal for the side-looking beam. The residual Doppler velocities of the ground are generally less than $0.4ms^{-1}$, however high frequency ($> 1Hz$) components of aircraft motion are not corrected as accurately (possibly due to timing problems), so the aircraft motion removal is significantly worse in turbulent conditions.

2.3 Constant altitude data subsets

The aircraft flies at varying altitudes and with varying roll and pitch angles, thus, a single range gate does not correspond to a fixed altitude. The position of the center of a radar gate, $\mathbf{X_{gate}}$, can be calculated from $\hat{\mathbf{b}}$ and the aircraft position $\mathbf{X_{ac}}$.

$$\mathbf{X_{gate}} = r_{gate}\hat{\mathbf{b}} + \mathbf{X_{ac}} \tag{10}$$

$$Z_{gate} = r_{gate}b_z + Z_{ac} \tag{11}$$

This equation can be solved for the range to a given altitude.

$$r = \frac{Z - Z_{ac}}{b_z} \tag{12}$$

A data subset is then constructed for an altitude by linearly interpolating between the range gates nearest the chosen altitude. Data subsets that are separated by more than twice the range gate spacing are completely independent.

3 The AVAD technique

3.1 Least-Squares solution

Once the Doppler velocity has been corrected for aircraft motion and data subsets corresponding to fixed altitudes have been constructed, then the inversion to determine the winds can be done. The traditional method for determining the wind field made use of Fourier analysis. The use of Fourier type methods is not an option for the airborne analysis as changing aircraft altitude and roll leads to irregular spacing of data points. Rather, a generalized least-squares solution similar to the methods used by Easterbrook (1975) and Testud et. al. (1980) is utilized. The least-squares solution is significantly more robust than the spectral methods and can tolerate gaps in the data as well as irregular spacing. The least-squares solution requires that we be able to state the problem in the form :

$$\mathbf{V_{Dopp}} = \mathbf{GV} \tag{13}$$

where $\mathbf{V_{Dopp}}$ is a vector of the measured Doppler velocities, $\mathbf{G}$ is the forward matrix describing how the model parameters are weighted, and $\mathbf{V}$ the vector to be retrieved.

The first step is to assume a functional form for $\mathbf{V}(x, y, t)$. The analysis is done separately for each altitude so no assumption about the vertical variation of the velocity field is needed. Results from a series of altitudes are assembled into a profile.

The simplest form for the AVAD analysis is the horizontally homogeneous windfield :

$$V_x(x, y, t) = V_{x0}$$
$$V_y(x, y, t) = V_{y0} \tag{14}$$
$$V_z(x, y, t) = V_{z0}$$

where the terms V_{x_0}, V_{y_0}, and V_{z_0} are constant. Browning and Wexler (1968) presented a more sophisticated velocity field where the components of the

velocity field vary linearly in the horizontal:

$$V_x(x, y, t) = V_{x0} + \overline{\frac{\partial V_x}{\partial x}}x + \overline{\frac{\partial V_x}{\partial y}}y$$

$$V_y(x, y, t) = V_{y0} + \overline{\frac{\partial V_y}{\partial y}}y + \overline{\frac{\partial V_y}{\partial x}}x \qquad (15)$$

$$V_z(x, y, t) = V_{z0} + \overline{\frac{\partial V_z}{\partial x}}x + \overline{\frac{\partial V_z}{\partial y}}y$$

This form of the wind field allows for the determination of divergence as well as stretching and shearing deformations. The terms corresponding to horizontal variations of the vertical component have been added to the formulation of Browning and Wexler (1968) because with the higher elevation angles employed during this analysis these components may become significant.

The equation for Doppler velocity at one altitude (eqn. 1) can be rewritten in matrix form as:

$$V_{Dopp} = \begin{bmatrix} b_x & b_y & b_z \end{bmatrix} \begin{bmatrix} V_x \\ V_y \\ V_z \end{bmatrix} \qquad (16)$$

A series of n measurements of the Doppler velocity with an assumed horizontally homogeneous windfield can be written as :

$$\begin{bmatrix} V_{Dopp_1} \\ V_{Dopp_2} \\ V_{Dopp_3} \\ \vdots \\ V_{Dopp_n} \end{bmatrix} = \begin{bmatrix} b_{x_1} & b_{y_1} & b_{z_1} \\ b_{x_2} & b_{y_2} & b_{z_2} \\ b_{x_3} & b_{y_3} & b_{z_3} \\ \vdots & \vdots & \vdots \\ b_{x_n} & b_{y_n} & b_{z_n} \end{bmatrix} \begin{bmatrix} V_x \\ V_y \\ V_z \end{bmatrix} \qquad (17)$$

Similarly, for the linearly varying velocity field case, a series of measurements

of the Doppler velocity can be written :

$$
\begin{bmatrix} V_{Dopp_1} \\ V_{Dopp_2} \\ V_{Dopp_3} \\ \vdots \\ V_{Dopp_n} \end{bmatrix} = \tag{18}
$$

$$
\begin{bmatrix} b_{x_1} & b_{y_1} & b_{z_1} & b_{x_1}x_1 & b_{y_1}y_1 & b_{x_1}y_1 & b_{y_1}x_1 & b_{z_1}x_1 & b_{z_1}y_1 \\ b_{x_2} & b_{y_2} & b_{z_2} & b_{x_2}x_2 & b_{y_2}y_2 & b_{x_2}y_2 & b_{y_2}x_2 & b_{z_2}x_2 & b_{z_2}y_2 \\ b_{x_3} & b_{y_3} & b_{z_3} & b_{x_3}x_3 & b_{y_3}y_3 & b_{x_3}y_3 & b_{y_1}x_3 & b_{z_3}x_3 & b_{z_3}y_3 \\ \vdots & \vdots & \vdots & \vdots & \vdots & \vdots & \vdots & \vdots & \vdots \\ b_{x_n} & b_{y_n} & b_{z_n} & b_{x_n}x_n & b_{y_n}y_n & b_{x_n}y_n & b_{y_n}x_n & b_{z_n}x_n & b_{z_n}y_n \end{bmatrix} \begin{bmatrix} V_x \\ V_y \\ V_z \\ \frac{\partial V_x}{\partial x} \\ \frac{\partial V_y}{\partial y} \\ \frac{\partial V_x}{\partial y} \\ \frac{\partial V_y}{\partial x} \\ \frac{\partial V_z}{\partial x} \\ \frac{\partial V_z}{\partial y} \end{bmatrix}
$$

Subsets of the terms in equation 18 can also be used as appropriate for a given situation.

The matrix of beamvectors (for the selected form of the velocity field) is then inverted using a singular value decomposition (Bevington 1969, Menke 1992) such that:

$$
\mathbf{V}_{est} = \mathbf{G}^{-g} V_{Dopp} \tag{19}
$$

The estimated velocity field parameters can then be used, together with the matrix of beamvectors, to produce an array of predicted Doppler velocities.

$$
V_{Dopp_{pre}} = \mathbf{G} \mathbf{V}_{est} \tag{20}
$$

Comparison between the predicted and actual data values can reveal how well the wind fields have been fit and the appropriateness of the velocity field form.

In our application the diameter of the analysis regions is reduced by an order of magnitude compared to a typical ground based VAD analysis. This

reduces the variation in the winds across the analysis domain caused by higher order characteristics of the windfield. This makes the assumptions that must be made about the functional form of the windfield significantly less stringent, but also reduces the accuracy with which the higher order charicteristics of the windfield can be determined. Thus, the horizontally homogeneous form for the wind field will be used in this paper. The vertical component of velocity, V_z, retrieved in this analysis is the vertical particle speed which is the difference between the vertical wind component w and the terminal velocity of the scatterers, V_t. No attempt to separate w from V_t is made due to the weaknesses inherent in attempting to utilize a $Z - V_t$ relationship at W band and due to the high effective elevation angles used – increasing the importance of having an accurate $Z - V_t$ relationship relative to low elevation angle applications.

3.2 Error Analysis

The estimated value of the component of the velocity field is a sum of the input data weighted by the appropriate components of the inverse matrix. The ith parameter of the velocity field can be expressed as:

$$V_i = \sum_{j=1}^{n} G_{ij}^{-g} V_{Dopp_j} \qquad (21)$$

The variance of the Doppler velocity can be used to calculate the variance of the estimated parameter. Turbulence with scales greater than the pulse volume leads to correlation between neighboring points. Thus, it would be inappropriate to assume that the data points were independent, rather it is assumed that the covariance between two data points is a function only of the time between the samples. Thus, the variance of the measured Doppler velocities can be estimated from the difference between the observed values and the least-squares fit predicted by the forward model and the estimated winds.

$$\sigma_d^2 = \frac{1}{n-m} \sum_{i=1}^{n} \left(V_{Dopp_i} - V_{Dopp_{pre_i}} \right)^2 \qquad (22)$$

where m is the number of model parameters (3 in the case of assumed horizontal homogeneity, 9 for the linearly varying windfield). The value of σ_d generally falls in the range of $0.2ms^{-1}$ to $1ms^{-1}$ for the stratiform cases presented it seems probably that convective cases might have significantly greater σ_d. Figure 3 shows an example of the measured Doppler velocities and the least square fit values for a range of altitudes. It is apparent in this figure that deviation of the winds about the least-squares fit is not random, but rather consists of semi-regular oscillations about the fit value.

The standard deviation of the wind field parameters can then be estimated given σ_d and the weights of the inverse matrix $\mathbf{G}^{-g}$.

$$Var(V_i) = \sum_{j=1}^{n} \sum_{k=1}^{n} G_{ij}^{-g} G_{ik}^{-g} Cov(V_{Dopp_j}, V_{Dopp_k}) \qquad (23)$$

Neighboring points are usually correlated because of turbulence, waves, and other velocity variations that are smaller than the area of the analysis but larger than the volume of a single pulse. The correlation between measurements tends to decay for points that are separated further apart in space and

15

time. With the assumption that that the correlation between datapoints is a function only of the time between the samples. Thus, equation 23 can be rewritten in terms of the autocorrelation as:

$$Var(V_i) = \sum_{j=1}^{n} G_{ij}^{-g}\sigma_d^2 + 2\sum_{j=1}^{n}\sum_{k=j+1}^{n} G_{ij}^{-g}G_{ik}^{-g}\sigma_d^2 R(|k-j|) \tag{24}$$

where $R(|k-j|)$ is the autocorrelation between the jth and kth samples. This is not the variance of the component of the wind but rather the variance of the estimate of that parameter. The standard deviation of the parameter estimates declines rapidly as the length of the turn segment increases. Figure 4 shows the rapid decline in standard deviation of the mean wind terms as a function of the length of the turn segment. This estimate assumes that the variance of the data is constant and there is one independent sample of velocity per degree and that the radar beam is initially poined to the East and that the turn uses a roll angle of 30°. It is apparent from the figure that 90° of turn is a realistic minimum for the AVAD analysis and that significant gains in accuracy can be achieved by using a turn segment closer to 180° long. Extending the turn beyond 180° yields only minimal gains in accuracy while potentially increasing the effects of temporal variations in the windfield. The standard deviation of the parameters for the cases presented was generally between 0.05 ms^{-1} and 0.3 ms^{-1}.

The effects of a bias in the Doppler velocities can also be calculated. While a bias is improbable for a ground based radar it can easily result from errors in the removal of aircraft motion. The effects of a bias on a given parameter are given by the sum of the weights of the inverse matrix.

$$V_i = \sum_{j=1}^{n} G_{ij}^{-g}\left(V_{Dopp_j} + V_{Bias}\right) \tag{25}$$

Where V_{Bias} is a constant bias included in each velocity measurement. The effects of a bias on different velocity parameters differ depending on the sum of the terms of G^{-g} for that parameter. The horizontal velocity is unaffected by a bias for turn segments longer than about 20 degrees. A bias has a greater effect on the vertical velocity component as and on higher order parameters such as divergence. A bias of 1 ms^{-1} corresponding to a 0.6° error in beam pointing direction for an airspeed of 100 ms^{-1}. would result in a bias of 1.4 ms^{-1} on the vertical component for a turn with a 45° bank angle and $2ms-2$ for a turn with an elevation angle of 30° (Side-looking with a roll

16

of 30° or up-looking with a 60° roll). . Errors in the aircraft velocity that are constant for the time of the analysis amount to an inadvertent Galilean transformation and cannot be detected unless the return from the ground or some other reference is included in the analysis. These errors affect all altitudes equally.

4 Results

The AVAD analysis described in the previous sections has been applied to data from two cases: A nimbostratus case from October 31, 1992, and a stratus case from September 14, 1995. These two cases were selected because the wind profiles include several interesting features, there are multiple turn segments with sufficient radar data for the AVAD analysis, and winds measured from the KingAir are available for comparison with the AVAD results.

4.1 Nimbostratus – October 31, 1992.

The flight on October 31, 1992. was in a Nimbostratus that developed to the north-east of Wheatland, Wyoming. The cloud layer extended from below 1.5 km up to almost 9 km (msl) with precipitation reaching to the ground. Features of interest in this case include a well defined bright band at the base of a layer of significant shear. Generating cells were embedded near cloud top (8.5 km msl) and the ice crystals formed in these cells formed high-reflectivity fallstreaks that extended through a region of shear and down to a region of uniform reflectivities at 6 km.

The radar beam was fixed in the up-looking position for this flight. The main part of the flight consisted of a series of East-West flight legs conducted at successively decreasing altitudes ranging from 7 to 1.5 km. Data for the AVAD analysis are taken from the turns between flight legs. Radar data files from this day are short, generally less than one minute of data. Thus, multiple radar data files are incorporated into a single analysis.

This increases the accuracy of the analysis by including a larger range of heading and roll angles. Figure 5 shows the flight track and the data used for the AVAD analyses. Shaded areas mark the radar data used. Five turns have sufficient radar data to attempt the AVAD analysis. The thickness of the cloud layer is over double the radar range of 3 km. A wind profile through the entire depth of the cloud layer must be pieced together from multiple analyses taken at different flight levels. Results from the five AVAD analyses and in-situ data from the KingAir are shown in Figure 6. Between 3 km and 5.5 km there are several overlapping profiles, allowing the consistency of the results to be examined, although variations between the profiles may also be due to spatial and temporal variations in the wind field. The most obvious feature in the profile is the melting layer between 2.2 and 2.4 km. In this region fallspeeds increase from 1.5 to 4.5 ms^{-1}, while reflectivities increase

18

from 0 dBz to 10 dBz at the bottom of the melting layer. The wind profiles from the KingAir sounding and the five AVAD analyses show a decrease in windspeeds from 3.3 km to 4.5 km. Below 4 km the wind direction remains steady. Above 4 km the winds back sharply at more than 40° per km. Some minor features are also apparent in several of the profiles. Three or four oscillations in the wind direction of about 30° are evident in the profiles between 4400m and 5500m, a region in which the windspeeds are steady.

4.2   Marine stratus – September 14, 1995.

Observations on this day were made off the coast of Oregon, in a 400 m thick stratus layer with a distinct cellular structure. Drizzle from the stratus provides sufficient reflectivity to to allow the AVAD analysis to be carried out from cloud top all the way to the ocean surface. Average reflectivity increased from -16 to -5 dBZ in the first 100 m below cloud top and remained nearly constant through the rest of the cloud layer.

The flight consisted primarily of north-south oriented legs ranging from 25 to 40 km in length. There are seven suitable data segments for the AVAD analysis, however one of these was too close to cloud top and provides results for only 80 m below cloud top. Of the six profiles used in the composite analysis four are from the southern end of the flight legs, one is from the northern end, and one is from near the center of the flight legs. These cases are spread over slightly more than one hour of flight. Figure 7 shows the flight track for this day and the regions used for the AVAD analyses. The composite of the six profiles and the KingAir measured winds are shown in Figure 8.

Four of the cases for the radar analysis are from the up-looking setting of the radar beam, while two of the analyses are done with data from the side-looking beam. The up-looking cases provide data from slightly above the flight track (usually about 200 m) to echo top. The side looking AVAD profiles are taken from 90° − 270° turns and thus give data from both above and below the flight level. In-situ winds measured by the KingAir are available from 50 m above the ocean surface to well above cloud top.

Wind speeds increase from roughly 2 ms^{-1} at 200 m and reached 7 ms^{-1} near cloud top. Between 200 m and 350 m the mean shear is over 27 ms^{-1} per km. Below 200 m windspeeds increase to 4 ms^{-1} at the ocean surface. Particle fall speeds remain fairly steady declining from about -1.1 ms^{-1} to -.9 ms^{-1} near cloud top. Near the 200m level winds change from 180° below to

19

330° above that level. The windshear evident in the AVAD profiles can also be observed in the reflectivity images. A representative North-South cross section of reflectivity from September 14 is shown in figure 9. The windshear seen between 200 and 400 m in the AVAD profiles is also evident in the cross section , as shown by the curvature of the high-reflectivity fallstreaks. The cross section is almost parallel to both the wind and the windshear vectors. The total shear between 200 and 400 m can be deduced from the final slope of the fallstreaks to be between 4 and 6 times the fallspeed of the scatterers – this is consistent with the AVAD determined 5 to 7 ms^{-1} velocity difference between 200 and 400 m for scatterers with a fallspeed of between -0.9 and $-1.1ms^{-1}$.

Overall, the KingAir and AVAD retrieved winds show good agreement with the windspeeds and directions measured by the KingAir. Individual AVAD derived profiles are very smooth in the vertical. Thus, it seems probable that the spread in the KingAir measured wind speeds and directions as well as the difference between AVAD profiles is due to real variations in the windfield. There are no consistent spatial or temporal trends in wind speed or direction as most data from the different analyses fall within 2 ms^{-1} and 10° of each other. The vertical particle speeds , in the range of $-0.9ms^{-1}$ to $-1.1ms^{-1}$ are consistent with those of drizzle drops of radius 0.1 to 0.2 mm (Beard 1976) which were observed on this day. The side–looking AVAD analyses, D and E, produce poor quality estimates of the vertical particle velocity. The problems with these vertical velocities are primarily due to the low roll angles ($< 30°$) and small amount of data which cause the vertical component of motion to be poorly resolved and allow residual aircraft motion to contaminate the vertical component.

20

5 Conclusions

The AVAD analysis has been shown to be a useful tool for retrieving wind profiles. The data required for the AVAD analysis can generally be obtained from turns required as part of a flight plan. Analyses can be obtained from 45 seconds of data and 90° of a turn.

The ability to obtain multiple AVAD profiles allows for the identification of small or transient features such as the oscillations in wind direction evident between 4.5 and 6 km in figure 6. Whereas time and other constraints may limit the number of aircraft soundings practical to one or two, it is possible to obtain tens of AVAD profiles during a typical two or three hour research flight.

The AVAD analysis provides data on a scale that begins to bridge the gap between the mesoscale information provided by ground-based VAD analysis or multiple Doppler techniques and the data provided by the in-situ probes. This data helps to provide a context for the in-situ data.

This technique is applicable where there are clouds with areas of detectable reflectivity greater than 2 km in diameter. However, the technique is not appropriate in cases were there is significant non-linear variation of the winds across the analysis region, as is likely in small rapidly growing cumulus.

The variations about the least squares value (as shown in Figure 3) are perhaps the most interesting area of the AVAD analysis for further exploration. The Doppler velocities from the Sept 14 case and others show apparently regular oscillations about the least-squares fit value. These variations are particularlly evident in figure 3 where they appear as semi-regular variations of the Doppler velocity about the mean value having a preiod of about 5 seconds (or about 400m at 90 ms^-1). These variations may be due to either small scale velocity structures or to the radar data slicing through higher fall speed fallstreaks. The features display a high degree of vertical continuity and can be seen to evolve from one level to the next, thus precluding the possiblitiy that they are artifacts caused by incorrect aircraft motion removal. These features may play a critical role in organizing the cellular structure evident on that day. A non-linear optimization method similar to that employed by Testud et. al. (1980) should be capable of identifying the wavelength and orientation of these waves. Due to the narrow beamwidth and the proximity of the radar to the analysis region is should be possible to identify features with wavelengths less than 100 m.

5.1 Acknowledgements

Table 1: University of Wyoming millimeter radar specifications

Characteristic	Value	Units	Comments
Wavelength	3.16	mm	
Transmit frequency	94.92	GHz	
Antenna diameter	0.305	m	
Antenna beam width	0.7°		
Antenna gain	49	dB	
Sidelobes	−31	dB	
Radar beam orientation :			
Up-looking	2.8°		forward of vertical
Side-looking	−1.0°		forward of right
Peak transmit power	1.2	kW	
Pulse duration	250	ns	
Pulse repitition frequency	20000	Hz	maximum
Reciever bandwidth	5	MHz	
Minimum detectable signal	−25	dBZ	at 1 km

Samples averaged	400		typical
Unambiguous range	7.5	km	minimum
Unambiguous velocity	31.8	ms^{-1}	maximum
Range resolution	37.5	m	250 ns pulse
Along-track resolution	5	m	typical
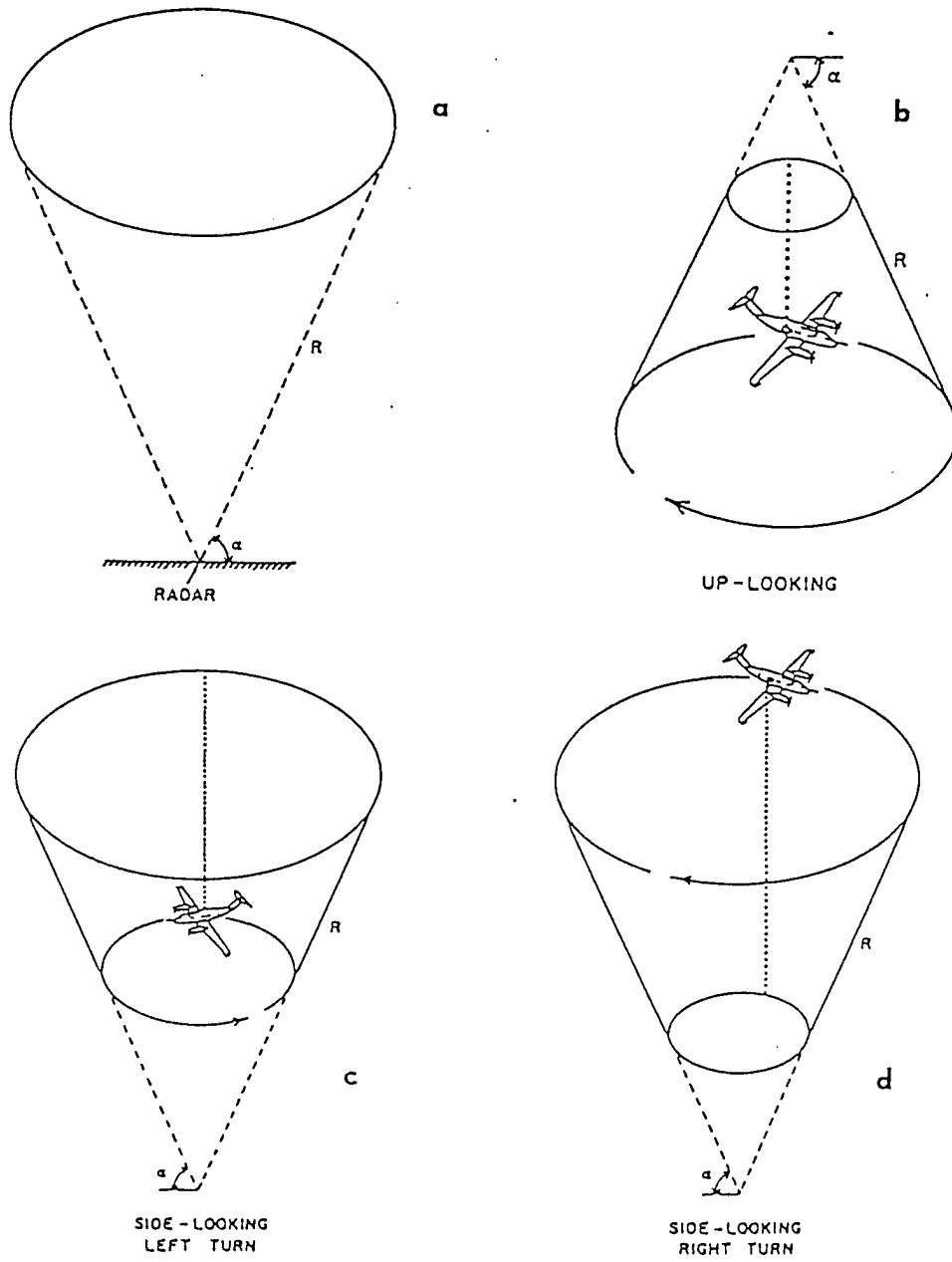
Figure 1: Scanning geometry for: (a) Ground based radar. (b) Up-looking radar beam (left or right turn). (c) Side-looking radar beam – left turn. (d) Side-looking radar beam – right turn.
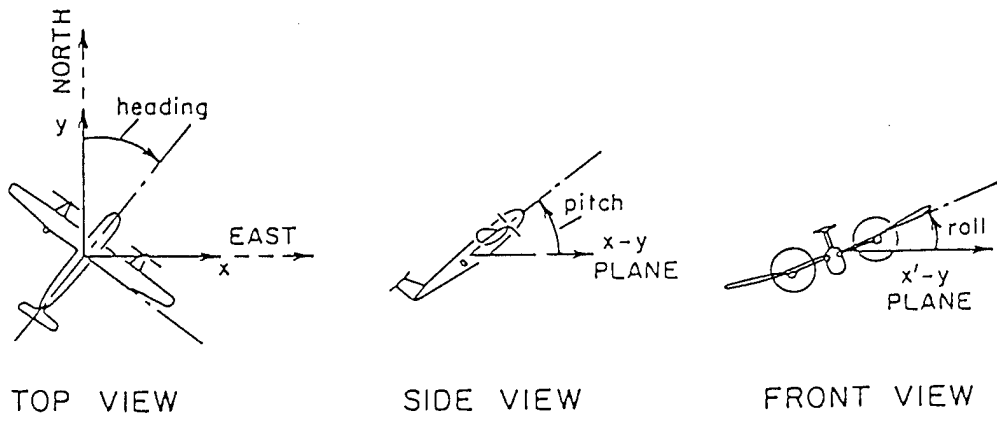
NORTH

y

heading

EAST

x

TOP VIEW

pitch

x-y
PLANE

SIDE VIEW

roll

x'-y
PLANE

FRONT VIEW

Figure 2: Heading (ψ), Pitch (θ), and Roll (ϕ) angles. Adapted from Lenschow (1971).
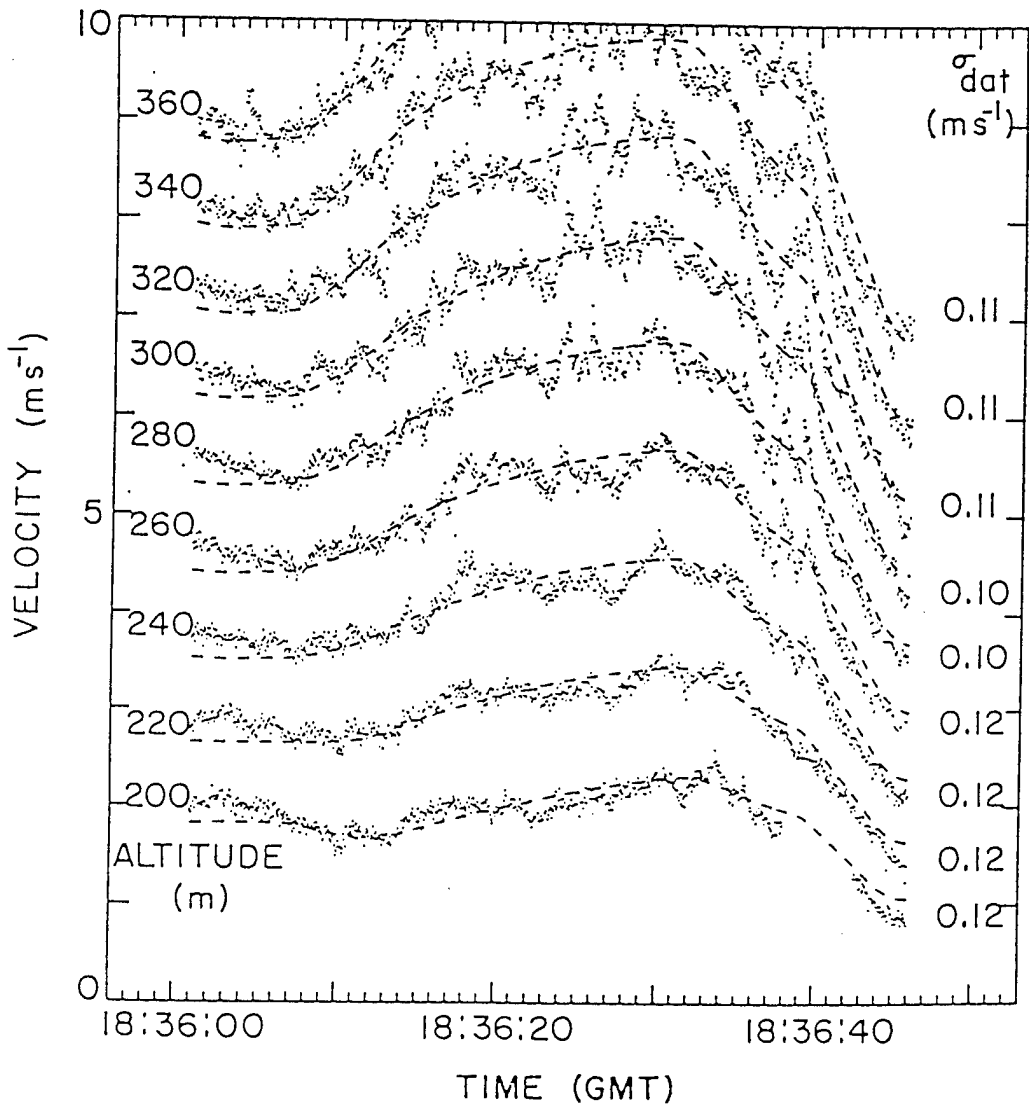
Figure 3: Least-squares fit (dashed line) and measured Doppler velocity (dots)
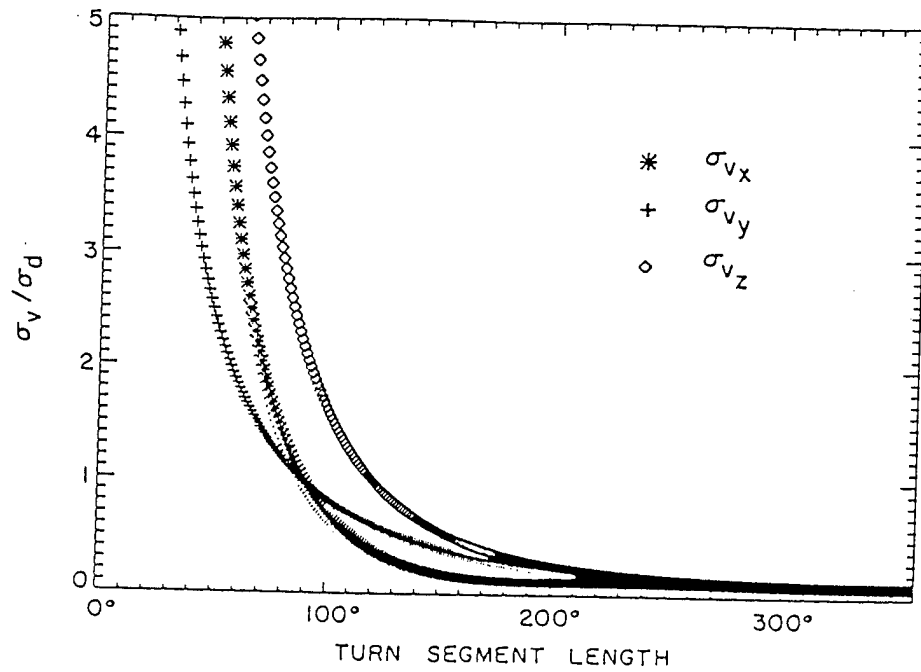
Figure 4: Standard deviation of the velocity component estimates as a function of the length of the turn segment used. One independent Doppler velocity sample per degree is assumed along with an effective elevation angle of 30° with the beam initially pointing East.
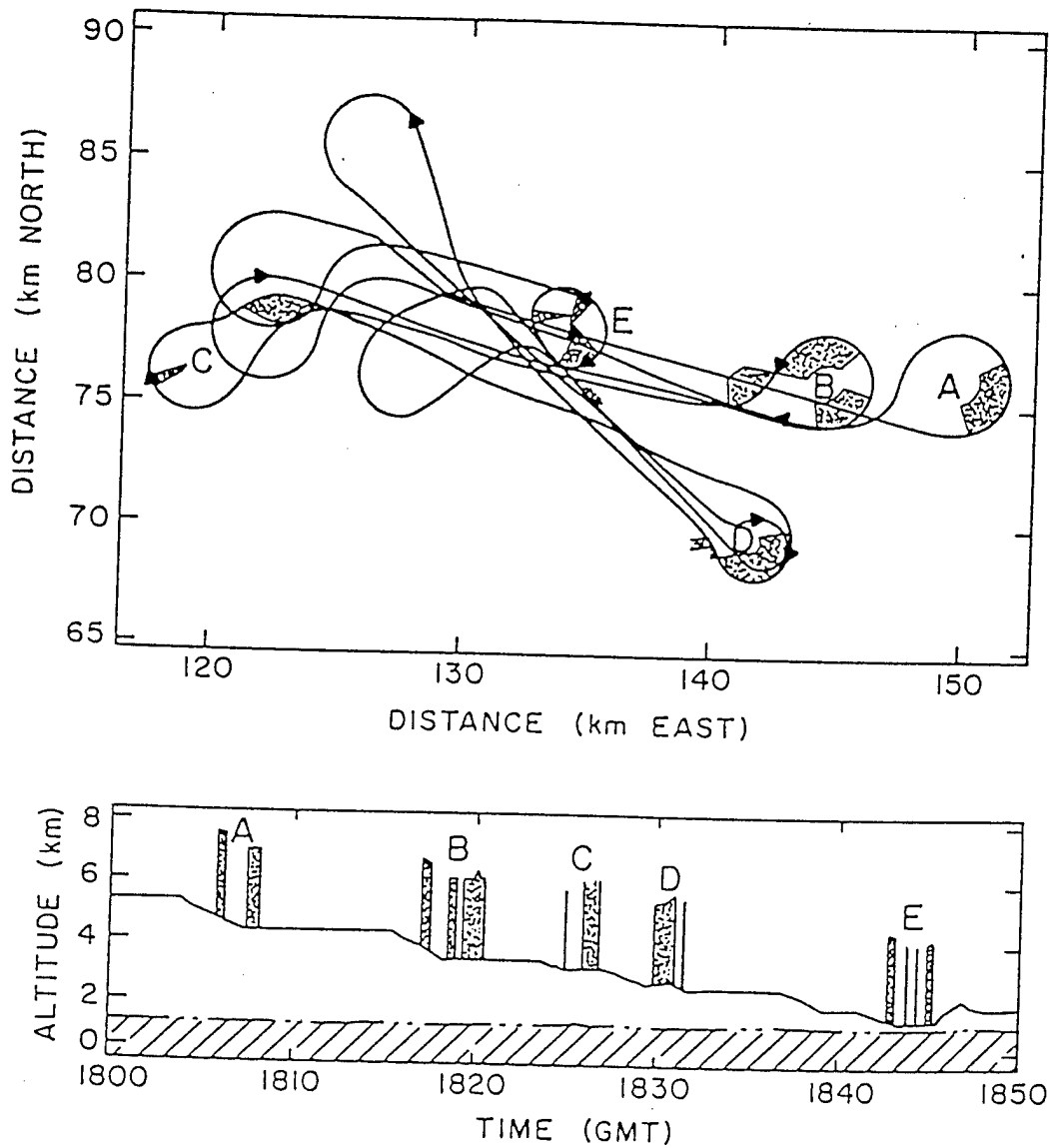
Figure 5: a) Map view of flight tracks and areas of coverage for the AVAD analyses. Labels A-E mark the locations of profiles. b) Flight altitudes and times for the data used in the AVAD analyses. All profiles are up-looking.
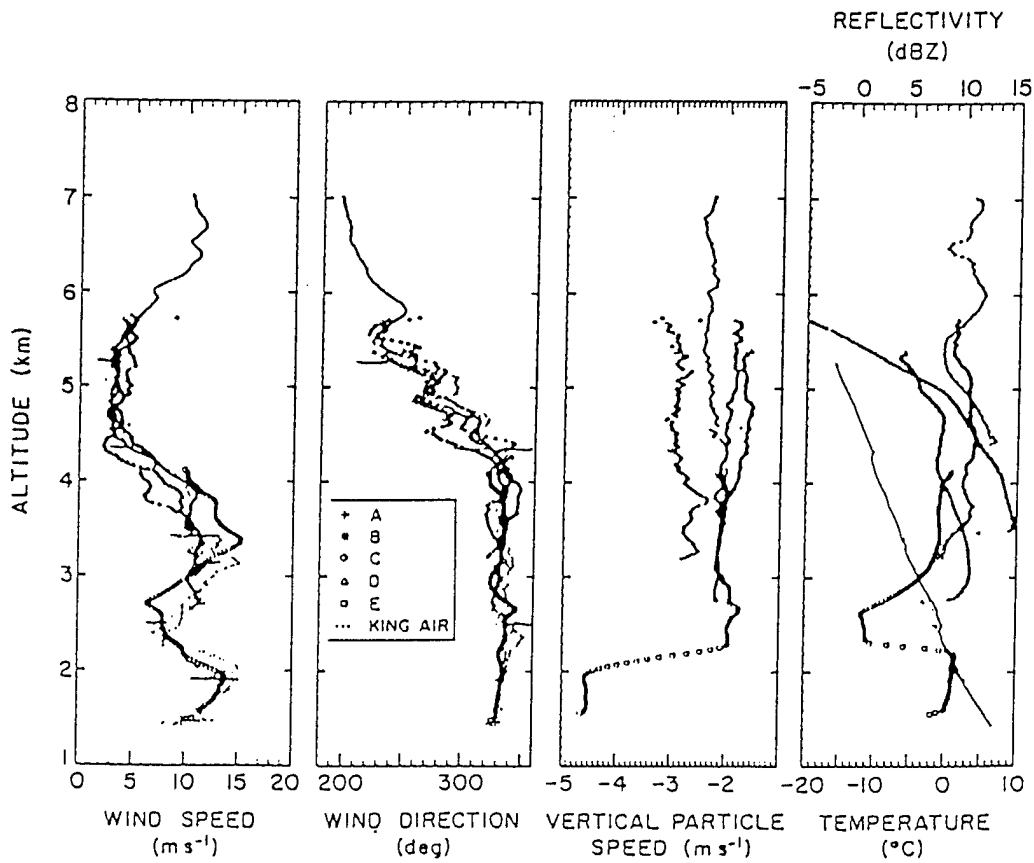
Figure 6: Wind profiles Derived from KingAir data (dots) and AVAD anal-
ysis. a) Wind Speed. b) Wind Direction. c) Vertical particle speed. d)
Temperature and mean reflectivity. Labels A-E on the profiles correspond to
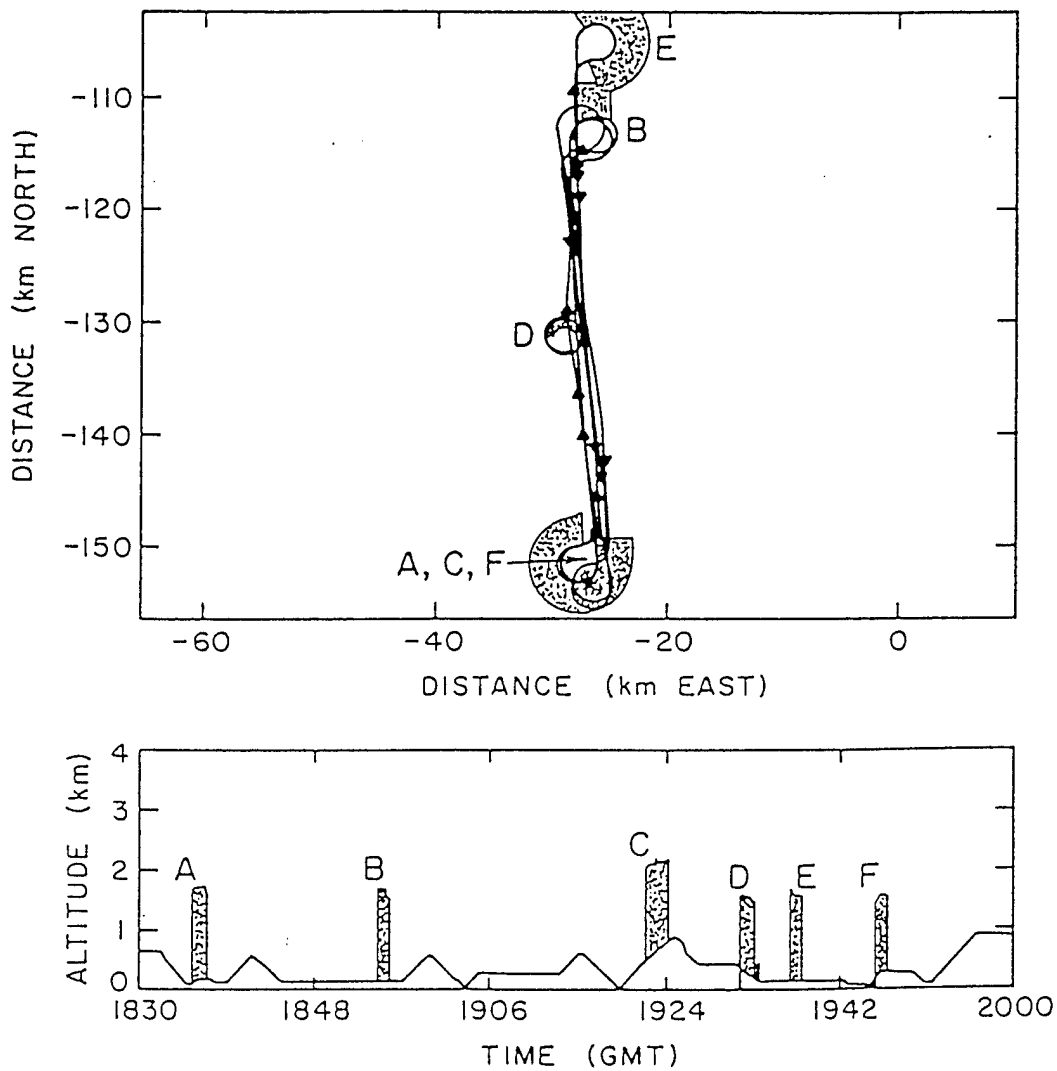the similarly labeled data segments in the previous figure.

Figure 7: a) Map view of flight tracks and areas of coverage for the AVAD analyses. Labels A-F mark the locations of profiles. b) Flight altitudes and times for the data used in the AVAD analyses. Profiles D and E are side-looking, A,B,C, and F are up-looking
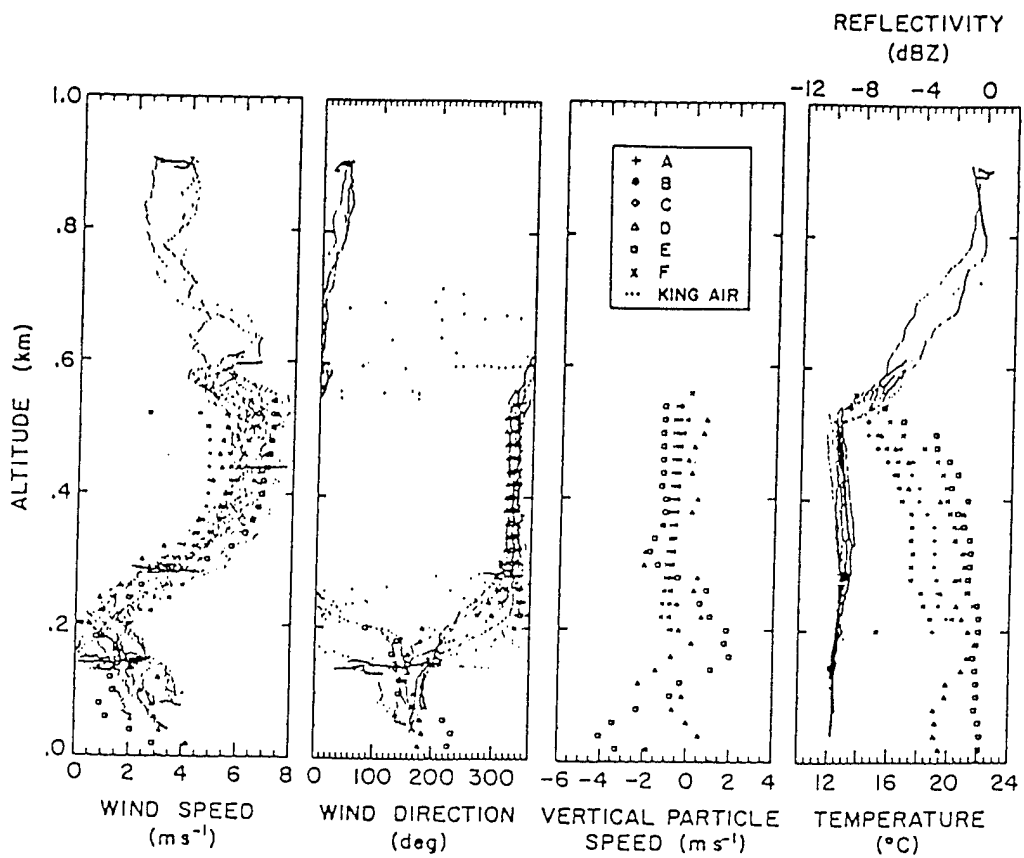
31

Figure 8: Wind profiles Derived from KingAir data (dots) and AVAD analysis. a) Wind Speed. b) Wind Direction. c) Vertical particle speed. d) Temperature and mean reflectivity. Labels A-F on the profiles correspond to the similarly labeled data segments in the previous figure.
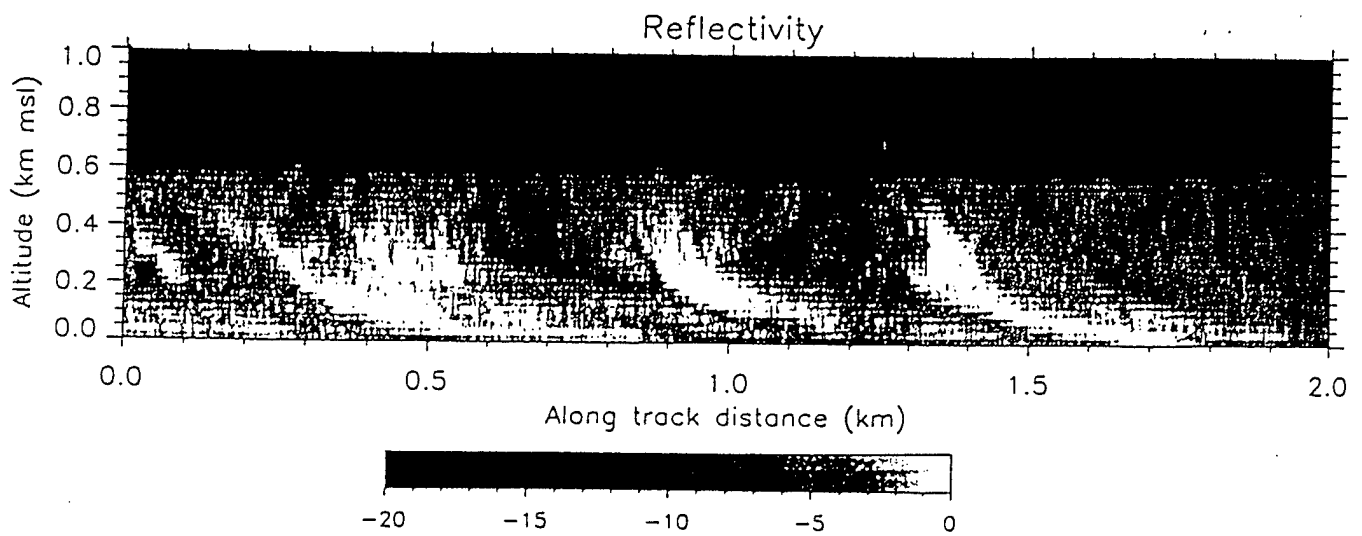
Figure 9: South to North reflectivity cross section. The curvature of the high-reflectivity fallstreaks demonstrates the wind-relative shear present between 200 and 400 m.

/f:angles abelsep14Z

References

[1] Beard, K. V., 1976: Terminal velocity and shape of cloud and precipitation drops aloft. *J. Atmos. Sci.*, 33, 851 – 864.

[2] Bevington, P. R., 1969: *Data Reduction and Error Analysis for the Physical Sciences.*, McGraw-Hill, 336 pp.

[3] Browning, K. A. and R. Wexler, 1968: The determination of kinematic properties of a wind field using Doppler radar. *J. Appl. Meteor.*,7,105–113.

[4] Easterbrook, C. C., 1975: Estimating horizontal wind fields by two dimensional curve fitting of single Doppler radar measurements. Preprints, *16th Radar Met. Conf.*, Houston, Amer. Meteor. Soc., 214–219.

[5] Hildebrand, P. H., W.-C. Lee, C. A. Walther, C. L. Frush, M. Randall, E. Loew, R. Neitzel, R. Parsons, J. Testud., F. Baudin, and A. LeCornec, 1996: The ELDORA/ASTRARIA airborne Doppler weather radar: High-resolution observations from TOGA COARE. *Bull. Amer. Meteor. Soc.*,77,213–232.

[6] Jorgensen,D. P. , T. Matejka, and J. D. DuGranrut. 1996: Multi-beam techniques for deriving wind fields from airborne Doppler radars. *J. meteor. and Atmospheric Physics*, 59, 83–104.

[7] Lee,W.-C., P. Dodge, F. D. Marks, P. H. Hildebrand. 1994: Mapping of airborne Doppler radar data. *J. Atmos. Oceanic Technol.*,11, 572 – 578.

[8] Lenschow, D. H., 1971: The Measurement of air velocity and temperature using the NCAR Buffalo aircraft measuring system. *NCAR Tech Note*, NCAR TN/EDD-74,39 pp.

[9] Lhermitte, R. and D. Atlas, 1961: Precipitation motion by pulse Doppler. Preprints, *Ninth Weather Radar Conf.*, Kansas City, Amer. Met. Soc.,218–223.

[10] Menke, T., 1993: *Geophysical data analysis : discrete inverse theory* . Academic Press, 289 pp.

[11] Mueller, C. K. and P. H. Hildebrand, 1985: Evaluation of meteorological airborne radar. Part II.: Triple Doppler analysis. *J. Atmos. Oceanic Technol.*,2, 381-392.

[12] Probert–Jones, J. R., 1960: Meteorological use of pulsed Doppler radar. *Nature*, 186,271–273.

[13] Srivastava, R. C., T. J. Matejka , and T. J. Lorello, 1986: Doppler radar study of the trailing anvil region associated with a squall line. *J. Atmos. Sci.*,43, 356–377.

[14] Testud, J. , G. Breger, P. Amayenc, M. Chong, B. Nutten, and A. Sauvaget, 1980: A Doppler radar observation of a cold front. Three dimensional air circulation , related precipitation system and associated wave–like motions. *J. Atmos. Sci.*, 37,78–98.